https://ntrs.nasa.gov/search.jsp?R=19710021342 2020-03-11T20:23:05+00:00Z

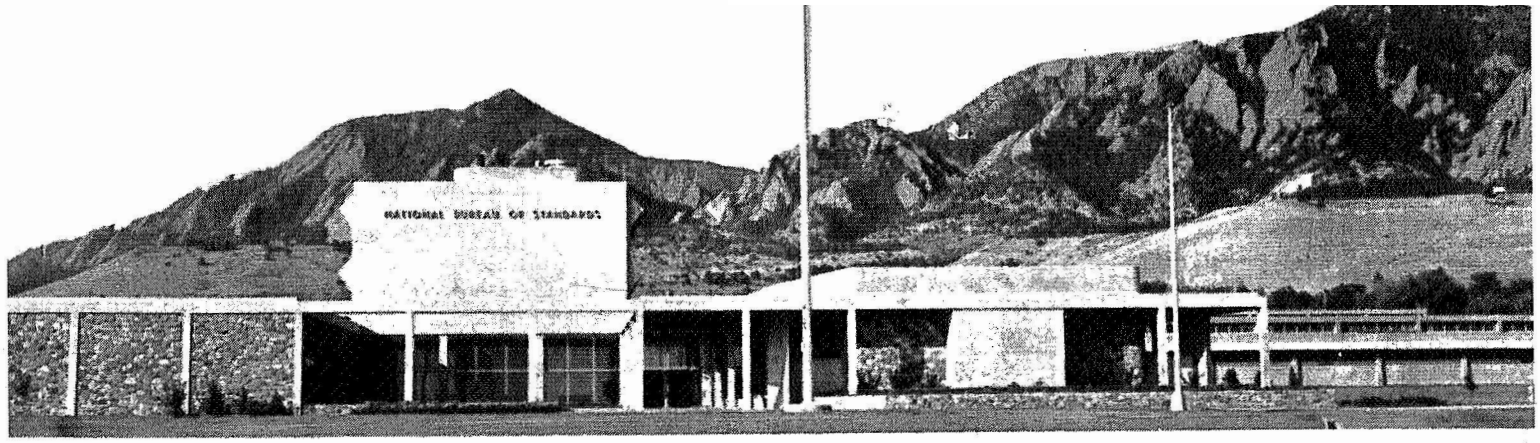

R-06-006-003

N71-30818
CR-119241

NBS REPORT
9793

INSTRUMENTATION FOR HYDROGEN SLUSH STORAGE CONTAINERS

by

D. H. Weitzel, R. S. Collier, D. A. Ellerbruch
J. E. Cruz, and L. T. Lowe

AUG 1971
RECEIVED
NASA STI FACILITY
INPUT BRANCH

CASE FILE
COPY

U. S. DEPARTMENT OF COMMERCE
NATIONAL BUREAU OF STANDARDS
Institute for Basic Standards
Boulder, Colorado 80302

NATIONAL BUREAU OF STANDARDS

The National Bureau of Standards[1] was established by an act of Congress March 3, 1901. The Bureau's overall goal is to strengthen and advance the Nation's science and technology and facilitate their effective application for public benefit. To this end, the Bureau conducts research and provides: (1) a basis for the Nation's physical measurement system, (2) scientific and technological services for industry and government, (3) a technical basis for equity in trade, and (4) technical services to promote public safety. The Bureau consists of the Institute for Basic Standards, the Institute for Materials Research, the Institute for Applied Technology, the Center for Computer Sciences and Technology, and the Office for Information Programs.

THE INSTITUTE FOR BASIC STANDARDS provides the central basis within the United States of a complete and consistent system of physical measurement; coordinates that system with measurement systems of other nations; and furnishes essential services leading to accurate and uniform physical measurements throughout the Nation's scientific community, industry, and commerce. The Institute consists of a Center for Radiation Research, an Office of Measurement Services and the following divisions:

Applied Mathematics—Electricity—Heat—Mechanics—Optical Physics—Linac Radiation[2]—Nuclear Radiation[2]—Applied Radiation[2]—Quantum Electronics[3]—Electromagnetics[3]—Time and Frequency[3]—Laboratory Astrophysics[3]—Cryogenics[3].

THE INSTITUTE FOR MATERIALS RESEARCH conducts materials research leading to improved methods of measurement, standards, and data on the properties of well-characterized materials needed by industry, commerce, educational institutions, and Government; provides advisory and research services to other Government agencies; and develops, produces, and distributes standard reference materials. The Institute consists of the Office of Standard Reference Materials and the following divisions:

Analytical Chemistry—Polymers—Metallurgy—Inorganic Materials—Reactor Radiation—Physical Chemistry.

THE INSTITUTE FOR APPLIED TECHNOLOGY provides technical services to promote the use of available technology and to facilitate technological innovation in industry and Government; cooperates with public and private organizations leading to the development of technological standards (including mandatory safety standards), codes and methods of test; and provides technical advice and services to Government agencies upon request. The Institute also monitors NBS engineering standards activities and provides liaison between NBS and national and international engineering standards bodies. The Institute consists of the following technical divisions and offices:

Engineering Standards Services—Weights and Measures—Flammable Fabrics—Invention and Innovation—Vehicle Systems Research—Product Evaluation Technology—Building Research—Electronic Technology—Technical Analysis—Measurement Engineering.

THE CENTER FOR COMPUTER SCIENCES AND TECHNOLOGY conducts research and provides technical services designed to aid Government agencies in improving cost effectiveness in the conduct of their programs through the selection, acquisition, and effective utilization of automatic data processing equipment; and serves as the principal focus within the executive branch for the development of Federal standards for automatic data processing equipment, techniques, and computer languages. The Center consists of the following offices and divisions:

Information Processing Standards—Computer Information—Computer Services—Systems Development—Information Processing Technology.

THE OFFICE FOR INFORMATION PROGRAMS promotes optimum dissemination and accessibility of scientific information generated within NBS and other agencies of the Federal Government; promotes the development of the National Standard Reference Data System and a system of information analysis centers dealing with the broader aspects of the National Measurement System; provides appropriate services to ensure that the NBS staff has optimum accessibility to the scientific information of the world, and directs the public information activities of the Bureau. The Office consists of the following organizational units:

Office of Standard Reference Data—Office of Technical Information and Publications—Library—Office of Public Information—Office of International Relations.

---

[1] Headquarters and Laboratories at Gaithersburg, Maryland, unless otherwise noted; mailing address Washington, D.C. 20234.
[2] Part of the Center for Radiation Research.
[3] Located at Boulder, Colorado 80302.

NATIONAL BUREAU OF STANDARDS REPORT

NBS PROJECT
27506-2750460
27506-2750464

June 1, 1971

NBS REPORT
9793

INSTRUMENTATION FOR HYDROGEN SLUSH STORAGE CONTAINERS

by

D. H. Weitzel, R. S. Collier, D. A. Ellerbruch,
J. E. Cruz, and L. T. Lowe

Cryogenics Division
Institute for Basic Standards
National Bureau of Standards
Boulder, Colorado 80302

IMPORTANT NOTICE

NATIONAL BUREAU OF STANDARDS REPORTS are usually preliminary or progress accounting documents intended for use within the Government. Before material in the reports is formally published it is subjected to additional evaluation and review. For this reason, the publication, reprinting, reproduction, or open-literature listing of this Report, either in whole or in part, is not authorized unless permission is obtained in writing from the Office of the Director, National Bureau of Standards, Washington, D.C. 20234. Such permission is not needed, however, by the Government agency for which the Report has been specifically prepared if that agency wishes to reproduce additional copies for its own use.

U.S. DEPARTMENT OF COMMERCE
NATIONAL BUREAU OF STANDARDS

TABLE OF CONTENTS

	Page
LIST OF FIGURES	iv
ABSTRACT	vi
1. Introduction	1
2. Experimental Program	3
3. Interface Location Methods	6
3. 1 Time Domain Reflectometry	6
3. 1. 1 Brief History.	6
3. 1. 2 TDR Experiments.	8
3. 2 Frequency Domain Reflectometry	14
3. 2. 1 Theory of the FDR Method.	14
3. 2. 2 FDR Experiments.	17
3. 3 Carbon Film Sensors.	22
4. Total Mass Gauging	24
4. 1 Resonant Cavity Experiments.	27
4. 2 Resonant Cavity Analysis.	33
4. 2. 1 Conclusions	37
4. 3 Capacitance Methods.	39
4. 3. 1 Mass Gauging by Capacitance Measurement	39
4. 3. 1. 1 Dewar Gauging Experiment	40
4. 3. 1. 2 Geometrical Effects	40
4. 3. 2 Capacitors in Cubic Meter Test Dewar	50
4. 4 Microwave Method for Dielectric Measurement.	54
4. 4. 1 System Theory	54
4. 4. 2 Experimental Results	58
5. Summary	60
5. 1 Settled Slush Level Detection	60

TABLE OF CONTENTS (Continued) Page

5.2 Total Mass Gauging 61

5.3 Technology Transfer 61

Appendix A. Total Mass Gauging in a Spherical Resonant Cavity. 63

Appendix B. Upper and Lower Bounds for Capacitance. . . 84

Appendix C. Total Mass Gauging in a Cylindrical Tank by Capacitance Methods. 88

LIST OF FIGURES

Figure 1. Aging of Settled Slush Hydrogen. . . . 2

Figure 2. Capacitance and Time Domain Reflectometry Gauging Methods in Cubic Meter Vessel. . . 4

Figure 3. Microwave Systems and Carbon Film Sensors in Cubic Meter Vessel. 5

Figure 4. Time Domain Reflectometry Measurement System. 7

Figure 5. Parallel Plane Transmission Line. 10

Figure 6. Time Domain Reflection Coefficients in Hydrogen. . 12

Figure 7. Hydrogen Liquid Level Measurement with Time Domain Reflectometry (5-13-71, Run 3). . . . 15

Figure 8. Frequency Domain Reflectometry Method for Liquid and Slush Level Detection. 16

Figure 9. FDR Results in Cubic Meter Vessel. 18

Figure 10. Spectrum Analysis of Frequency Domain Reflections. . 19

Figure 11. Spectrum Analysis of Frequency Domain Reflections. . 20

Figure 12. Carbon Film Sensor Response in Liquid and Slush Hydrogen. 23

LIST OF FIGURES (Continued) Page

Figure 13. Carbon Film Thermometry Results in Liquid Hydrogen. 25

Figure 14. Carbon Film Thermometry Results in Liquid Hydrogen. 26

Figure 15. Resonant Cavity Method. 28

Figure 16. Resonant Cavity Results, Cylindrical Dewar. . . . 29

Figure 17. Resonant Cavity Experiment, Spherical Dewar. . . 31

Figure 18. Resonant Cavity Results, 48 cm Diameter Sphere.. 32

Figure 19. Resonant Cavity Results in One Cubic Meter Vessel with Interfering Obstructions. 34

Figure 20. Mass Gauging with Capacitor Electrodes Fastened to Inner Walls of Dewar. 41

Figure 21. Upper and Lower Bounds for Parallel Plate Capacitors. 45

Figure 22. Behavior of Concentric Sphere Capacitor. . . . 48

Figure 23. Data from Capacitors in One Cubic Meter Hydrogen Slush Vessel. 52

Figure 24. Microwave System Used to Measure Density in Terms of Transmission Time. 55

Figure 25. Settled Slush Density Data Obtained by Microwave Method. 59

Figure A1. Resonant Frequency vs. Mass, TM_{m11} Mode. . . 79

Figure A2. Resonant Frequency vs. Mass, TM_{m21} Mode. . . 80

Figure A3. Resonant Frequency vs. Mass, TM_{m31} Mode. . . 81

Figure A4. Resonant Frequency vs. Mass, TM_{m41} Mode. . . 82

Figure A5. Mass Gauging in Spherical Vessel (TM_{021} Mode, Liquid Nitrogen). 83

ABSTRACT

An experimental and analytical study of hydrogen liquid and slush tank gauging methods is described. The objective was continuous inventory of hydrogen slush during ground storage. Two approaches were taken, the first based on vapor-liquid and liquid-slush interface location, the second based on direct total mass sensing. Three interface location methods and three total mass methods were tried. Carbon film point sensors, previously used for vapor-liquid discrimination, were also successful for discrimination between triple-point liquid and settled slush. Time domain reflectometry was very successful for liquid level location and can probably be developed for settled slush level detection. Resonant cavity and capacitance methods were developed and demonstrated for accurate determination of total mass of liquid or slush without reference to liquid or settled slush levels.

Key Words: Hydrogen Liquid; Hydrogen Slush; Instrumentation; Liquid Level Sensing; Mass Gauging; Slush Level Sensing; Storage.

INSTRUMENTATION FOR HYDROGEN SLUSH STORAGE CONTAINERS*

D. H. Weitzel, R. S. Collier, D. A. Ellerbruch
J. E. Cruz, and L. T. Lowe

1. Introduction

An investigation of methods and instrumentation for continuous inventory of hydrogen slush during ground storage has been completed. This work was performed during 1970 under NASA/SNPO-C sponsorship at the Cryogenics Division of the National Bureau of Standards. The vessel used for most of the experimental work was a vacuum-insulated cylindrical steel dewar 76 cm in diameter by 243 cm deep. Actual volume was 1.102 m^3; maximum working volume was about 0.75 m^3.

When such a vessel contains slush hydrogen, the solids will normally settle to the bottom as soon as the fluid is quiescent. Freshly prepared slush has a settled solid fraction of 0.35 to 0.45. The solid fraction in the settled portion increases as the slush ages. Figure 1 shows change in solid mass fraction and density for settled slush in a vessel with heat leak on the order of 6.7×10^{-8} W cm^{-3}. This is a very low heat influx, resulting in a solids loss of only 0.3 percent per day.

If there is more heat flow to the slush, and consequently more melting of the solids, the density of the remaining solid fraction increases at a faster rate than shown in figure 1. Thus, the slush in a vessel having approximately 20 times as much heat influx as the above example reached a solid fraction of 0.6 in 17 hours, instead of in 50 hours. For the 1 m^3 vacuum-insulated steel dewar used in most of the present work, a settled solid fraction of 0.6 was reached in about 8 hours[1].

* This work was carried out at the National Bureau of Standards under NASA (SNPO-C) Contract R-45 and NASA-MSFC Contract H-2159A.

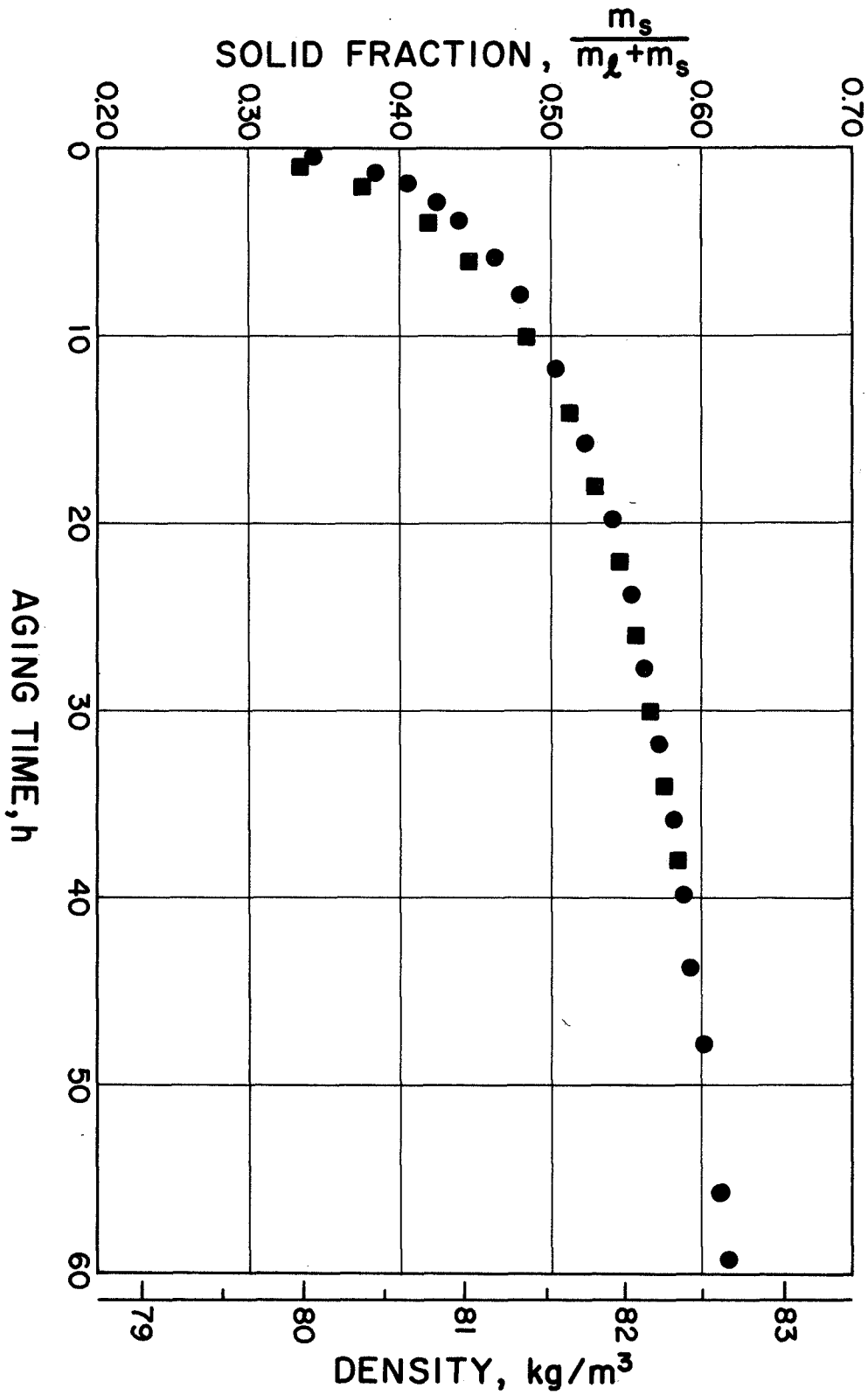

Figure 1. Aging of Settled Slush Hydrogen.

The settled solids in a slush storage tank will form an interface which represents a sharp density discontinuity similar to the vapor-liquid interface, although of much smaller magnitude. Effective slush tank gauging will result from accurate location of both the vapor-liquid and the liquid-slush interfaces, along with knowledge of tank geometry and density gradients in both the liquid and the settled slush portions. Alternately, gauging methods which respond to total mass without reference to density may be used. Both approaches were included in the present investigation, with the total mass methods proving more reliable than methods depending on interface location.

2. Experimental Program

The various forms of tank gauging instrumentation which were studied are schematically represented in figures 2 and 3. The transducers are shown in their approximately true positions in the hydrogen slush storage and upgrading vessel. In figure 2 are shown two capacitors of different geometry and a time domain reflectometry transmission line. The capacitors are total mass sensors, as will be shown, and the TDR transmission line is designed to detect and locate a dielectric discontinuity such as occurs at a vapor-liquid or liquid-slush interface.

In figure 3 are shown four more transducer systems, making a total of seven for which data were obtained. Represented at the left are a pair of microwave horns with faces 90 cm apart which give average density of the fluid between them by means of a time-delay-induced frequency difference. Another pair of microwave horns located just below the top plate of the dewar are for location of interfaces by means of a microwave reflection method. A third microwave system uses a pair of loop antennae in the ullage space near the top of the dewar and measures total mass by means of a resonant cavity technique. Finally on the right side of the diagram are shown six carbon film sensors which give temperature (and hence density) distribution and also can discriminate between triple-point liquid and settled slush.

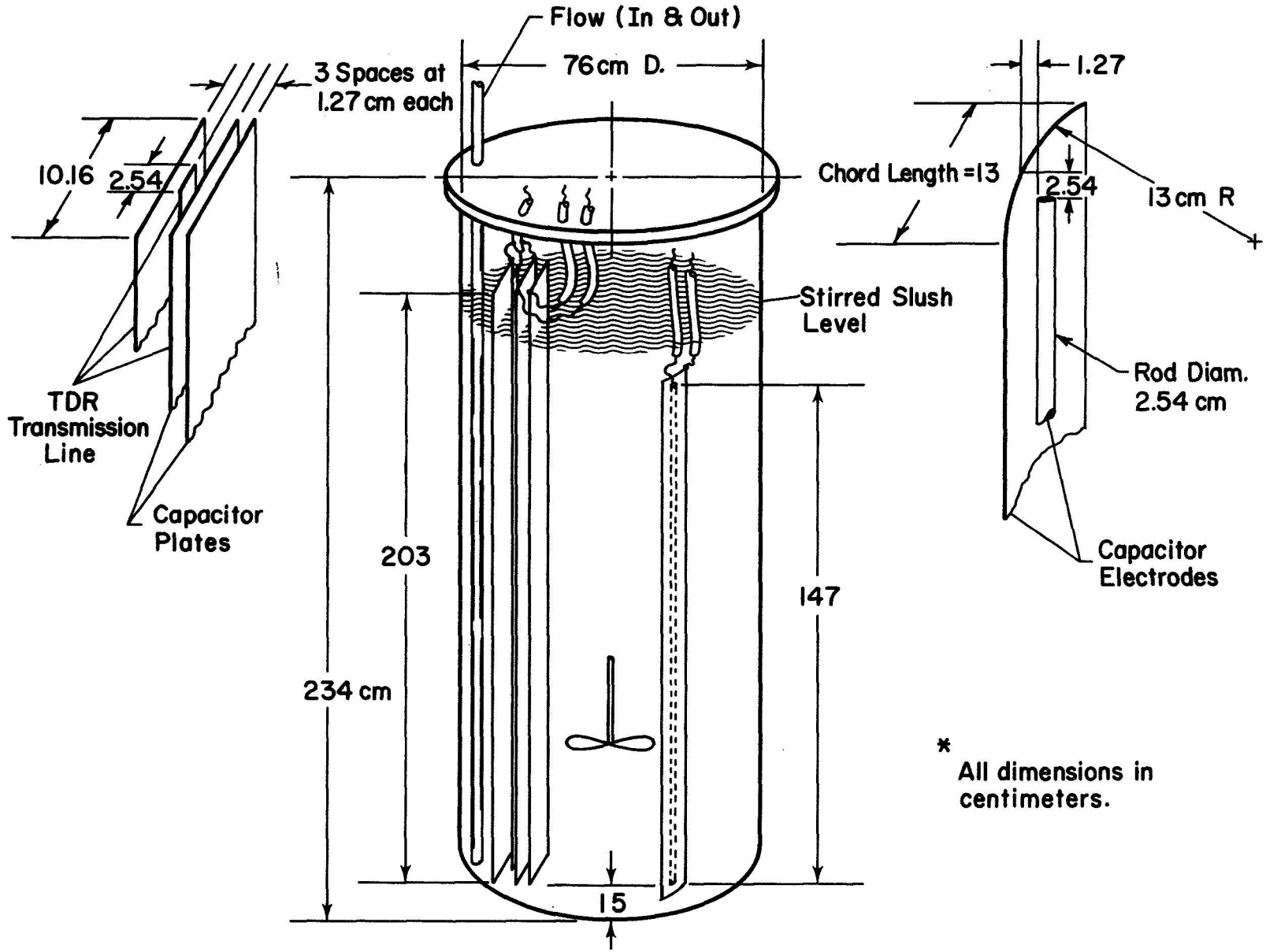

Figure 2. Capacitance and Time Domain Reflectometry Gauging Methods in Cubic Meter Vessel.

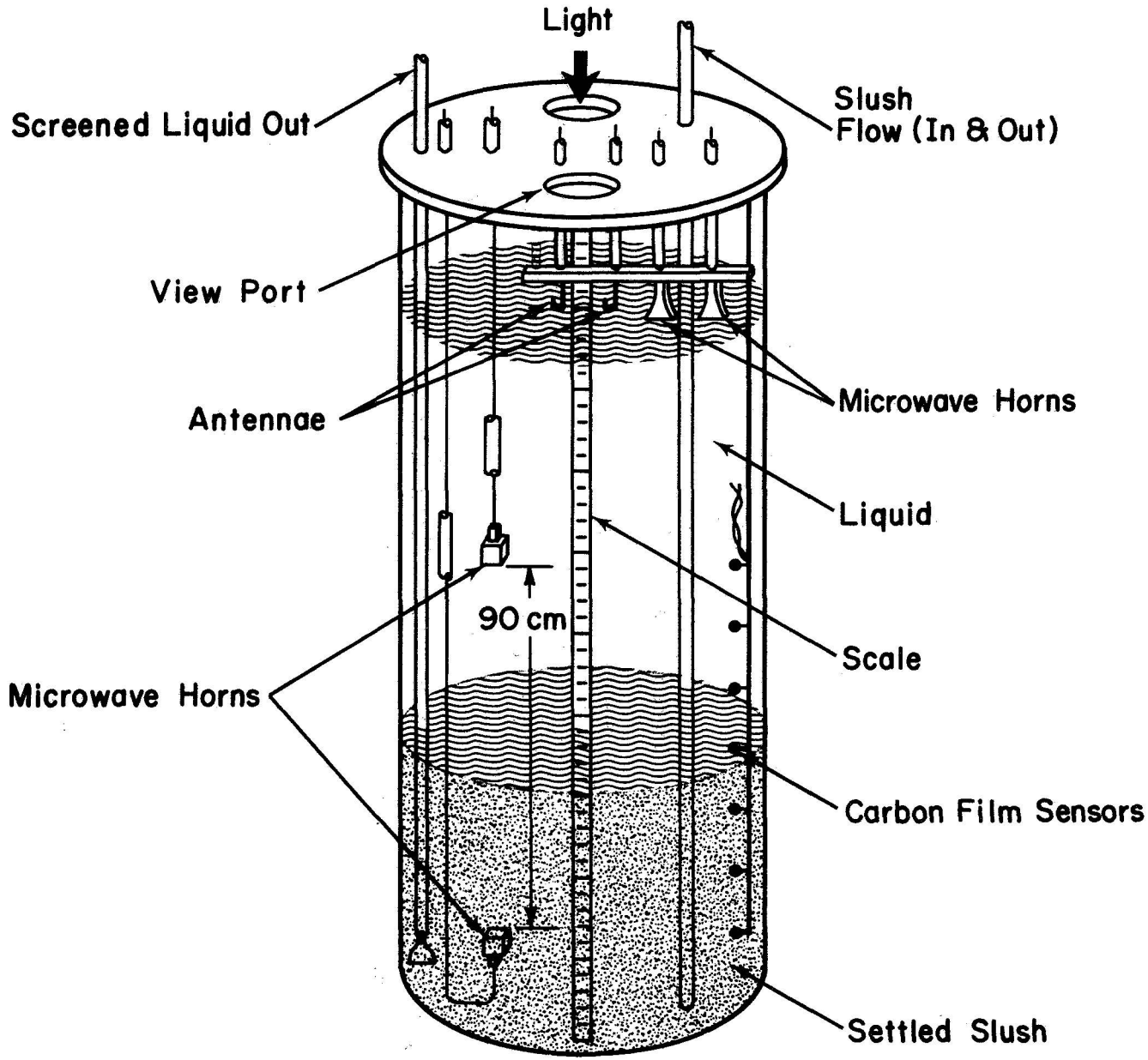

Figure 3. Microwave Systems and Carbon Film Sensors in Cubic

Each of the seven instrumentation systems will be discussed in some detail, and experimental results will be given. In a final section we will compare the various methods and evaluate their potential.

3. Interface Location Methods

The methods best suited for vapor-liquid and/or liquid-slush interface location are time domain reflectometry, microwave frequency domain reflectometry, and carbon film sensors. These three will be covered in the present section.

3.1 Time Domain Reflectometry

3.1.1 Brief History

Time Domain Reflectometry (TDR) techniques for measuring transmission line discontinuities separated by one inch or less have been developed[2-7] in the last eight years. The pulse-echo method has been used for many years for location of faults in wide band transmission systems such as coaxial cables. The pulse-echo reflectometry as a laboratory tool has had to await the development of fast rise time pulse generators and sampling oscilloscopes.

In TDR systems a fast rise time (<120 picoseconds) step generator launches a voltage step down the transmission line under investigation. The incident and reflected waves at some particular point on the transmission line are monitored with a sampling oscilloscope as shown in figure 4.

The system immediately displays the characteristic impedance of the line under test. Analysis of the display shows the nature of each discontinuity, which can be resistive, capacitive, or inductive.

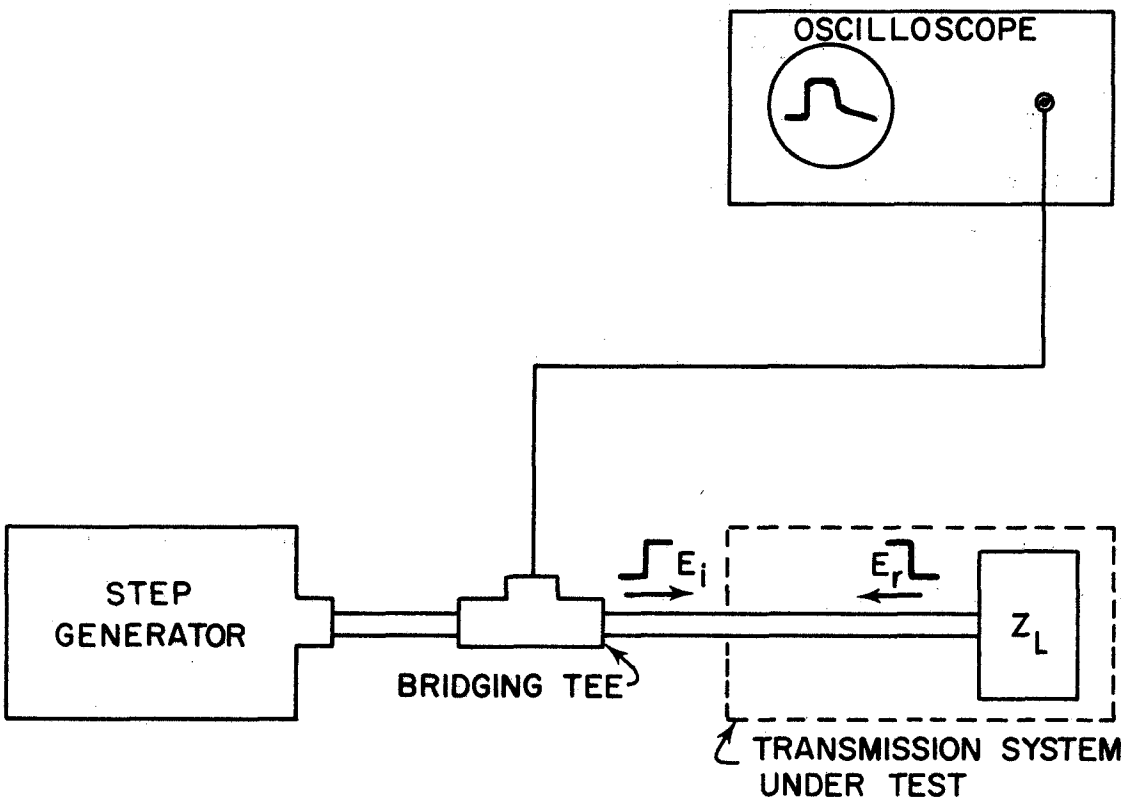

Figure 4. Time Domain Reflectometry Measurement System.

If the losses of the transmission line are negligible, the characteristic impedance of the line is

$$Z = \frac{1}{\sqrt{\epsilon}} f \text{ (cross-sectional dimensions)} \tag{3-1}$$

where

ϵ = dielectric constant of the medium between the conductors.

Equation (3-1) shows that the characteristic impedance of the transmission line will change with either dielectric constant or cross-sectional dimension. It is the change in impedance as a function of dielectric constant that was used in the work to be described below.

3.1.2 TDR Experiments

Detection of the liquid-vapor interface of cryogenic liquids was readily demonstrated. The change in dielectric constant of equation (3-1) gives a change in characteristic impedance of the transmission line such that

$$Z_L = \frac{1}{\sqrt{\epsilon_L}} f \text{ (cross-sectional dimensions)} \tag{3-2}$$

$$Z_V = \frac{1}{\sqrt{\epsilon_V}} f \text{ (cross-sectional dimensions)} \tag{3-3}$$

and

$$\frac{Z_V}{Z_L} = \sqrt{\frac{\epsilon_L}{\epsilon_V}} . \tag{3-4}$$

Equation (3-4) is defined as the voltage standing wave ratio (VSWR) of the two characteristic impedances of the liquid and gas as a function of the dielectric constant. A similar impedance ratio

$$\frac{Z_L}{Z_S} = \sqrt{\frac{\epsilon_S}{\epsilon_L}} \tag{3-5}$$

exists at the liquid-slush interface.

If ϵ_L (H_2 triple-point liquid) is 1.252 and ϵ_S (0.5 solid fraction slush) is 1.268, then a numerical calculation of VSWR shows that

$$\frac{Z_L}{Z_S} = \sqrt{\frac{1.268}{1.252}} = 1.006 . \tag{3-6}$$

This impedance ratio is well within the sensitivity of the TDR system and should be readily detectable. For the liquid-vapor interface the VSWR is

$$\frac{Z_V}{Z_L} = \sqrt{\frac{1.252}{1.000}} = 1.119 . \tag{3-7}$$

This larger ratio has been used for liquid level sensing.

A rectangular cross-section parallel-plane transmission line, as represented in figure 5, was constructed. The dimension were

$$D = 10.16 \text{ cm}$$
$$b = 2.54 \text{ cm}$$
$$w = 2.54 \text{ cm}$$
$$t = 0.152 \text{ cm} .$$

These dimensions[8] give a characteristic impedance of approximately 61 ohms with gas dielectric between the transmission line conductors. The length of the line was 203 cm. This line was installed in the one-m^3 vessel as shown in figure 2.

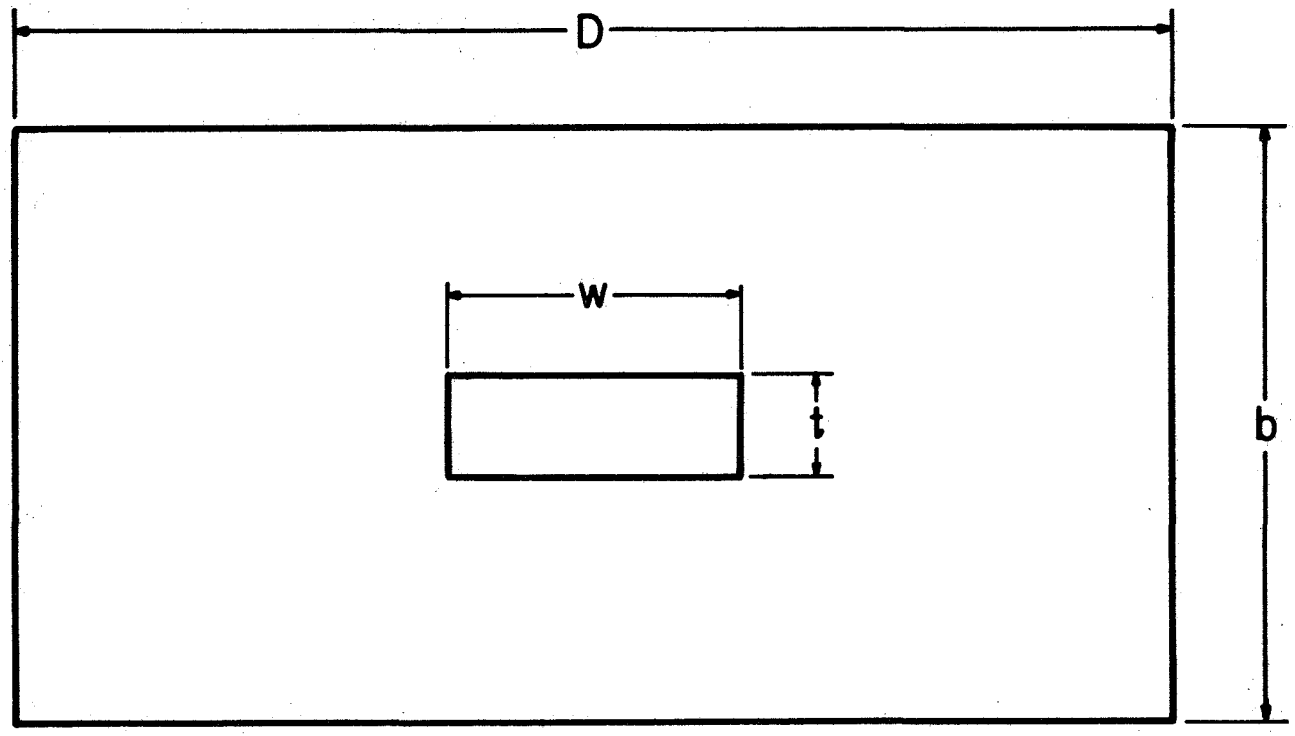

Figure 5. Parallel Plane Transmission Line.

Figure 6 shows three readily detectable levels of characteristic impedance. These levels are calibrated in reflection coefficient units. Zero reflection coefficient is the reference level of 52 ohms in the transmission line.

Reflection coefficient is related to the characteristic impedance by the equation

$$Z_M = \frac{1 + \Gamma_M}{1 - \Gamma_M} Z_R \tag{3-8}$$

where

Z_M = measured characteristic impedance
Γ_M = measured reflection coefficient
Z_R = reference impedance of 52 ohms.

Using equation (3-8), the impedance level of the vapor dielectric (Z_V), normal boiling point dielectric (Z_{NBP}), and triple point dielectric (Z_{TP}) were found to be

$$Z_V = \frac{1 + \Gamma_V}{1 - \Gamma_V} Z_R = \frac{1 + 0.08}{1 - 0.08} (52) = 61 \text{ ohms},$$

$$Z_{NBP} = \frac{1 + \Gamma_{NBP}}{1 - \Gamma_{NBP}} Z_R = \frac{1 + 0.022}{1 - 0.022} (52) = 54.3 \text{ ohms},$$

$$Z_{TP} = \frac{1 + \Gamma_{TP}}{1 - \Gamma_{TP}} Z_R = \frac{1 + 0.017}{1 - 0.017} (52) = 53.7 \text{ ohms}.$$

Using the relationship

$$\frac{Z_{NBP}}{Z_{TP}} = \sqrt{\frac{\epsilon_{TP}}{\epsilon_{NBP}}}$$

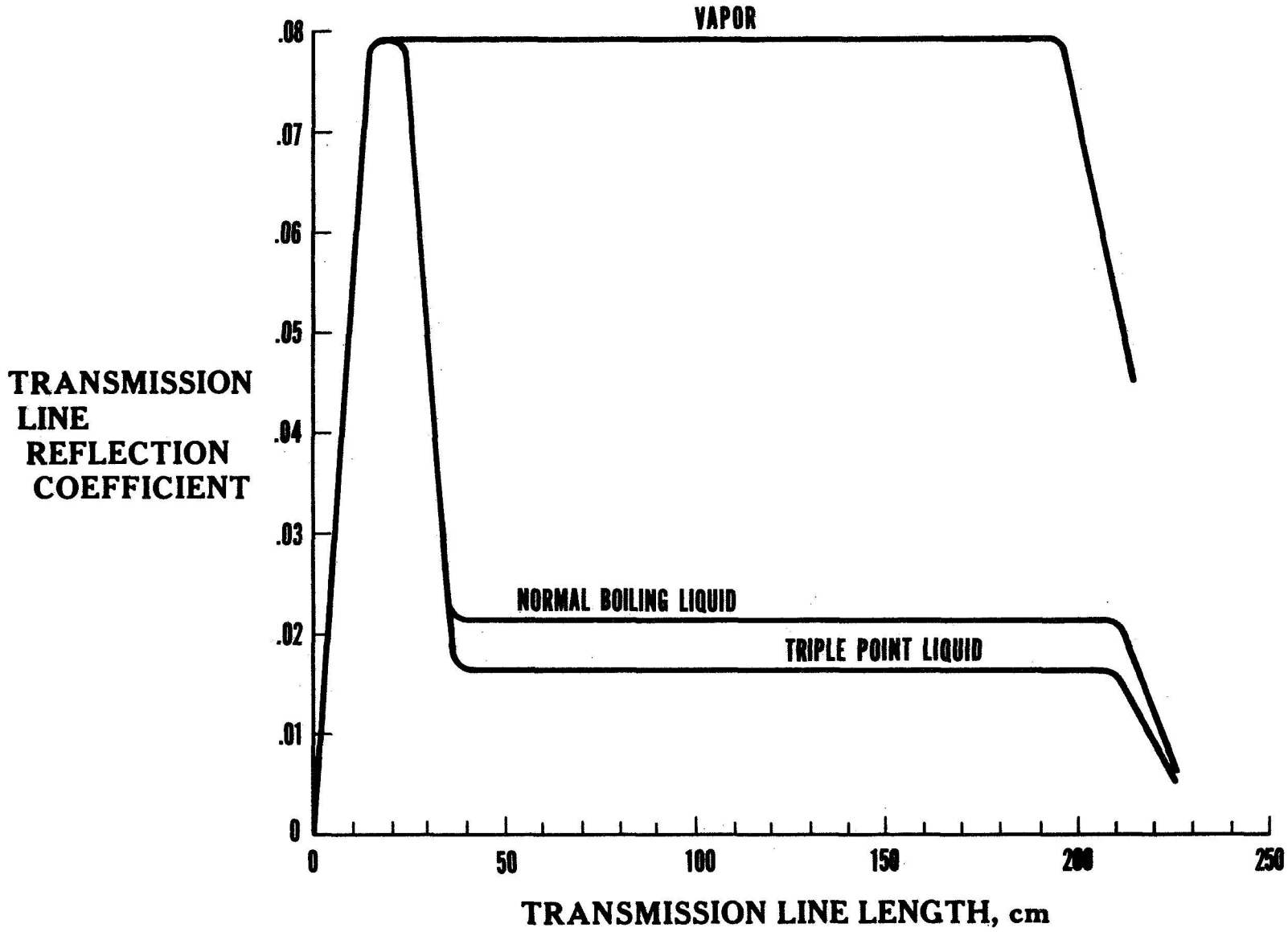

Figure 6. Time Domain Reflection Coefficients in Hydrogen.

and substituting the values of Z_{NBP} and Z_{TP}, it is found that

$$\frac{\epsilon_{TP}}{\epsilon_{NBP}} = \left(\frac{Z_{NBP}}{Z_{TP}}\right)^2 = \left(\frac{54.3}{53.7}\right)^2 = 1.02 .$$

This ratio is correct for the dielectric constants of normal-boiling-point and triple-point hydrogen. The experiment shows that $LH_{2(TP)}$ is readily discernible from $LH_{2(NBP)}$ with the TDR system.

Triple-point LH_2 and 0.5 solid fraction slush hydrogen have a dielectric constant ratio of about 1.01. The TDR was consequently tried for possible detection of the liquid-slush hydrogen interface. However, a liquid-slush interface was not readily detected. Reasons for not detecting the liquid-slush interface could be that the slush melted between the transmission line conductors, or the slush did not readily pack between the inner and outer conductors.

Another transmission line is now being constructed. This line will be made of stainless steel and will have different cross-section configuration. Another attempt to detect the liquid-slush interface with this new TDR line will be made. In the meantime we are using a perforated coaxial stainless steel TDR line to obtain reference flow rates from the one-m^3 test vessel.

The standing wave voltage can be displayed as the vertical part of an oscilloscope trace, where the voltage is proportional to the characteristic impedance defined by equation (3-1). The horizontal displacement of the oscilloscope trace will be proportional to the signal transmission time, which in turn will be proportional to the effective length of the transmisstion line. The vertical output can be used to start and stop a counter in the period mode. In particular, the counter can be triggered

by the vertical voltage step which is reflected from the vapor-liquid interface. The counter will then measure the period of signal transmission through the vapor-filled part of the TDR line. As the liquid level goes down, this period increases.

Figure 7 shows a typical liquid level vs. time plot which was obtained during outflow from the one-m^3 test vessel. These curves are generated by computer direct from data recorded on magnetic tape during flow tests. The TDR technique is proving to be a very useful tool in this work.

3.2 Frequency Domain Reflectometry

A second signal reflection method which can be used for interface location is illustrated in figure 8. This method uses microwave signals and does not require a transmission line. It therefore has the advantage of simpler installation and better sampling of the total dewar contents, but the possible disadvantage of spurious reflections or distortions from surfaces or objects inside the dewar.

3.2.1 Theory of the FDR Method

With reference to figure 8, the microwave signal generator is swept in frequency over its spectrum. The sweep generator output has a sawtooth or ramp waveform so that a linear frequency versus time output is produced by the microwave signal generator.

The microwave signal travels from the generator to the mixer by two paths. If the electrical lengths of the two paths were identical, the reference and test signals going into the mixer would arrive at the same time, t_1, and their instantaneous frequencies would coincide at all times. But the test signal will arrive at a later time because this signal goes into the cryostat and a portion is reflected from the vapor-liquid interface,

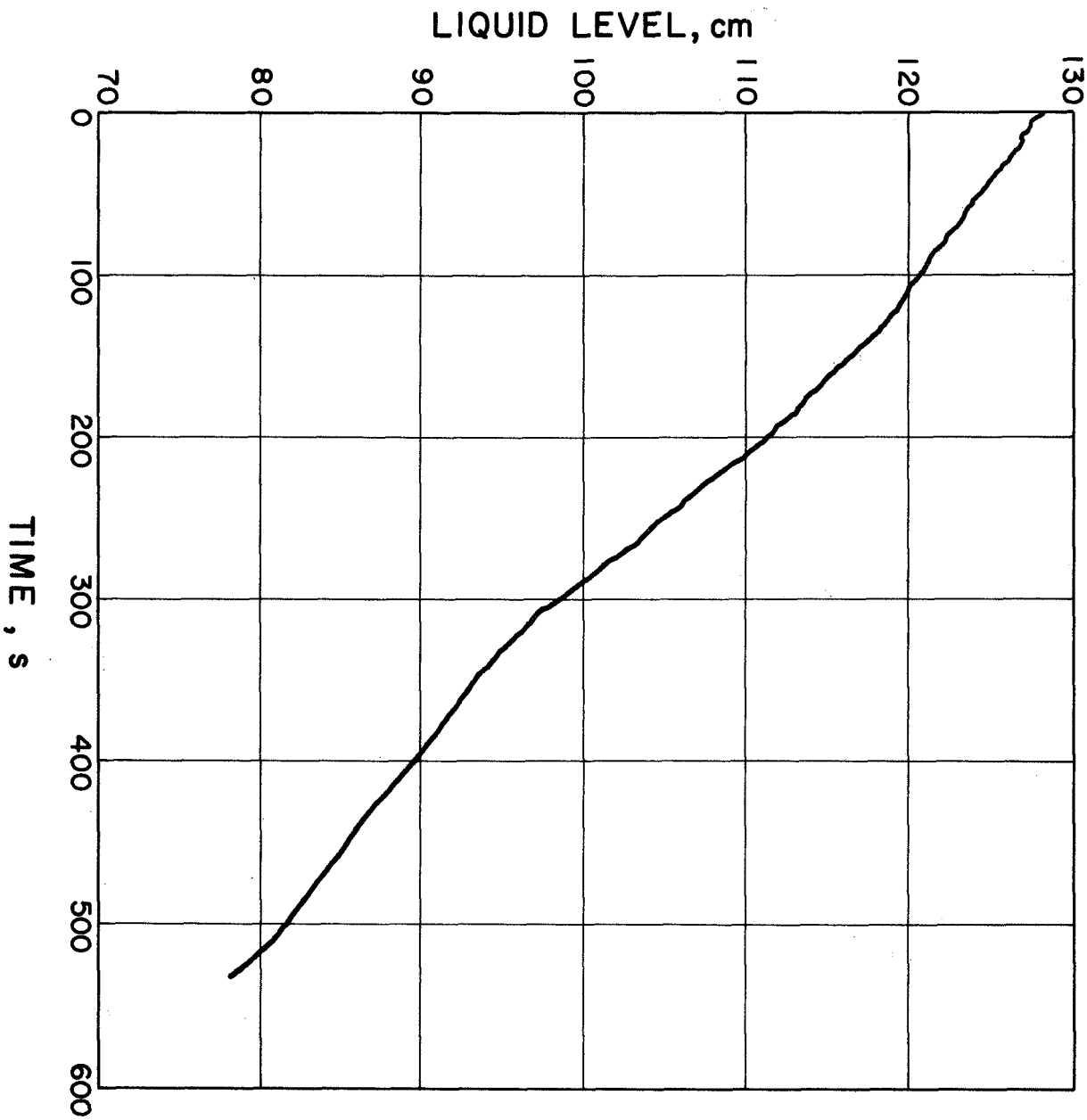

Figure 7. Hydrogen Liquid Level Measurement with Time Domain Reflectometry (5-13-71, Run 3).

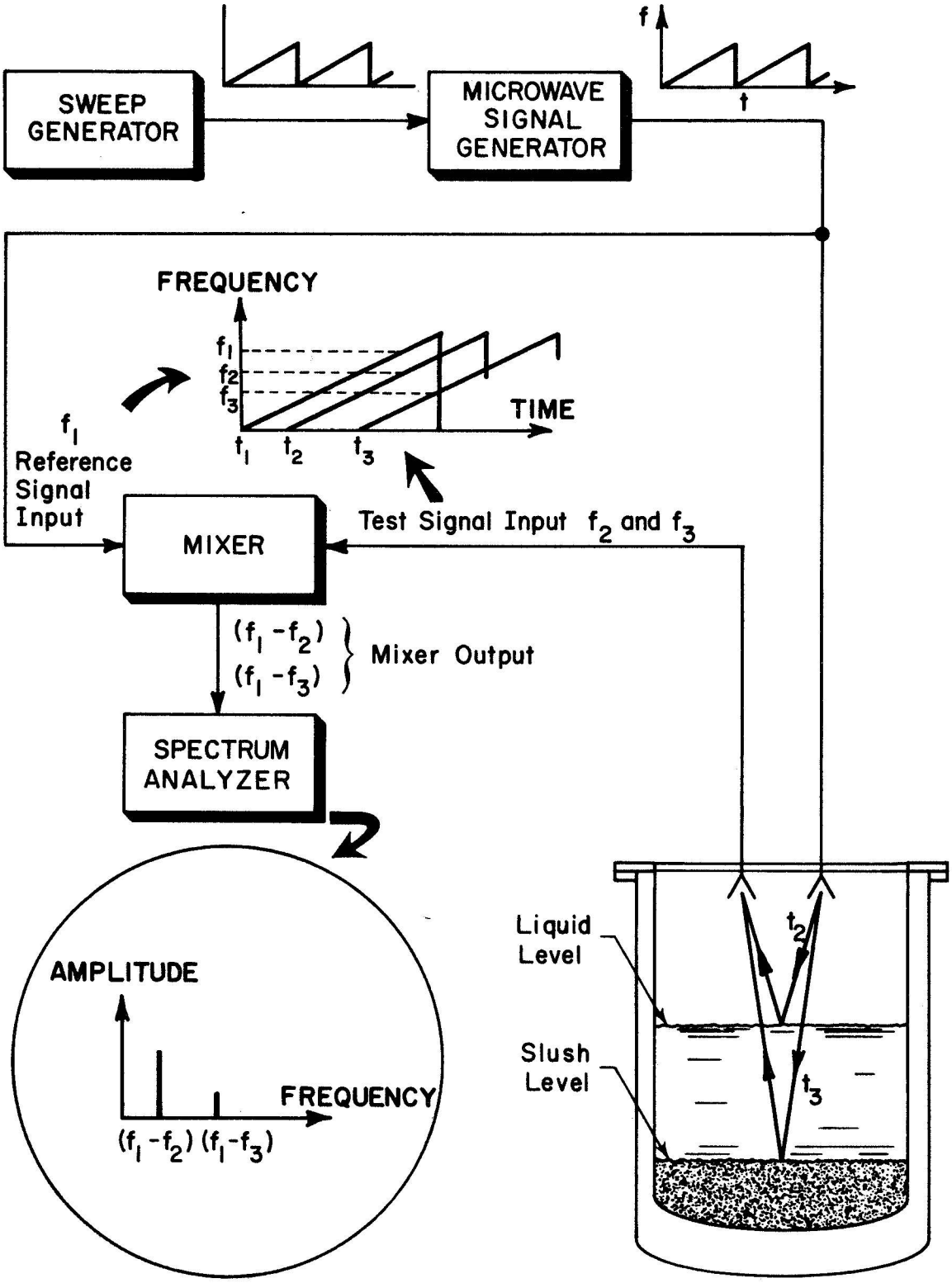

Figure 8. Frequency Domain Reflectometry Method for Liquid and Slush Level Detection.

while another portion is reflected from the liquid-slush interface. Thus, the signal reflected from the vapor-liquid interface will arrive at the mixer at time t_2. The signal reflected from the liquid-slush interface will arrive even later, at time t_3.

Because all inputs to the mixer arrive at different times, the instantaneous frequencies differ, as shown by the frequency vs. time relationship on the figure. The mixer is essentially a product demodulator, i. e., a device having an output signal which is the product of sums and differences, but all except the differences $(f_1 - f_2)$ and $(f_1 - f_3)$ are filtered out. These are displayed on a spectrum analyzer and are functions of the distances from the plane of the horns to the liquid and slush planes. The relationship between distances and frequency is

$$\ell_i = C \frac{\Delta f_i}{\sqrt{\epsilon}}$$

where ϵ is the average dielectric constant of the medium between the horns and the interfaces, Δf_i is the measured frequency difference, C is a constant, and ℓ_i is the distance from the horns to the ith interface.

3. 2. 2 FDR Experiments

A pair of microwave horns were located above the liquid near the top of the one-m^3 test dewar as shown in figure 3. Figure 9 shows the relation obtained between frequency shift and liquid level for both nitrogen and hydrogen. The uncertainty in visual liquid level (abscissa) is one or two cm, which contributes significantly to the scatter of the data.

Slush level data are shown in figures 10 and 11, which are oscilloscope pictures of the spectrum analyzer trace. The horizontal scale is actually frequency, but the corresponding fluid depth scale is shown,

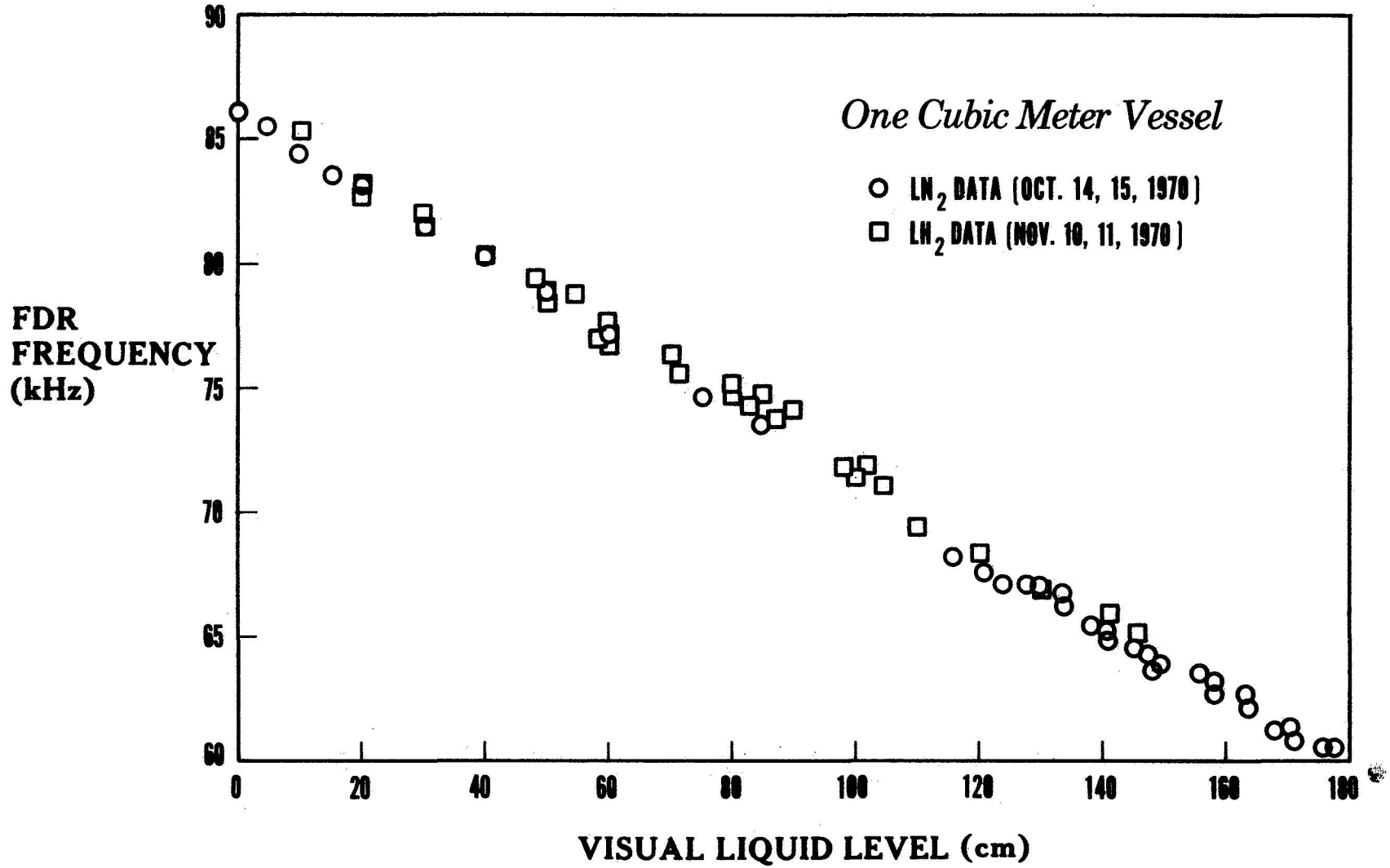

Figure 9. FDR Results in Cubic Meter Vessel.

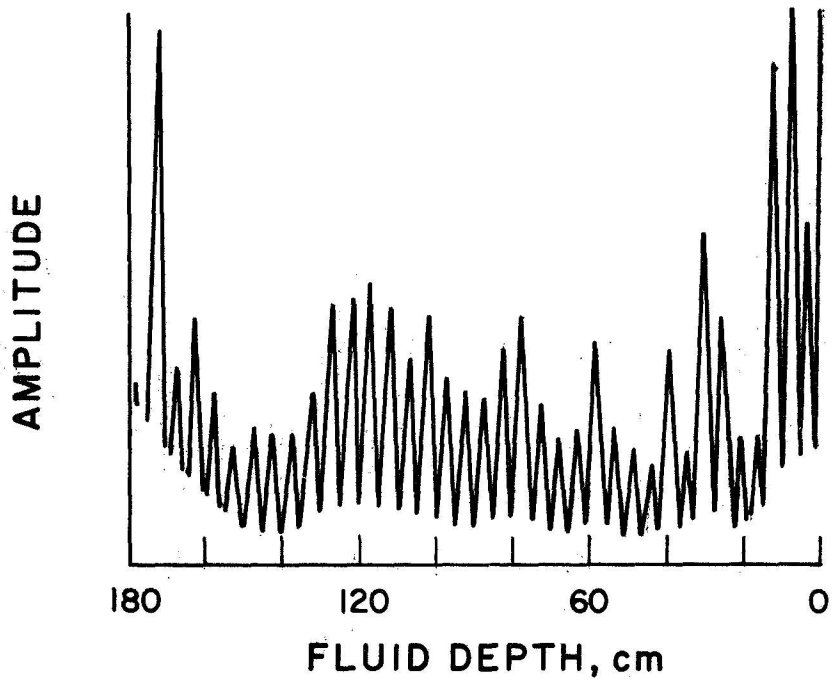

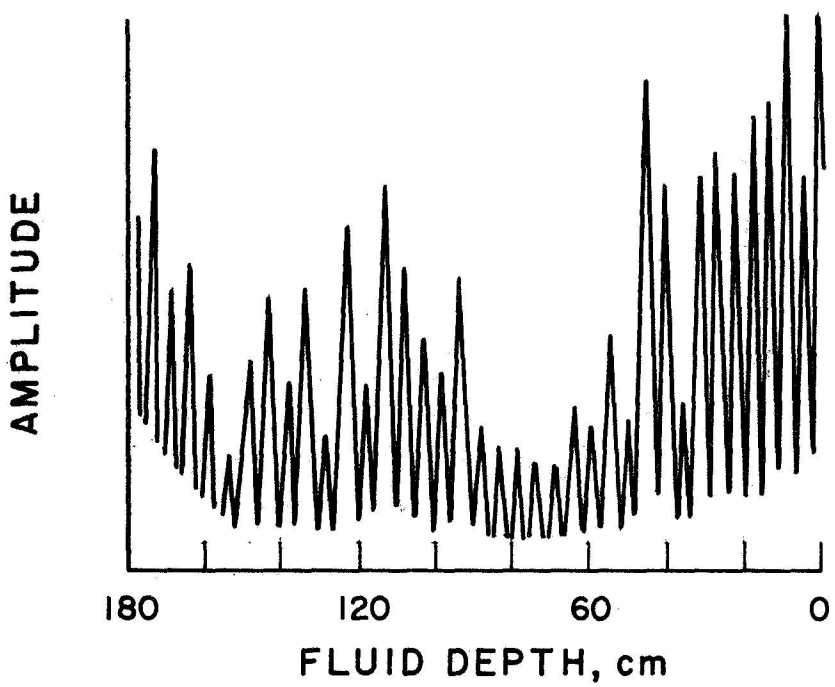

Figure 10. Spectrum Analysis of Frequency Domain Reflections.

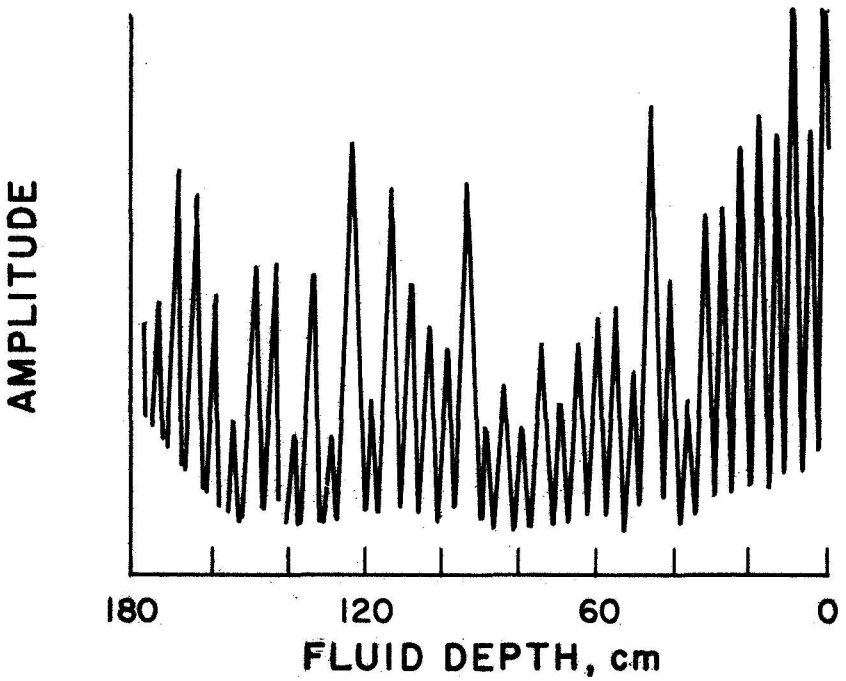

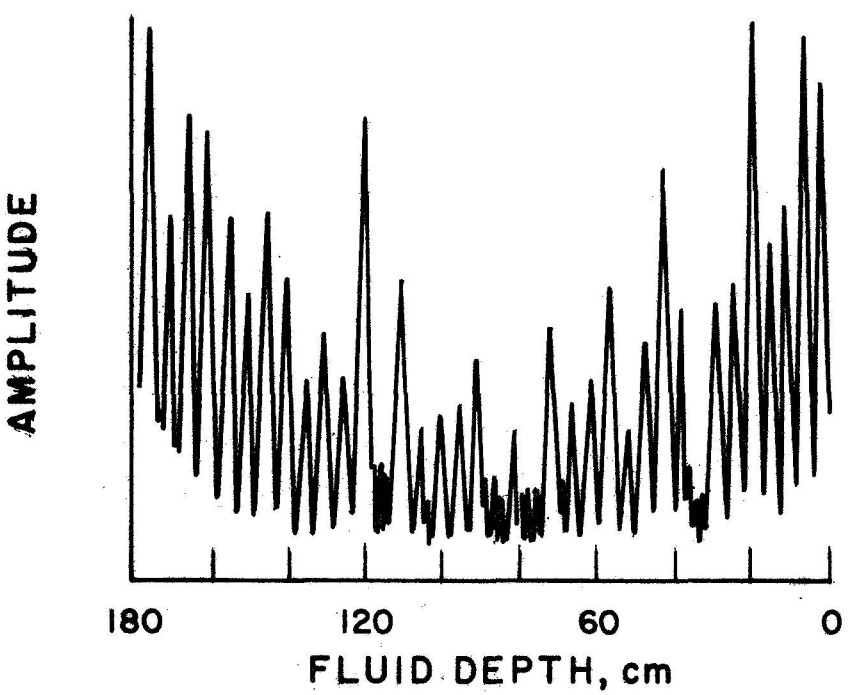

Figure 11. Spectrum Analysis of Frequency Domain Reflections.

with the bottom of the dewar (0 cm) at the right end of the traces. All of these pictures were taken with 180 cm of liquid in the dewar; the liquid-vapor interface is shown by the large amplitude spike at the left side of the pictures.

The top picture of figure 10 was obtained with the cryostat full of normal-boiling liquid hydrogen. Responses from the vapor-liquid interface and from the dewar bottom are clearly shown. The small spikes between these two extremes are probably reflections from bubbles.

The bottom picture in figure 10 was obtained with 40 cm of settled slush in the dewar. Three separate density regions can be distinguished. From zero to 40 cm the fluid is settled slush. From 40 to 90 cm we have homogeneous triple-point liquid, giving a very low reflected signal. This region of uniform density corresponds accurately to the presence of a heavy copper shield which contacts the lower 100 cm of the dewar wall. Above the 100 cm level, the liquid is stratified by convection currents. These are caused by heat leaks and the warmer normal-boiling liquid at the surface. Several significant liquid-liquid interfaces apparently were present between 90 and 180 cm at the instant the picture was taken.

Figure 11 shows pictures taken 10 minutes and 25 minutes after the lower picture of figure 10. After 10 minutes (top picture) the density distributions are still changing. The liquid-slush interface is still apparent at 40 cm, but below this interface the slush is more homogeneous (lower signal) than before. The lower picture of figure 11 shows continued stratification, with a well-defined liquid-liquid interface at 120 cm, the liquid-slush interface still present, and indication of stratified layers present also in the settled slush.

This method of locating regions of changing density in cryogenic fluids appears to have high potential for liquid level indication, and also is fairly good for discrimination of a settled slush level. The readout

instrumentation was not developed beyond the feasibility stage because of time and funding limitations.

3.3 Carbon Film Sensors

Sophisticated point sensors based on change in electrical resistance have been developed by deposition of thin carbon films on substrates of glass or sapphire. A power pulse followed by interrogation of the decay transient yields temperature and fluid phase information. Principal advantages over prior technology of this type are high signal level and fast response time.

The method has been extensively tested for liquid-vapor interface location in hydrogen and nitrogen. Tests performed under the present program have shown that the sensors can also distinguish between triple-point liquid and slush for both nitrogen and hydrogen.

Two carbon film sensors were tested in the density reference system. There was a significant difference in sensor response between the triple point liquid nitrogen or hydrogen and the settled slush, thus indicating that these sensors have good potential as settled slush level indicators. The response to a constant current pulse for both Pyrex and sapphire substrates in hydrogen is shown in figure 12. The initial transient is similar in both triple point liquid and settled slush, indicating that there is a liquid boundary layer surrounding the sensor in the slush. The sensor then attains a higher temperature in the slush, as indicated by the lower voltage across the sensor.

There appears to be an oscillation in the temperature of the sensor. This oscillation occurs at about eight cycles per second, independent of the substrate or power input between 0.05 watts and 0.5 watts. These effects in slush were not completely understood and further tests were designed to clarify the heat transfer which occurs between the sensor and the slush.

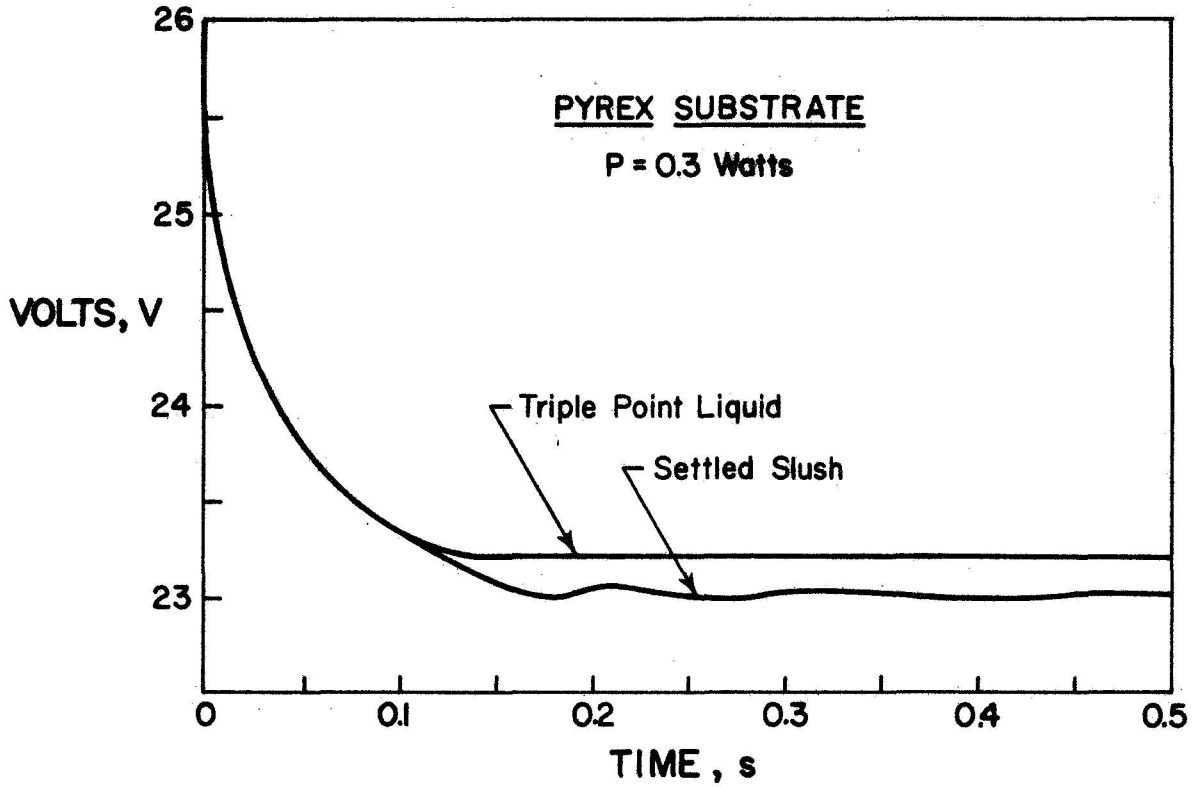

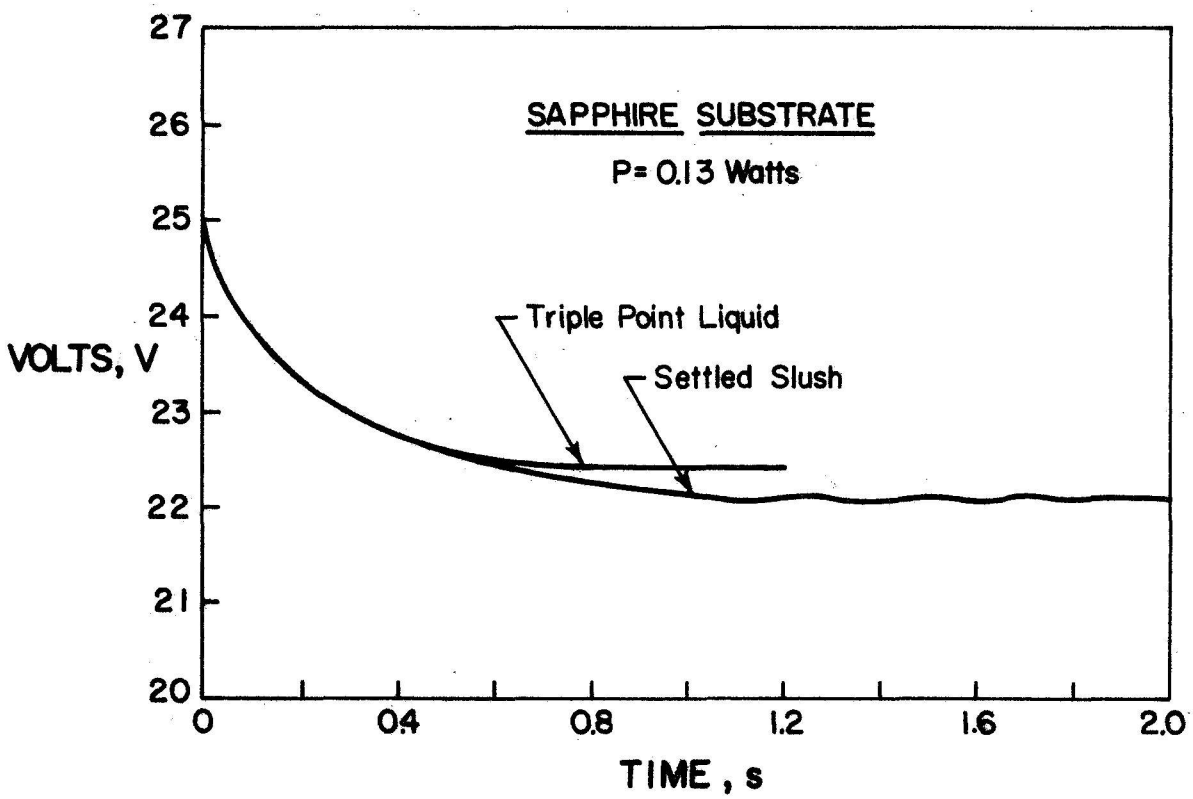

Figure 12. Carbon Film Sensor Response in Liquid and Slush Hydrogen.

Figures 13 and 14 show temperature responses obtained for six unmatched carbon film sensors which were located in the one-cubic-meter dewar, as shown in figure 3. The temperatures were obtained by maintaining the liquid hydrogen in equilibrium with its vapor at various pressures. The temperature response curves are useful for analysis of the slush-discriminating transients. These curves also make possible a quick and convenient check of liquid hydrogen temperature, and therefore density, in the vicinity of each sensor before reaching triple-point. After the hydrogen is pumped to triple-point and solids are formed, stratification of temperature and density develops quickly in the liquid above the settled slush; the resistance-temperature curves have proven useful in following this action.

The sensors were all able to discriminate between triple-point liquid and settled slush by virtue of change in transient characteristics, but the regular 8 Hz oscillatory transients previously observed for the two sensors tested in the Density Reference System were not reproduced. The sensor mounting was changed so that the sensors were at least three inches from any supporting brackets, and the oscillations reappeared although they were not as pronounced and regular as those observed in the density reference system.

Work on the carbon film sensors and the heat transfer mechanism causing the oscillations is being continued under a contract extension.

4. Total Mass Gauging

The resonant cavity method is uniquely well-suited for total mass gauging in a tank of simple geometry which contains a minimum of interfering penetrations or irregularities. Capacitance probes respond to the total mass of fluid between the electrodes, and hence will give total tank

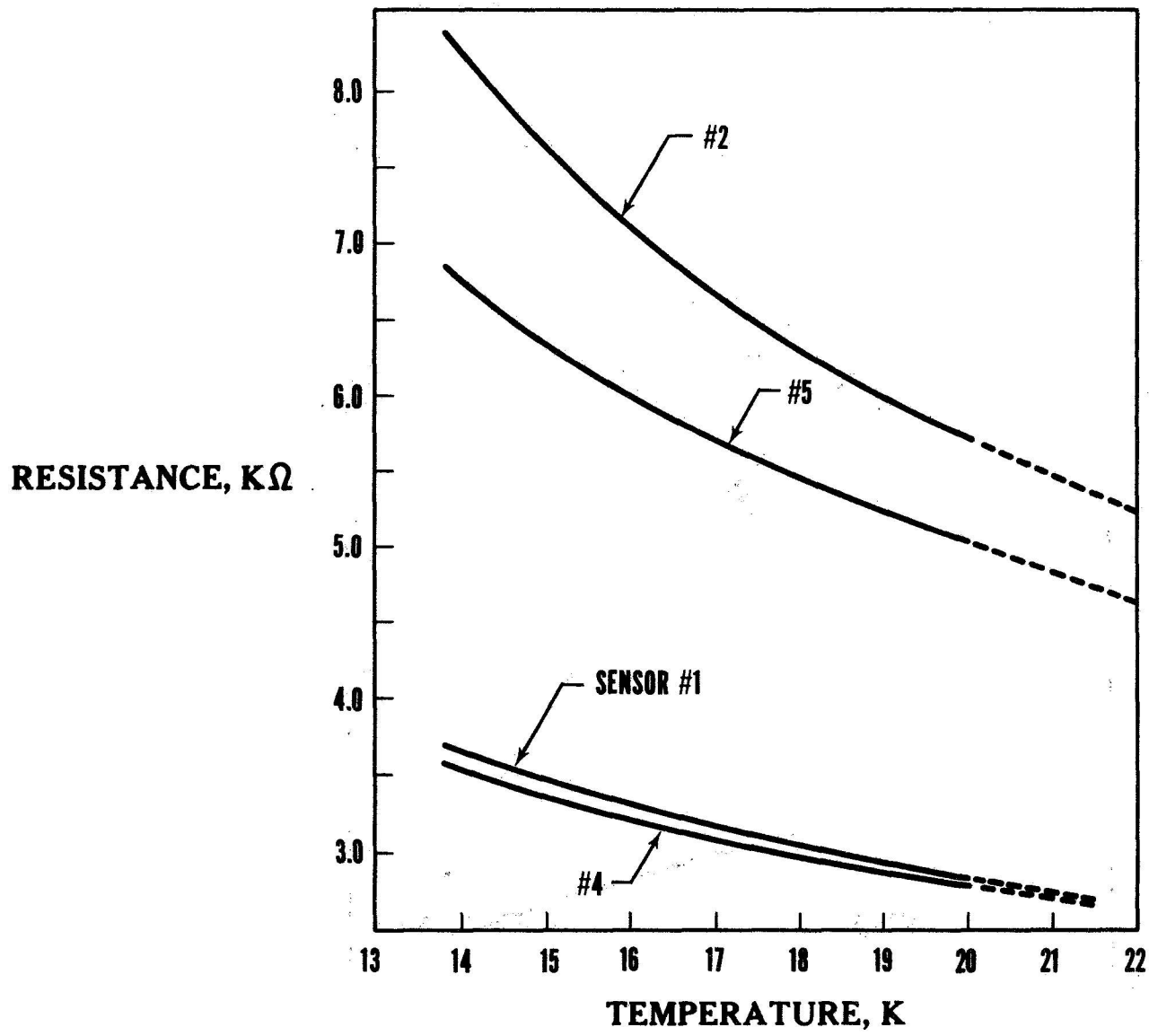

Figure 13. Carbon Film Thermometry Results in Liquid Hydrogen.

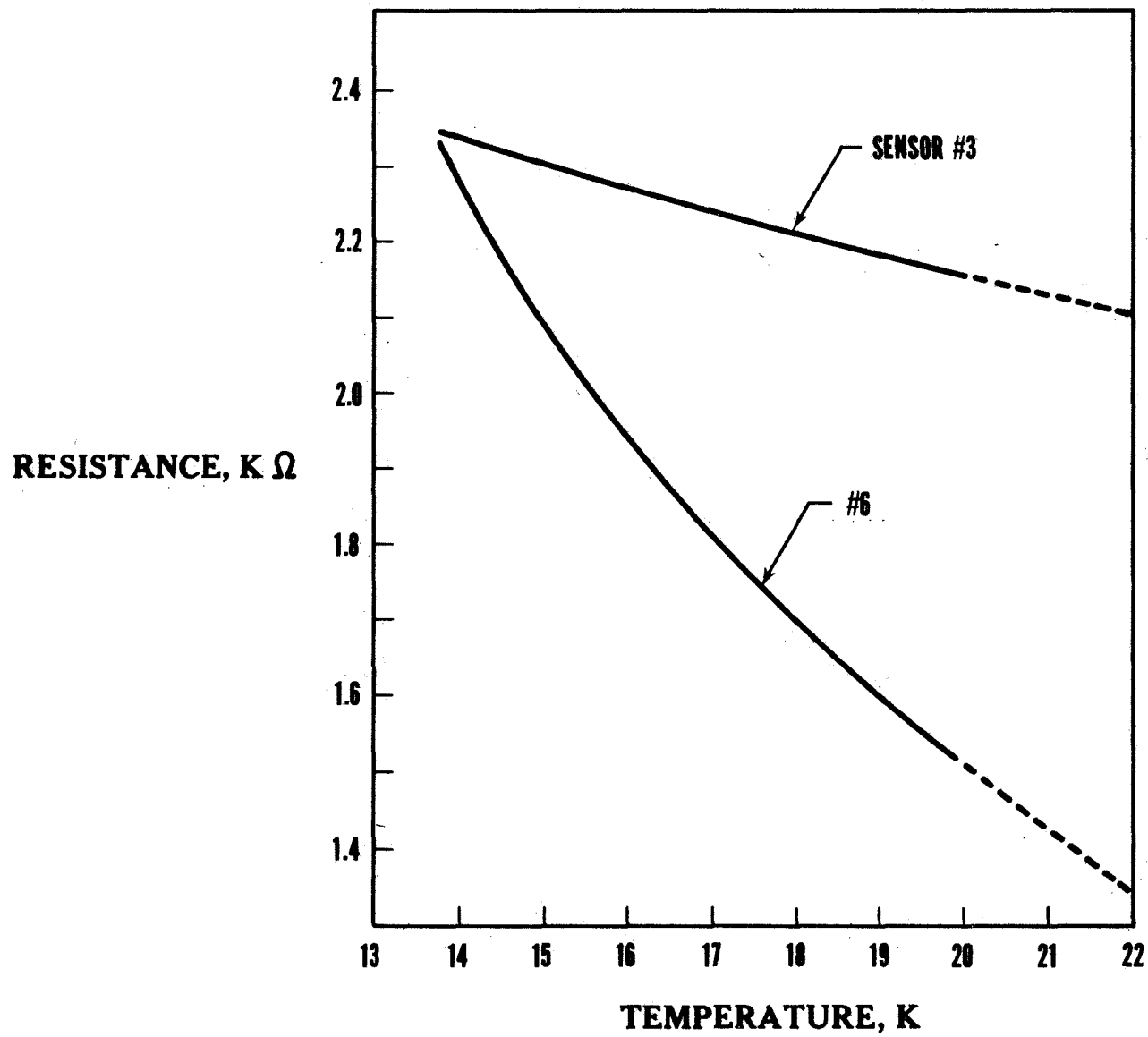

Figure 14. Carbon Film Thermometry Results in Liquid Hydrogen.

content after multiplication by the proper tank-geometry factor or series of factors. The microwave propagation method of dielectric constant measure is approximately equivalent to the capacitance methods, with the advantage of easier representative sampling of the tank contents.

These three methods will be discussed in the present section.

4.1 Resonant Cavity Experiments

Experiments utilizing the resonant cavity method of mass gauging were performed in smaller cylindrical and spherical vessels as well as in the one-m^3 upgrading vessel. The method of the experiments is illustrated in figure 15. The TE_{112} mode was excited and detected by a pair of 0.5-inch rectangular "loop" antennae. If the quantity of dielectric material in the container changes, the resonant frequency of the cavity changes. The objective is to measure the resonant frequency to determine the quantity of fluid present.

The resonant frequency was first measured with the container empty. The measurement starts with the switch in the "test" position. The signal frequency was adjusted until maximum amplitude was shown on the spectrum analyzer. Then the signal source was switched to the frequency meter and the frequency read as accurately as possible. This procedure was repeated as increments of liquid were added or removed from the container. For the smaller containers, the reference mass was determined either by placing the vessel on a platform balance during the experiment or by making an independent measurement of the liquid level.

Figure 16 shows results obtained with liquid nitrogen in a 0.05 m^3 cylindrical container having a diameter of 33 cm. The periodic nature of the response is caused by interference with waves reflected from the

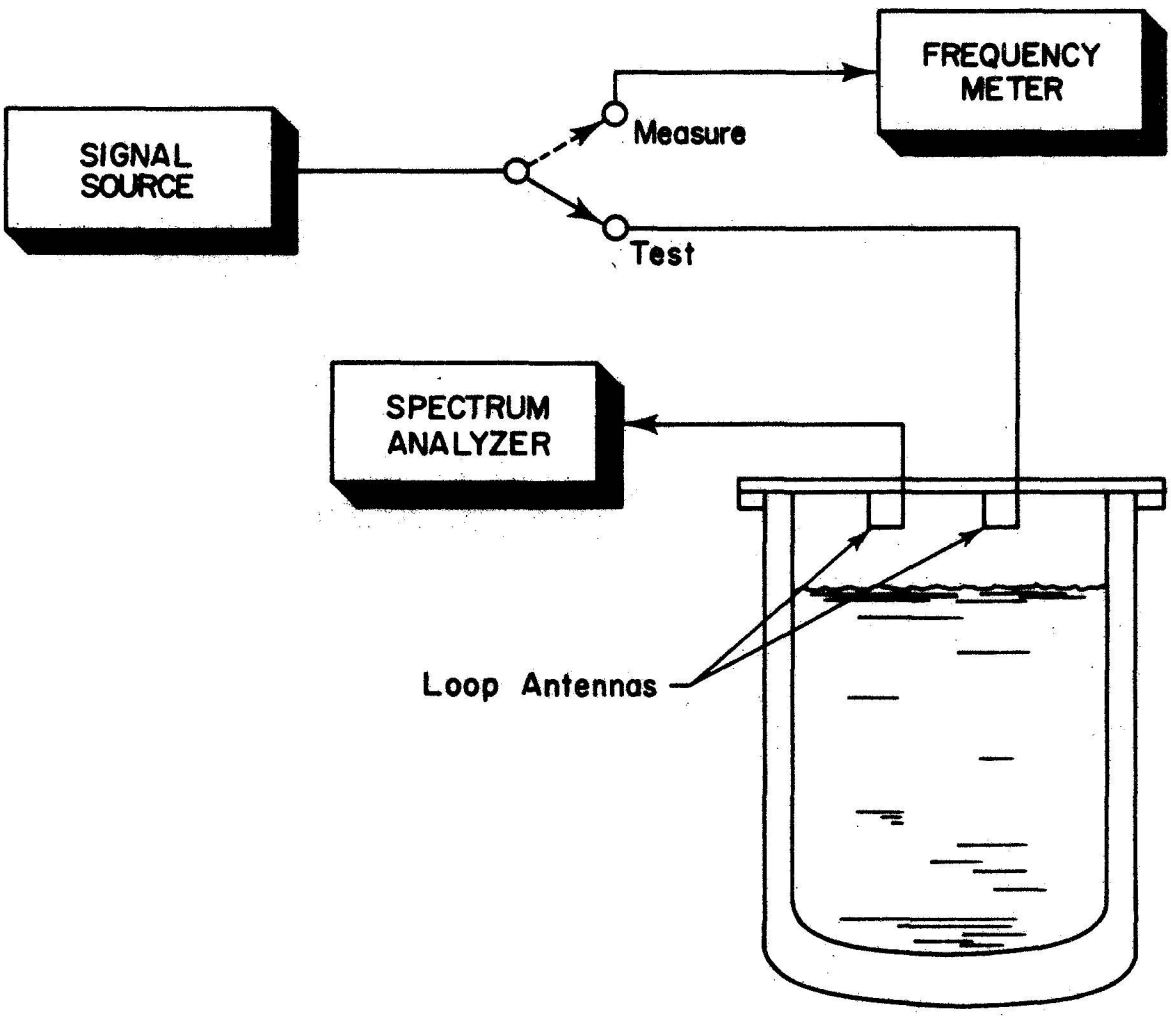

Figure 15. Resonant Cavity Method.

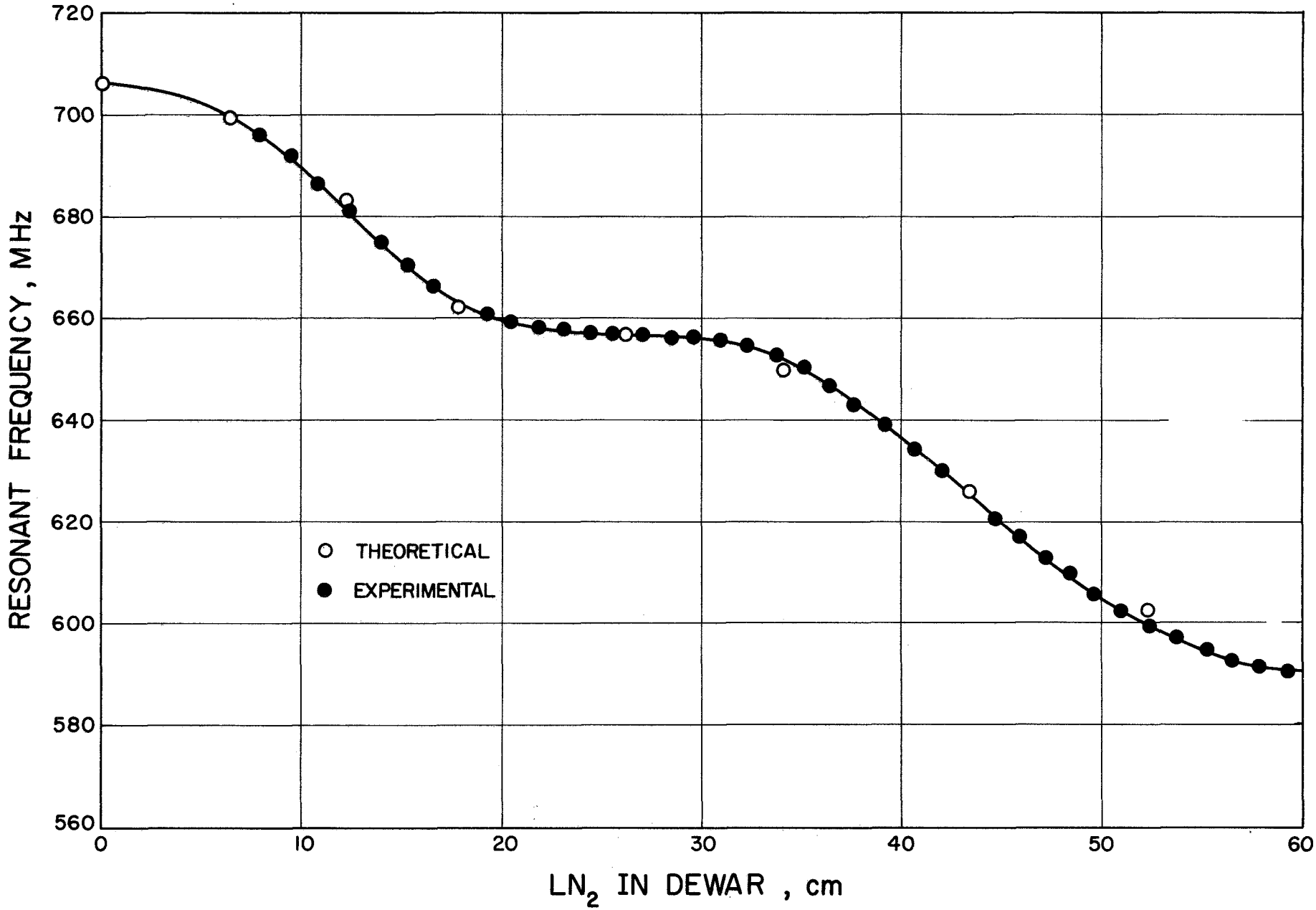

Figure 16. Resonant Cavity Results, Cylindrical Dewar.

vapor-liquid interface. The effect of the reflected signal can be calculated; a number of calculated points are shown on figure 16.

Sensitivity of the system was limited by the frequency-measuring ability of the equipment used. This was approximately ±100 kHz. Since empty-to-full resulted in a frequency change of about 110 MHz, the sensitivity was on the order of 0.1 percent of the total mass on the steeper portions of the curve and less on the flat portions.

Sloshing of the liquid in the partially-filled container had a negligible effect on the resonant frequency. Agitation of the liquid surface changed the amplitude of the signal, but large variations in amplitude are tolerable in this arrangement because the mass is measured in terms of frequency.

A second experiment, using a spherical container, is illustrated in figure 17. The cavity was a copper sphere having a diameter of 48 cm. A single straight wire about 1 cm long was used as an antenna to simultaneously excite the cavity and detect the resonant frequency. The sphere was insulated with a hollowed-out block of rigid foam, and the "dewar" placed on a platform balance to obtain the reference mass.

Results are shown in figure 18. Sensitivity was similar to that obtained with the cylindrical cavity, primarily because the same frequency meter was used. Repeatability of the measurement was limited by inaccuracy of the balance weight setting and by accumulation of liquid air in the foam insulation. The largest spread in frequency data during three empty-to-full runs was 0.3 percent. The "full" condition was about 45 kg (100 lb) of liquid nitrogen.

The third experiment with the resonant cavity method was carried out in the one-m^3 liquid and slush hydrogen upgrading vessel. A pair of

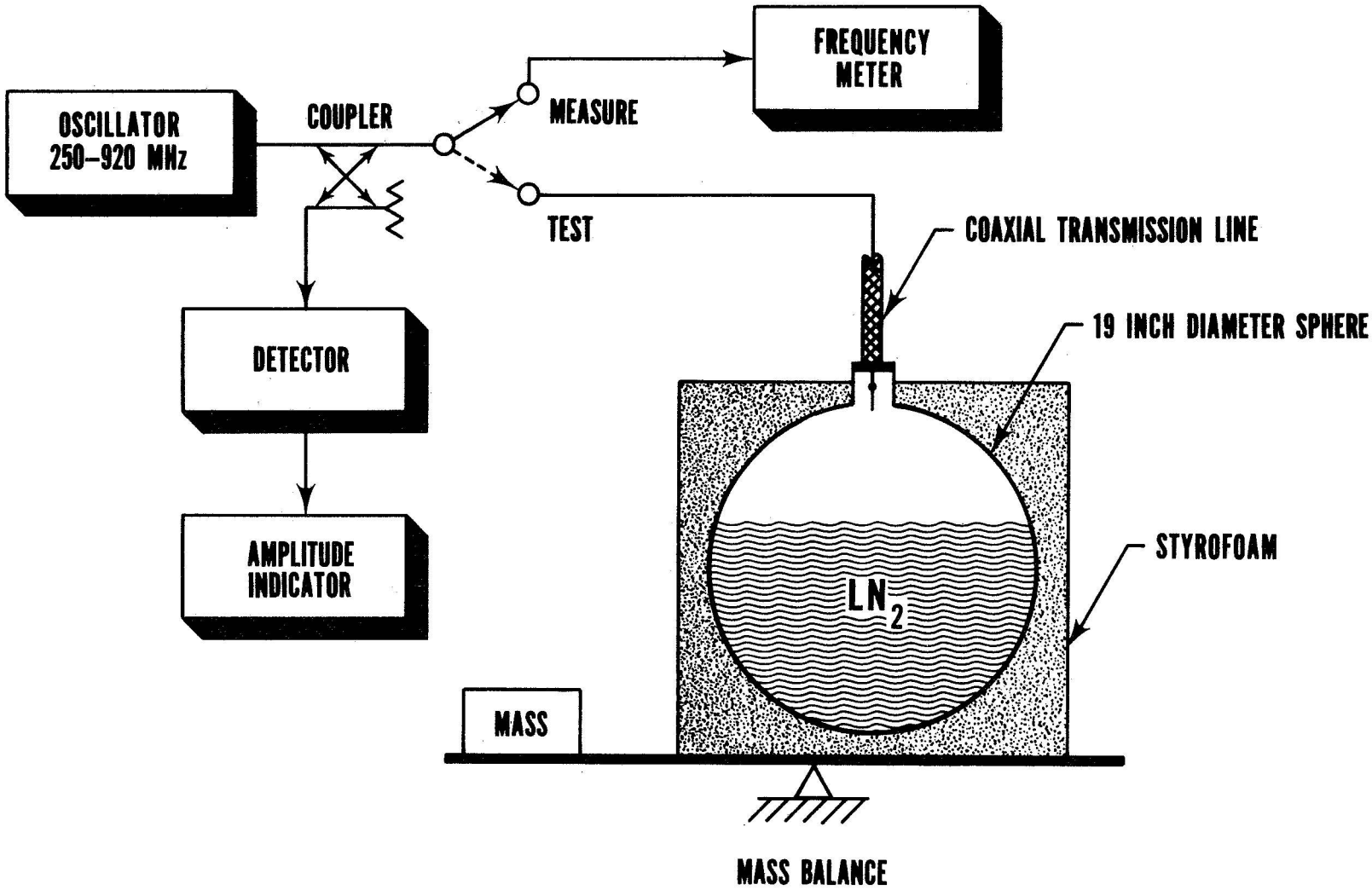

Figure 17. Resonant Cavity Experiment, Spherical Dewar.

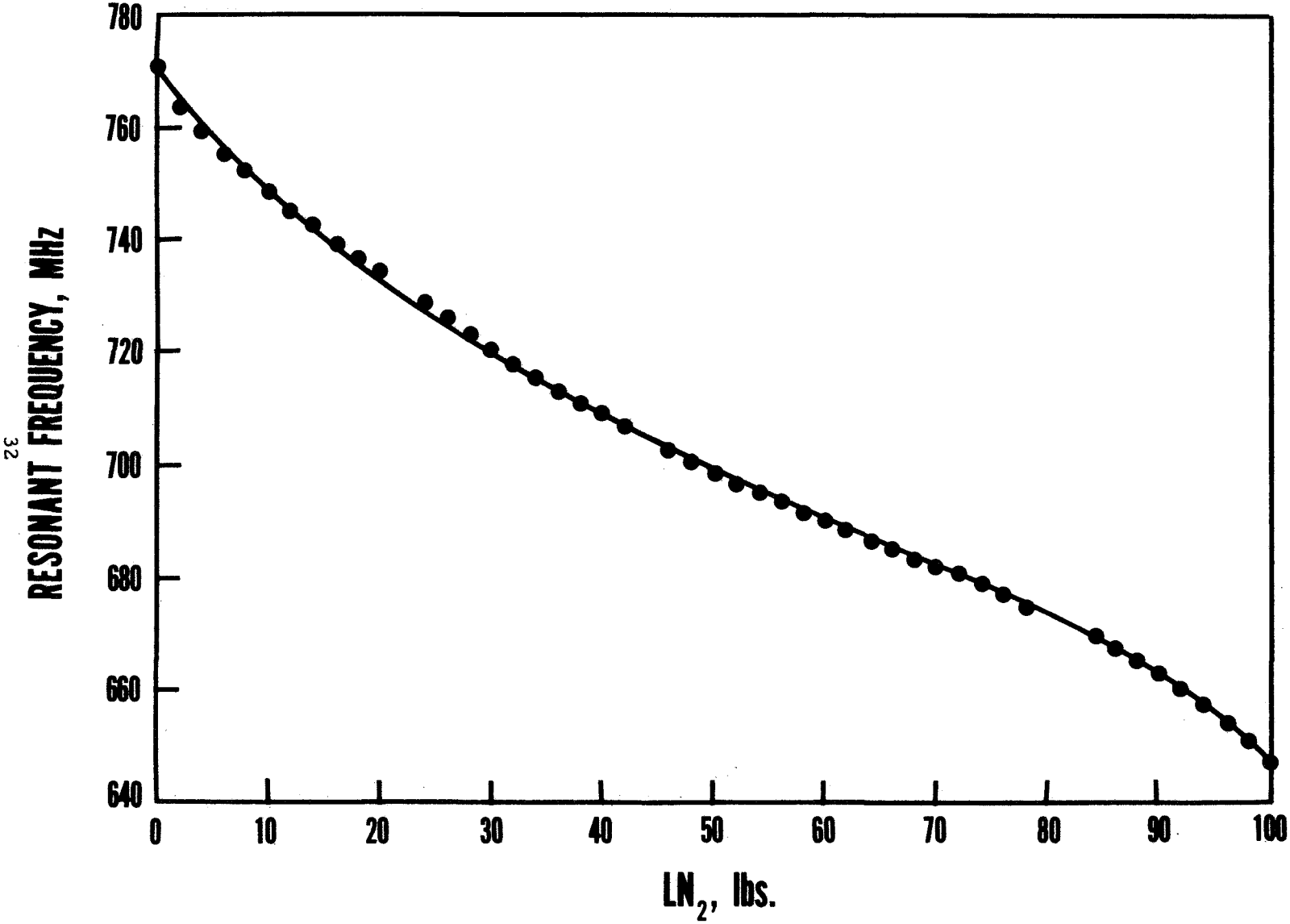

Figure 18. Resonant Cavity Results, 48 cm Diameter Sphere.

small loop antennae were located under the top plate of the dewar, as shown in figure 3. The experiment was designed to:

1) Determine if a large vessel containing various penetrations and obstructions can be resonated;
2) Observe how the resonant cavity technique responds to changes in density of the fluid in the vessel.

Results obtained for near normal-boiling and near triple-point liquid are shown in figure 19. It is apparent that resonance was achieved in spite of the unfavorable conditions noted above, and a curve similar to those previously reported for liquid nitrogen in uncluttered cylindrical and spherical containers was obtained. The expected curve would not be as regular as that shown in figure 16 because of the many interfering surfaces inside the cavity. Marginal resolution of the frequency meter accounts for much of the data scatter. A difference was obtained between the two liquid densities, i. e., lower resonant frequency for higher density at a given liquid level, but scatter prevented any more quantitative evaluation.

4. 2 Resonant Cavity Analysis

A considerable amount of mathematical analysis of the resonant cavity method of mass gauging was done during the contract period. Many of the mathematical details will be found in Appendix A. The present section outlines the calculations and discusses the conclusions which were reached.

The following properties have been established:

1) In a loss-free cavity uniformly filled with a fluid with dielectric constant, ϵ, the resonant frequency is given by

$$f_{np} = \frac{u_{np}}{a\sqrt{\mu\epsilon}} \tag{4-1}$$

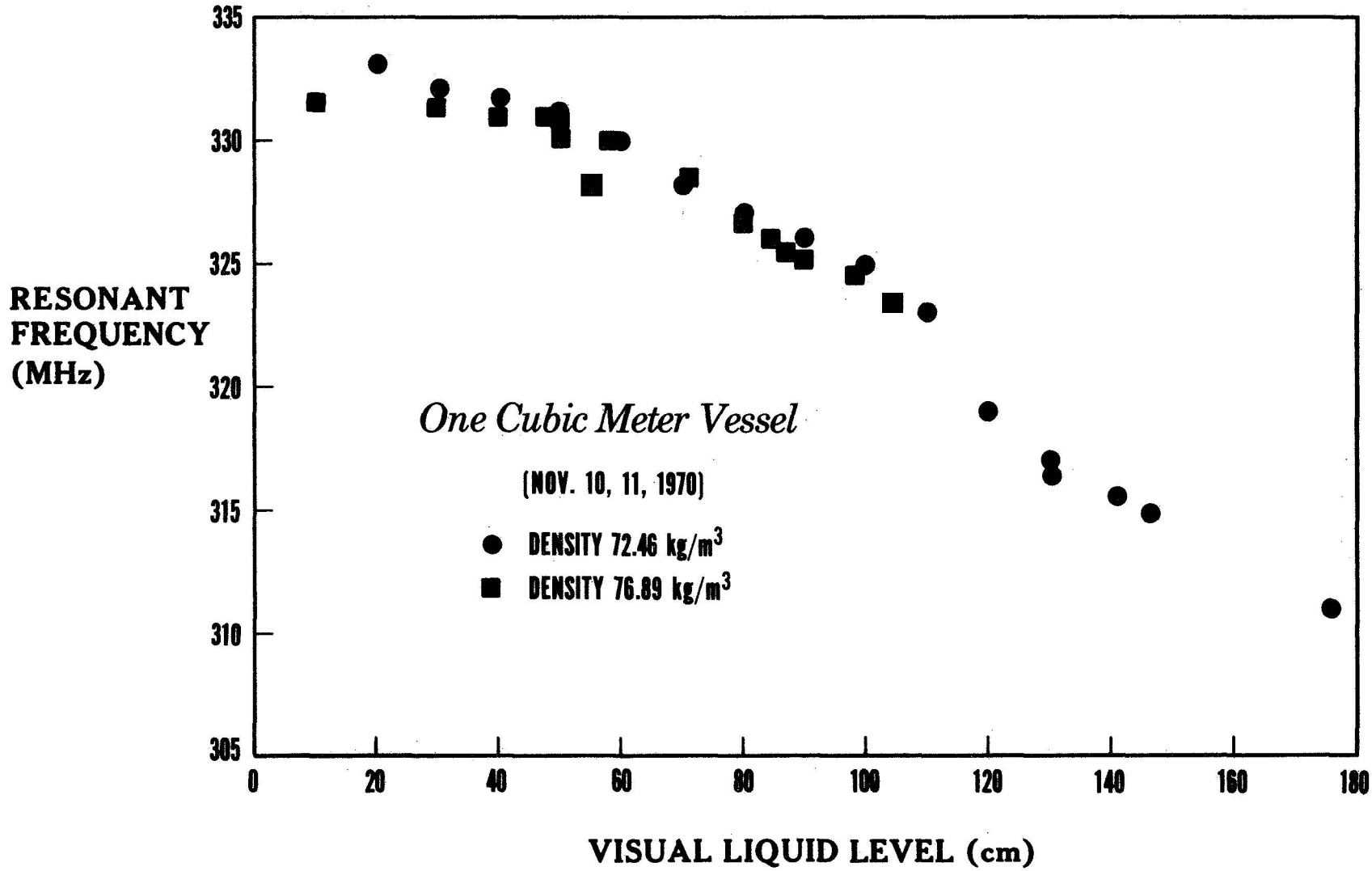

Figure 19. Resonant Cavity Results in One Cubic Meter Vessel with Interfering Obstructions.

where a is the radius of the cavity and u_{np} are eigenvalues which depend only on the mode of vibration. If the magnetic permeability, μ, is known then the frequency of each mode is related to ϵ, and ϵ is related to the density, ρ, by the Clausius-Mossotti relation,

$$\frac{\epsilon - 1}{\epsilon + 2} = P\rho \tag{4-2}$$

The volume, $V = \frac{4}{3}\pi a^3$, is known; it follows that the resonant frequency of each mode determines the total mass by

$$M = \frac{1}{CV}\left(\frac{u_{np}^2 - f_{np}^2 a^2 \epsilon_o \mu}{u_{np}^2 - 2f_{np}^2 a^2 \epsilon_o \mu}\right). \tag{4-3}$$

2) For the uniform cavity, the field configurations for each mode have been calculated in closed form and the corresponding eigenvalues u_{np} have been tabulated for ten of the lowest frequency modes. The resulting calculated values for f_{np} (for the three lowest TM modes and the lowest TE mode) have been verified experimentally to within one percent, using an air-filled 48 cm diameter copper cavity at room temperature. The modes in spherical geometry are highly degenerate, resulting in widely spaced frequencies among distinctly different lower order modes. This makes it easy to monitor several of the lowest order modes simultaneously as the cavity is being filled without the bothersome effect of "mode crossing" which is prevalent in other geometries.

3) Under normal gravity and two-phase fill conditions, the frequency vs. mass for liquid nitrogen has been obtained on the 48 cm diameter spherical dewar (figures 17 and 18) for the second lowest TM mode. This data has also been obtained by Lockheed[9] on their 5-foot diameter "nearly spherical" dewar for the lowest three TM modes,

as shown in figures 4-7 of their report. The data scale qualitatively rather well from the 48 cm cavity to the 5-foot cavity. Small quantitative differences are probably due to the geometry of the 5-foot cavity being a short cylinder with spherical caps.

4) In order to anticipate scaling effects, the Q of the cavity was calculated as a function of cavity radius in the limit $Q \gg 1$. For the TM modes

$$Q_{mnp} = \sqrt{\sqrt{\frac{\mu}{\epsilon}}\pi\sigma a}\left[\sqrt{u_{np}} - \frac{n(n+1)}{\left(u_{np}\right)^{3/2}}\right] \tag{4-4}$$

and for the TE modes

$$Q_{mnp} = \sqrt{\sqrt{\frac{\mu}{\epsilon}}\pi\sigma a\, u_{np}} \tag{4-5}$$

so that Q increases with increasing radius. This is borne out experimentally by the fact that the resonant line widths for the Lockheed 5-foot cavity (figure 4-6 of the Lockheed report) appear at least as narrow as the line widths for the 48 cm cavity. If there are detrimental scaling effects, they must be found in either the coupling to the cavity or the external circuitry.

5) For zero gravity (spherical symmetry) and two-phase (vapor-liquid) conditions, the frequency vs. mass has been calculated in closed form for constant density in the liquid phase. A computer program has been written which plots the zero-g frequency vs. mass for the TM modes. It is assumed that liquid will be next to the walls of the sphere, with vapor in the center. Plots have been obtained for both liquid nitrogen and liquid hydrogen under various densities for the first four TM modes (see figs. A1 through A5). Although the "completely full" frequencies differ between hydrogen and nitrogen according to equation (4-1), the normalized curves differ very little.

Qualitative comparison between these curves and the normal g experimental data gives a rough idea of the effect of changing the geometry of the liquid (see fig. A5). The discrepancy between these two geometries, for the most mass values, goes down for the higher modes. This is due to the tendency of the high field regions in the higher modes to be partitioned more uniformly throughout the cavity. However, except for the lowest mode, the curves for these two geometries cross, causing the discrepency at some particular mass values to be smaller for lower modes than for higher modes. These conclusions are in qualitative agreement with the zero-g simulations performed by Lockheed for cylindrical cavities.

6) A small silver cylindrical cavity was partially filled with liquid nitrogen and shaken vigorously. This resulted in only a small jiggle in the resonant frequency. This is in qualitative agreement with Lockheed's data which show that sloshing gives a relatively small discrepancy as compared to more gross geometry changes.

4.2.1 Conclusions

1) If the fluid geometry is known and either the volume or density is known, then the total mass can be determined unambiguously from the resonant frequency of any mode provided that a proper calibration curve is given.

2) If the fluid geometry is known and both density and volume are unknown, there is an intrinsic uncertainty in the resonant frequency vs. mass relation which is on the order of 20 percent of the uncertainty in the density. If more than one mode is measured simultaneously, it is sometimes possible to completely eliminate this uncertainty (see Appendix A).

3) If the geometry is not known, then for a given frequency in a given mode there is an intrinsic uncertainty in the total mass. This uncertainty appears to be different for different modes. For each mode, there will be two fluid geometries which will give the upper and lower limits of uncertainty. These geometries are not known, but it is certain that they will be hard to simulate in practice, especially for the higher modes, and therefore these limiting geometries will be highly improbable fluid geometries. Hence, there will be practical limits to the uncertainty in mass which will be obtained by excluding certain highly improbable fluid geometries. This practical uncertainty will be smaller than the theoretical uncertainty.

If the uncertainty is intolerable then some effort must be made to determine the geometry, at least approximately. Three methods have been suggested:

(1) Multiple coupling points. For example, suppose three coupling antennae were located in three orthogonal directions at the surface of the sphere. If all three points induced the same resonant frequency, then spherical symmetry would be assured. If the three coupling antennae induced different frequencies then it seems reasonable that certain asymmetries could be deduced which would decrease the uncertainty in total mass.

(2) Multiple Modes. Since each mode has a different field geometry it seems reasonable that geometry effects can be deduced by comparing the resonant frequencies of two or more modes. This is already apparent in discriminating between normal-g and zero-g geometries. The mode degeneracies of spherical geometry make this approach more feasible for spherical cavities than for other geometries. It should be emphasized that this procedure is not the "mode counting" technique used by Bendix[10].

(3) Point sensors such as carbon film phase discriminators could be placed at points in the cavity where the field is expected to be significantly higher or lower than the average field. These would help determine the geometry as well as provide a weight function for the determination of frequency vs. mass.

Specific methods for synthesizing two or more information inputs, as required in all of these geometry-determining procedures, have not been worked out in detail. The methods are given as suggestions for further work on the resonant-cavity mass-gauging techniques.

4.3 Capacitance Methods

This section is a study of mass gauging by capacitance methods. The first part will be theoretical analysis of two simple capacitance configurations. The second part will be a discussion of the capacitors used and results obtained for mass gauging in the one-m^3 test vessel.

4.3.1 Mass Gauging by Capacitance Measurement

Modern capacitance-measuring bridges and development of the guarded three-terminal capacitor design have made it possible to measure capacitances with an accuracy of ±0.01 percent in the presence of 1000 times as much lead capacitance. These advances make it possible to obtain the capacitance between two or more widely separated electrodes in a storage vessel. The effective dielectric constant obtained by these measurements will depend mainly on the total mass of dielectric within the container, but also, to a lesser degree, on the geometrical configuration of the dielectric with respect to the geometry of the electrodes.

4. 3. 1. 1 Dewar Gauging Experiment

A simple test was conducted to investigate the feasibility of determining total storage vessel content by means of capacitor electrodes fastened to the inner walls. A 33 cm diameter by 61 cm deep cylindrical stainless steel dewar was placed on a platform balance. Insulating paper and aluminum foil electrodes were taped to the inside. Each electrode was 34. 5 cm wide by 40. 6 cm long. Air capacitance was measured and found to be 1. 219 pf. When the vessel was filled with liquid nitrogen, the capacitance was 1. 790 pf. The liquid level sensitivity was found to be 0. 012 pf per cm, and a change of 0. 002 pf could be measured. Thus, a liquid level change of 1. 7 mm could be detected, representing 0. 51 percent of the volume (and mass) of the liquid bracketed by the capacitor.

A plot of mass vs. capacitance was obtained; this is shown in figure 20. Except for a slight fringing effect near the top and bottom of the capacitor, the plot is linear within the accuracy of the experiment.

One reason for performing the above experiment was to explore the effect of the non-uniform electric field by moving a styrofoam ball (simulating a vapor pocket such as might form at low gravity) around in the liquid between the electrodes. Results were interesting and led us to initiate some calculations of various geometrical configurations of the dielectric for several geometries of the electrodes. These calculations are given below and should lead to a better understanding of the problem of mass gauging by capacitance methods.

4. 3. 1. 2 Geometrical Effects

As previously stated, the geometrical configuration of the dielectric with respect to the geometry of the electrodes represents an uncertainty between the capacitance and the total mass. We will discuss two

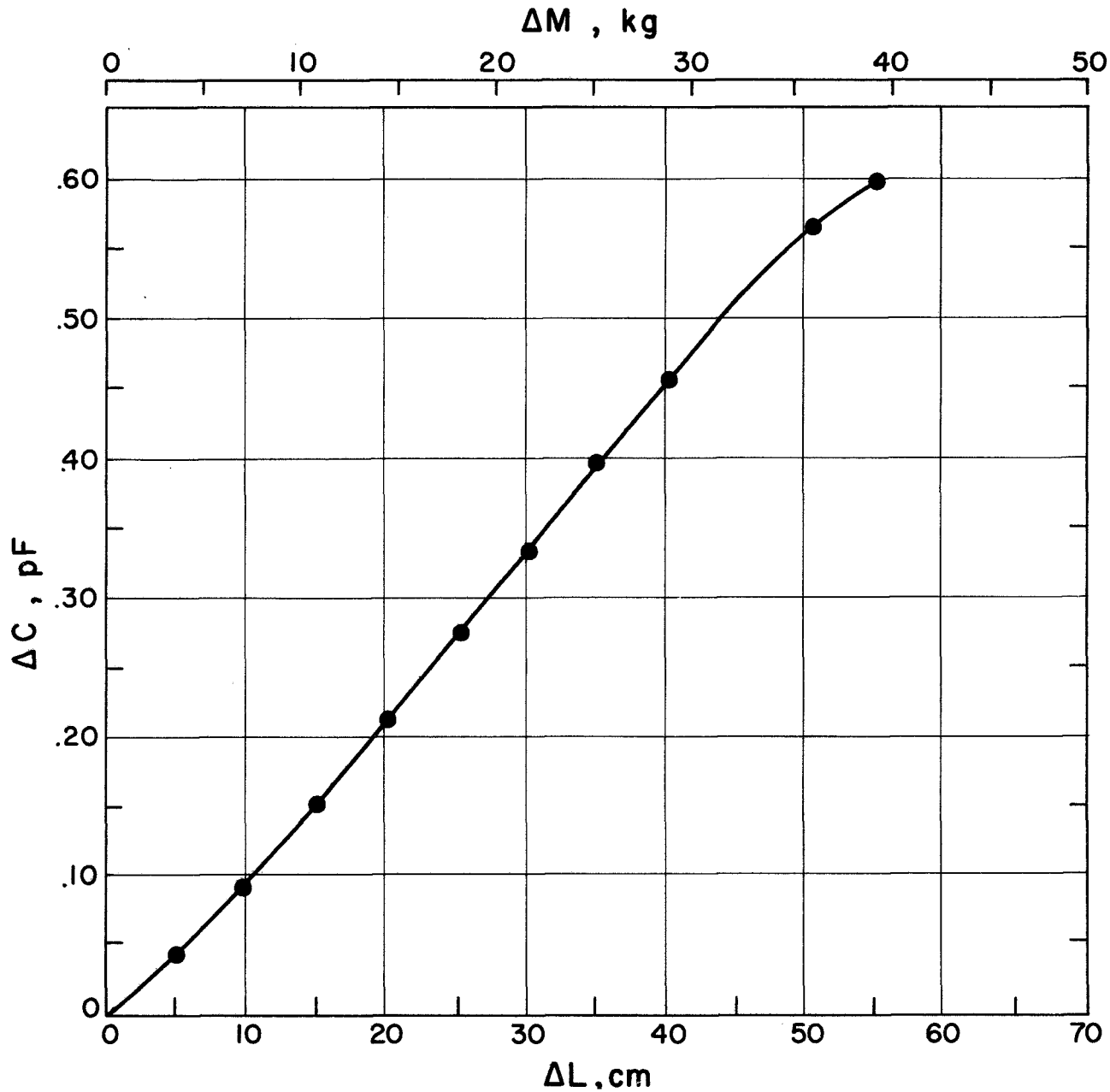

Figure 20. Mass Gauging with Capacitor Electrodes Fastened to Inner Walls of Dewar.

methods by which this uncertainty can be minimized: 1) by placing the electrodes so that the electric field in the absence of this dielectric is as uniform as possible over the container volume; and 2) by placing point phase sensors in the regions of the container where the field is significantly higher or lower than the average field.

It is shown in Appendix B that upper and lower bounds on the capacitance between two electrodes are given by

$$\frac{\int_S \varphi_o \nabla \varphi_o \cdot dS}{\int_V \frac{1}{K} |\nabla \varphi_o|^2 dV} \leq \frac{C}{C_o} \leq \frac{\int_V K |\nabla \varphi_o|^2 dV}{\int_S \varphi_o \nabla \varphi_o \cdot dS} \tag{4-6}$$

where C_o is the empty space capacitance, φ_o is the empty space potential, V is the open space not occupied by the electrodes, S is the surface bounded by electrodes, and K is the dielectric constant which may vary throughout V; $\nabla \varphi_o$ is the empty space electric field. Several qualitative conclusions may be obtained from these inequalities:

1) The upper and lower bounds given by (4-6) are the "best possible" when the geometry of the dielectric is completely unknown; i. e., there are electrode geometries such that for any given dielectric volume the upper and/or lower bounds may actually be attained depending on the geometry of the dielectric.

2) For a given volume of dielectric the difference between upper and lower bounds is minimized when the electric field, $\nabla \varphi_o$, is uniform throughout V.

3) When V is partially filled with dielectric and the field is not uniform, both the upper and lower bounds are the highest when the dielectric is in the low field region. This conclusion makes it possible to

decrease the uncertainty in capacitance vs. mass when any information at all is given concerning the dielectric geometry.

4) For a given geometry, the difference between upper and lower bounds decreases and approaches zero as the dielectric susceptibility, χ, gets small ($K \equiv 1 + \chi$). This minimizes the uncertainty for dielectrics such as liquid hydrogen where $\chi \approx 0.23$.

These conclusions will be demonstrated for two simple geometries, the parallel plate capacitor and the concentric sphere capacitor, and are expected to hold for more complicated electrode geometries.

Parallel Plate Capacitor

Suppose the surface area of each plate is A and the distance between plates is d, where d is small enough that edge effects may be neglected. The volume V is equal to Ad. Let a dielectric with uniform dielectric constant K fill a volume V'. Let f be the fraction of the total space occupied by the dielectric $\left(f = V'/V\right)$. $\nabla\varphi_o$ is calculated by letting $\varphi_o = 0$ on one plate and $\varphi_o = \psi$ on the other plate. It follows that $\nabla\varphi_o = \psi/d$ uniformly throughout V. (Here, because edge effects are neglected, it is assumed that $\nabla\varphi_o = 0$ outside of V.) The integrals in (4-6) are easily evaluated:

$$\int_V K|\nabla\varphi_o|^2 dV = (\psi/d)^2\left[KV' + (V - V')\right]$$

$$\int_V \frac{|\nabla\varphi_o|^2 dV}{K} = (\psi/d)^2\left[\frac{V'}{K} + (V - V')\right]$$

$$\int_S \varphi_o \nabla\varphi_o \cdot dS = \frac{(\psi)^2}{d}A = (\psi/d)^2 V. \qquad (4\text{-}7)$$

The inequality (4-6) becomes

$$\frac{K}{f + (1 - f)K} \leq \frac{C}{C_o} \leq Kf + (1 - f). \tag{4-8}$$

Expressed in terms of the susceptibility, χ,

$$\frac{1 + \chi}{1 + (1 - f)\chi} \leq \frac{C}{C_o} \leq f\chi. \tag{4-9}$$

These bounds are plotted in figure 21 for values of χ corresponding to LH_2 and LN_2 showing that the uncertainty in C is small if χ is small. The upper and lower bounds are assumed when the geometry of the dielectric is as in figure 21(a) and 21(b), respectively. For example, in figure 21(b), since $\psi = \int_o^d \nabla\varphi dx$ and $K\nabla\varphi$ is continuous at the dielectric interface, it follows that

$$\nabla\varphi = \begin{cases} \dfrac{1}{f + (1 - f)K} & 0 \geq x \geq fd \\[2ex] \dfrac{K}{f + (1 - f)K} & fd \geq x \geq d \end{cases}$$

and

$$\frac{C}{C_o} = \frac{\int_V K|\nabla\varphi|^2 dV}{\int_V |\nabla\varphi_o|^2 dV}$$

$$= \frac{A}{V\left[f + (1 - f)K\right]^2} \left[\int_o^{fd} Kdx + \int_{fd}^{d} K^2 dx\right]$$

$$= \frac{K}{f + (1 - f)K}.$$

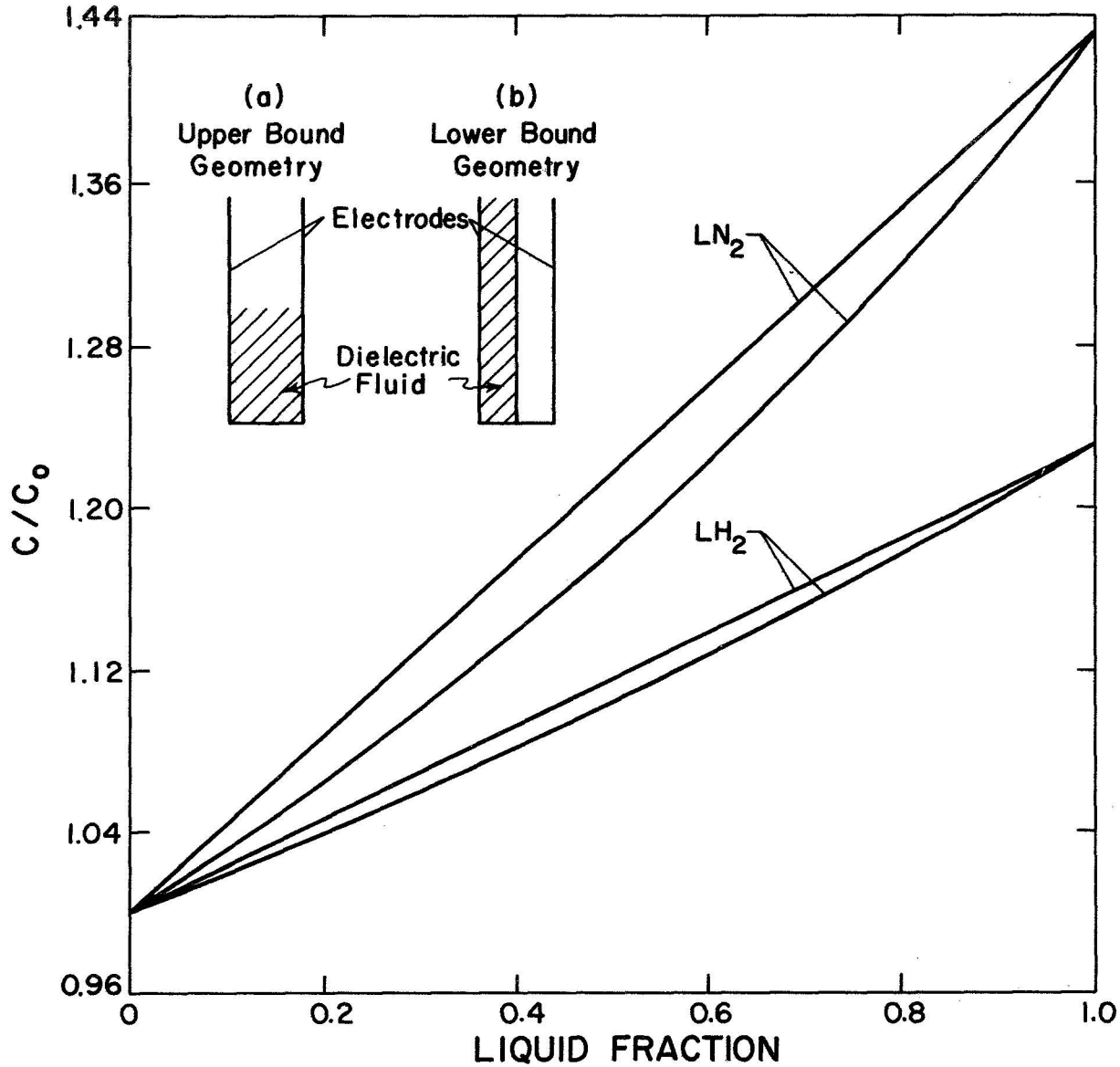

Figure 21. Upper and Lower Bounds for Parallel Plate Capacitors.

Similarly, the upper bound is obtained directly from figure 21(a) by noting that for this case, $\nabla\varphi = \nabla\varphi_o = \psi/d$ uniformly throughout V.

Concentric Sphere Capacitor

Suppose the center ball has radius a and the outer shell has radius b. The total volume inside is $V = 4/3\,\pi\,(b^3 - a^3)$. Let r be the radial distance from the center and $\varphi_o = \psi$ at $r = a$ and $\varphi_o = 0$ at $r = b$, then $\nabla\varphi_o = k/r^2$ where $k = \psi ab/(b-a)$. Suppose the capacitor is partially filled with dielectric of volume V' and dielectric constant K. When the dielectric is in the high field region, near the center ball, the dielectric forms a hollow sphere of inside radius, a, and outside radius $r_o = \left[(b^3 - a^3)f + a^3\right]^{\frac{1}{3}}$, where $f = V'/V$. The integrals in (4-6) become

$$\int_V K|\nabla\varphi_o|^2 dV = 4\pi\int_a^{r_o} K\frac{k^2}{r^2}\,dr + 4\pi\int_{r_o}^{b}\frac{k^2}{r^2}\,dr$$

$$= 4\pi k^2\left[K\left(\frac{1}{a} - \frac{1}{r_o}\right) + \left(\frac{1}{r_o} - \frac{1}{b}\right)\right]$$

$$\int_S \varphi_o\nabla\varphi_o\cdot dS = \psi\frac{k}{a^2}\cdot 4\pi a^2 = 4\pi k^2\,\frac{(b-a)}{ab},$$

and the bounds for C become

$$\frac{K\frac{b-a}{ab}}{\left(\frac{1}{a} - \frac{1}{r_o}\right) + K\left(\frac{1}{r_o} - \frac{1}{b}\right)} \le \frac{C}{C_o} \le \frac{K\left(\frac{1}{a} - \frac{1}{r_o}\right) + \left(\frac{1}{r_o} - \frac{1}{b}\right)}{\frac{b-a}{ab}},$$

or in terms of the susceptibility, χ,

$$\frac{1+\chi}{1 + \chi\frac{a}{r_o}\left(\frac{b - r_o}{b - a}\right)} \le \frac{C}{C_o} \le 1 + \chi\frac{b}{r_o}\left(\frac{r_o - a}{b - a}\right).$$

Similarly, when the dielectric is in the low field region near the outer shell, the dielectric forms a hollow sphere of outside radius b and inside radius $r_i = \left[b^3 - f(b^3 - a^3)\right]^{\frac{1}{3}}$. The bounds for C become

$$\frac{K\frac{b-a}{ab}}{K\left(\frac{1}{a} - \frac{1}{r_i}\right) + \left(\frac{1}{r_i} - \frac{1}{b}\right)} \leq \frac{C}{C_o} \leq \frac{\left(\frac{1}{a} - \frac{1}{r_i}\right) + K\left(\frac{1}{r_i} - \frac{1}{b}\right)}{\frac{b-a}{ab}},$$

or in terms of χ

$$\frac{1+\chi}{1+\chi\frac{b}{r_i}\left(\frac{r_i - a}{b-a}\right)} \leq \frac{C}{C_o} \leq 1 + \chi\frac{a}{r_i}\left(\frac{b-r_i}{b-a}\right).$$

These bounds are plotted in figure 22 for a/b = 5 and $\chi = 0.23$. The high and low field graphs represent the extremes in capacitance as a function of volume fraction f. It turns out that the capacitance can be calculated in closed form in both the high and low field cases and that in each case the lower bound gives the exact value of the capacitance.

To illustrate the facility of the inequalities in (4-6) where it is difficult to obtain the capacitance explicitly, it is interesting to obtain the bounds for the case where the dielectric fills a spherical chord (see figure 22(b). This situation applies when the sphere is in a gravitational field and is being filled with a dielectric liquid. In this case, the integrals in (4-6) become

$$\int_V K|\nabla\varphi_o|^2 dV = 2\pi\int_\rho^b \int_o^{\theta'} K\frac{k^2}{r^2}\sin\theta d\theta r$$

$$+ 2\pi\int_\rho^b \int_{\theta'}^{\pi} \frac{k^2}{r^2}\sin\theta d\theta dr$$

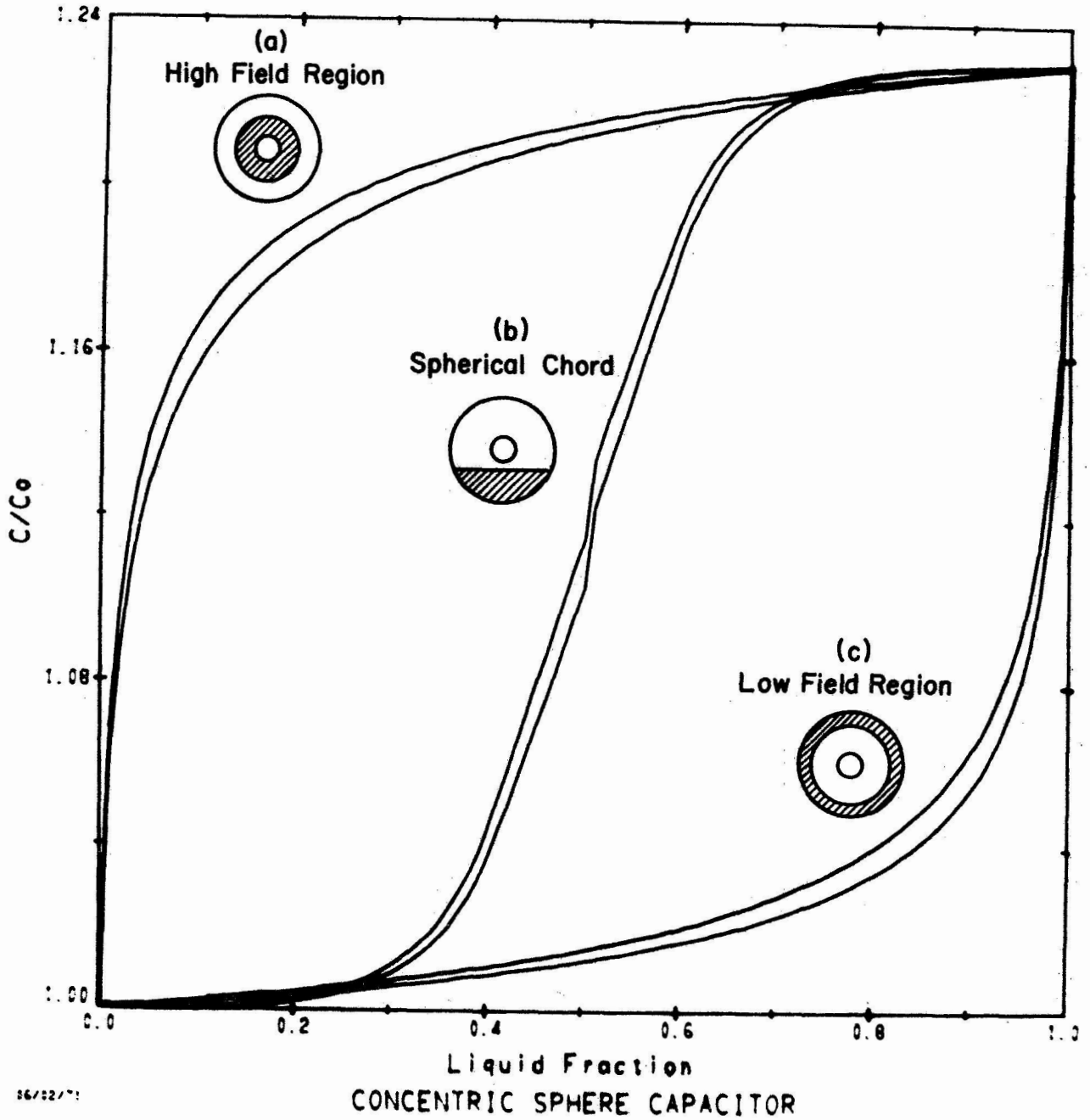

Figure 22. Behavior of Concentric Sphere Capacitor.

where $\theta' = \cos^{-1} d/r$ and $\rho = \max\{a, d\}$ where d is the distance from the center to the chord surface,

$$\int_V K|\nabla\varphi_o|^2 dV = 2\pi k^2 \int_\rho^b dr\left[\frac{K}{r^2}\left(1 - \frac{d}{r}\right) + \frac{1}{r^2}\left(1 + \frac{d}{r}\right)\right], \text{ etc.}$$

These integrals are easily evaluated and the bounds on C for this case are also plotted in figure 22 as a function of volume fraction of liquid.

Two Phase Dielectric in a Uniform Field (Total Mass Gauging)

Suppose a parallel plate capacitor of volume V (neglecting end effects) is partially filled with a two phase dielectric with dielectric constants K_1 and K_2 which are assumed to follow the Clausius-Mossotti relation

$$\frac{K - 1}{K + 2} = k\rho$$

where ρ is the density and k is a constant. It follows that

$$K_1 = \frac{2k\rho_1 + 1}{1 - 2k\rho_1}, \qquad \chi_1 = \frac{4k\rho_1}{1 - 2k\rho_1}$$

$$K_2 = \frac{2k\rho_2 + 1}{1 - 2k\rho_2}, \qquad \chi_2 = \frac{4k\rho_2}{1 - 2k\rho_2} \tag{4-10}$$

where ρ_1 and ρ_2 are the densities of the two phases. Let V_1 and V_2 be the volumes of the two phases and suppose for definiteness that $\rho_1 \geq \rho_2$; let m_1 and m_2 be the total mass of each phase.

The upper and lower bounds for C become

$$\frac{1}{\frac{V_1}{K_1 V} + \frac{K_2}{K_2 V} + \frac{V - (V_1 + V_2)}{V}} \leq \frac{C}{C_o} \leq \frac{K_1 V_1}{V} + \frac{K_2 V_2}{V} + \frac{V - (V_1 + V_2)}{V}.$$

Since $V_1 = m_1/\rho_1$ it follows that

$$\frac{1}{1 - \left[\frac{\chi_1 m_1}{K_1 \rho_1 V} + \frac{\chi_2 m_2}{K_2 \rho_2 V}\right]} \leq \frac{C}{C_o} \leq 1 + \frac{\chi_1 m_1}{\rho_1 V} + \frac{\chi_2 m_2}{\rho_2 V} .$$

Since $\rho_1 \geq \rho_2$, the following inequalities hold using equation (4-10):

$$\frac{\chi_1}{\rho_1} \geq \frac{\chi_2}{\rho_2}$$

$$\frac{\chi_2}{K_1 \rho_1} \leq \frac{\chi_2}{K_2 \rho_2} .$$

So that in terms of the total mass $M = m_1 + m_2$ it follows that

$$\frac{1}{1 - \frac{\chi_1}{K_1 \rho_1} \cdot \frac{M}{V}} \leq \frac{C}{C_o} \leq 1 + \frac{\chi_1}{\rho_1} \cdot \frac{M}{V} .$$

These bounds on C are the same as those plotted in figure 21 where χ is replaced by χ_1 and f is replaced by $m/\rho_1 V$. In this case the upper and lower bounds can be assumed only if the entire dielectric is in the high density phase.

4. 3. 2 Capacitors in Cubic Meter Test Dewar

Capacitors which were installed and tested in the upgrading dewar are shown in figure 2. One was a parallel plate design, which was made to share one plate with a TDR transmission line. This capacitor reached almost to the bottom of the dewar and always extended above the liquid surface. The "empty-space" capacitance was 193 pf. Spacing between the plates was 1. 27 cm; previous experience in the Density Reference System has shown that this spacing allows relatively free passage of moving solids.

A similar spacing was maintained between the electrodes of the "rod-to-blade" capacitor. This unit was designed with one curved and one round electrode, as shown in figure 2. Both capacitors were positioned to be parallel to the movement of fluid in the vessel during mixing. "Empty space" capacitance of the rod-to-blade was 68.949 pf.

Capacitance values for both capacitors are shown in figure 23 for triple-point and normal-boiling liquid hydrogen, and for 0.5 solid-fraction slush.

The top of the rod-to-blade was 162 cm above the dewar bottom, so the dielectric was all liquid or slush at levels higher than this. When totally submerged in triple-point liquid, the capacitance is

$$C = A\epsilon = A\,(1.2516).$$

The measured value was 86.296 pf, so $A = 68.949$ pf. This is the "empty space" capacitance at the triple-point temperature of 13.8 K, and makes possible the calculation of dielectric constant from capacitance measurement of any unknown slush mixture.

Conversion from measured capacitance to density is by way of the Clausius-Mossotti function

$$\frac{\epsilon - 1}{\epsilon + 1} = P\rho,$$

which can be written

$$\epsilon = \frac{1 + 2P\rho}{1 - P\rho} = \frac{(1 - P\rho) + 3P\rho}{1 - P\rho} = 1 + \frac{3P\rho}{1 - P\rho}.$$

The polarizability P increases about 0.1 percent between triple-point liquid hydrogen and 0.5 solid fraction slush[9]. The variation in ϵ is given by

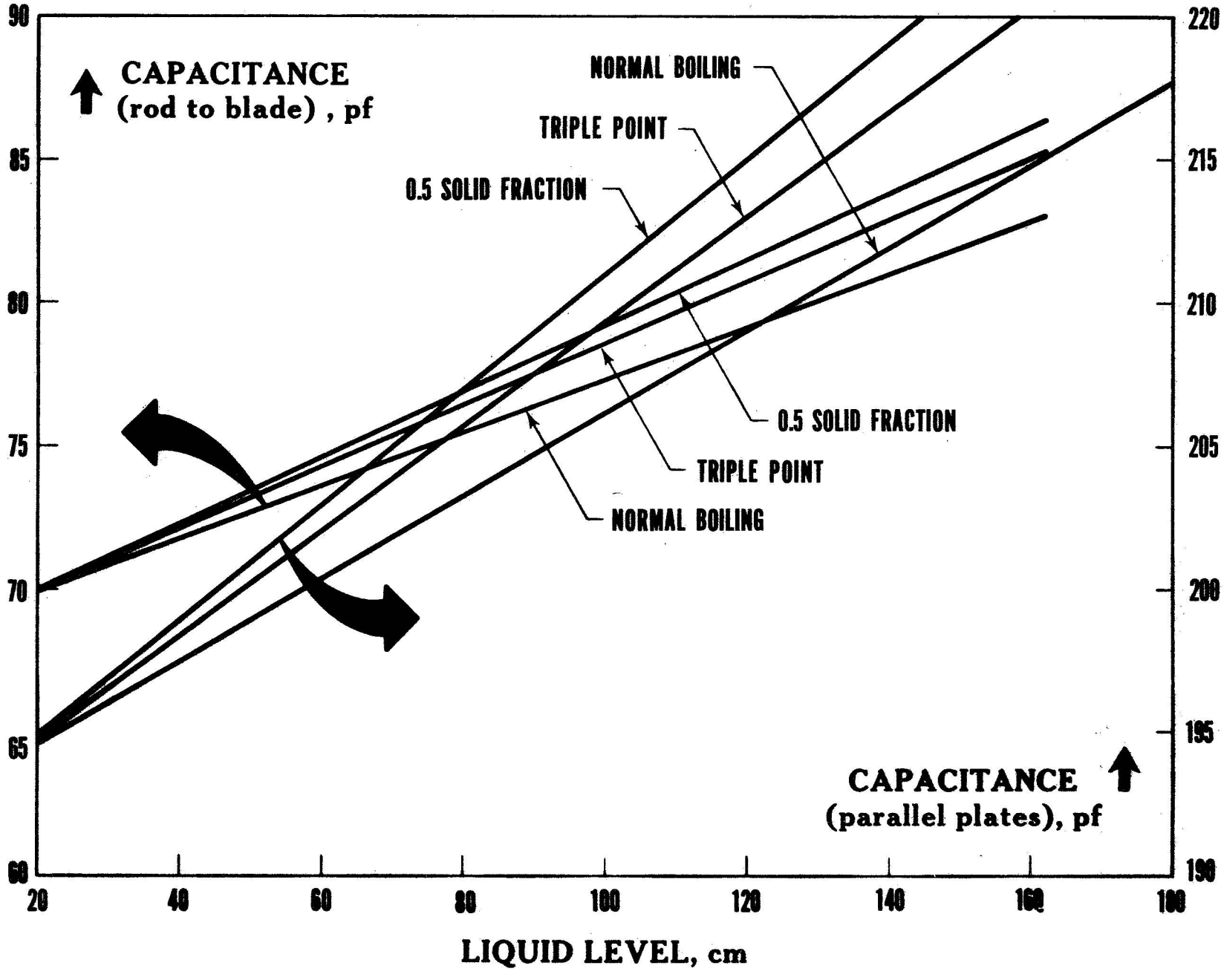

Figure 23. Data from Capacitors in One Cubic Meter Hydrogen Slush Vessel.

$$d\epsilon = \left(\frac{\partial\epsilon}{\partial P}\right) dP + \left(\frac{\partial\epsilon}{\partial\rho}\right) d\rho = \frac{3\rho dP + 3P d\rho}{(1 - P\rho)^2}.$$

Triple point liquid density is 77.017 kg/m^3; 0.5 solid fraction slush density is 81.526 kg/m^3. The corresponding polarizability values are 1.0046 and 1.0056 cm^3/g. Using the average of these values for ρ and P, and the difference between the extremes for dP and $d\rho$, we have

$$d\epsilon = \frac{3 \times 0.07927 \times 0.0010 + 3 \times 1.0051 \times 0.00451}{(1 - 1.0051 \times 0.07927)^2}$$

$$= 2.81 \times 10^{-4} + 1.61 \times 10^{-2}.$$

This is the change in ϵ which results when hydrogen changes from triple-point to 0.5 solid fraction slush. The first term is due to the change in polarizability; the second term is due to the change in density. If we start from the triple-point liquid value of $\epsilon = 1.25158$, the polarizability term accounts for a change in ϵ of 0.02 percent, while the density term accounts for a 1.3 percent change.

The above analysis applies when all of the dielectric between the capacitor electrodes is either liquid or slush, i.e, when the rod-to-blade capacitor is totally submerged, and when the density distribution is uniform. As soon as the liquid level drops below the top of the capacitor, the capacitance depends on volume between the electrodes, i.e., on liquid level, as well as on ϵ. In our rod-to-blade capacitor, a change of one cm in triple-point liquid level changes the capacitance by 0.10 pf. The upgrader cross section is 4560 cm^2, so 0.10 pf represents a triple-point liquid volume outflow of 4560 cm^3 or 351 g. The capacitance is easily read to the nearest 0.01 pf, which represents a mass change of 35 g, or about 0.06 percent of the full vessel.

Principal uncertainties in the mass measurement by this method result if the density between the capacitor electrodes is not known exactly. We have made an analysis of the uncertainty which results from an unknown density distribution; this uncertainty is shown to be small, indicating that the capacitor tends to integrate over mass rather than volume. The results are given in Appendix C.

4.4 Microwave Method for Dielectric Measurement

The capacitance measurements described above result in mass determination because the dielectric constant of the fluid between the capacitor electrodes can be derived from the capacitance. The mass then follows, with the uncertainties discussed in Appendix C, by use of the Clausius-Mossotti relation.

An alternative method for measurement of dielectric constant is based on time delay in propagation of a microwave signal. The density then follows from the C-M relation, and the total mass of fluid in the sample column can be calculated in a manner analogous to that described for the capacitance method. Two advantages of the microwave method are:

1) The sample is an unrestricted column of fluid between two microwave horns which can be spaced any desired distance apart.

2) The output signal is a frequency, which can be easily transmitted to a data center or, alternately, can be converted to a proportional voltage signal.

4.4.1 System Theory

The method is illustrated in figure 24. The microwave signal generator, shown in figure 24, is swept in frequency over its spectrum. The signal travels from the generator to the mixer by two paths, the reference and the test channels. It is assumed that both paths are dispersionless.

MICROWAVE SYSTEM USED TO MEASURE DENSITY IN TERMS OF TRANSMISSION TIME

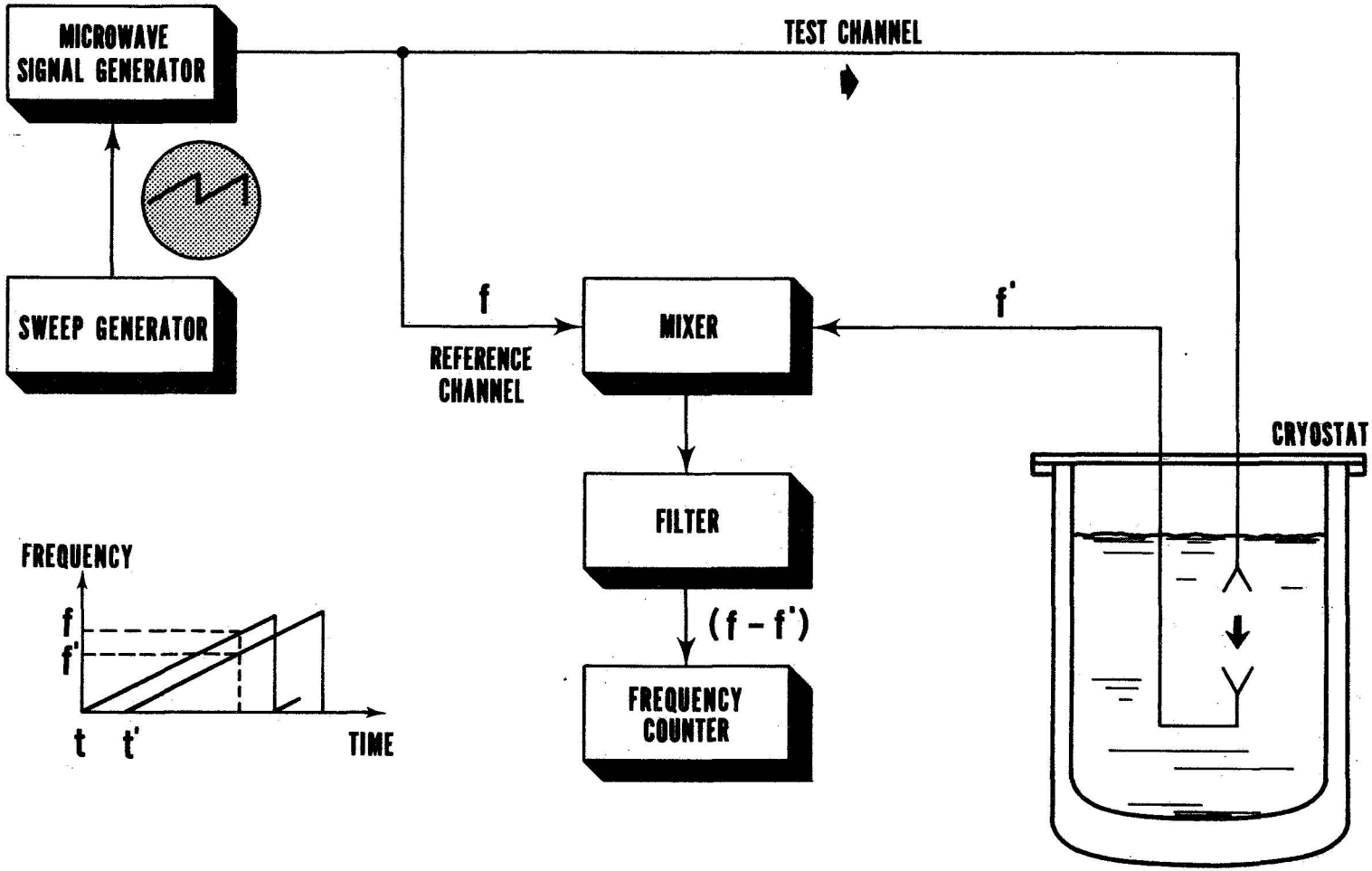

Figure 24.

The instantaneous frequencies of the two signals fed into the mixer are designated f and f′, and both of them vary linearly at the same time rate. But their frequencies differ because the cryogenic fluid delays the signal going through it.

The test signal undergoes a total phase shift given by

$$t = \frac{d\varphi}{d\omega} = \frac{\ell}{c}\sqrt{\epsilon}, \tag{4-11}$$

where t is the group delay time, ℓ is the distance between horn faces, and c is the free space velocity of propagation.

A finite change in the dielectric constant of the fluid produces a finite change in the group delay time,

$$\frac{\partial t}{\partial \epsilon}\Delta\epsilon = \Delta t = \frac{\ell}{2c}\frac{\Delta\epsilon}{\sqrt{\epsilon}}. \tag{4-12}$$

The frequency of the signal generator is swept over the bandwidth, $(f_2 - f_1)$ in time t_s. The average rate of change of frequency is

$$\frac{\Delta f}{\Delta t} = \frac{(f_2 - f_1)}{t_s}. \tag{4-13}$$

The difference between the instantaneous reference and test frequencies is then

$$\Delta f = \frac{(f_2 - f_1)\ell}{2ct_s\sqrt{\epsilon}}\Delta\epsilon \tag{4-14}$$

from which

$$\Delta\epsilon = \frac{2ct_s\sqrt{\epsilon}}{(f_2 - f_1)\ell}\Delta f. \tag{4-15}$$

The mixer, then, is essentially a product demodulator. Its output spectrum contains f and f′ frequency sums and differences, but all except the difference, Δf, are filtered out.

An analysis of the variation in equation (4-15) can be made to estimate the accuracy with which the change in dielectric constant ($\Delta\epsilon$) can be measured. Typical values and associated uncertainties are as follows:

t_s	=	10^{-3} seconds; $dt_s = \pm 10^{-5}$ seconds, the sweep period of the signal generator.
c	=	3×10^{10} cm/s; dc = ±1 cm/s, the free space velocity of electromagnetic radiation.
ϵ	=	1.25158, $\sqrt{\epsilon} = 1.119$; $d\sqrt{\epsilon} = \pm 10^{-3}$, the dielectric constant of triple-point liquid hydrogen.
Δf	=	50 hz; $d(\Delta f) = \pm 0.1$ hz, a typical frequency shift and the uncertainty of the counter used.
$(f_2 - f_1)$	=	3×10^9 hz; $d(f_2 - f_1) = \pm 10^7$, the frequency sweep of the generator.
ℓ	=	90 cm; $d\ell = \pm 0.2$ cm, the distance between horn faces.

The root mean square error is

$$\left[\frac{d(\Delta\epsilon)}{\Delta\epsilon}\right]_{rms} = \left[\left(\frac{10^{-5}}{10^{-3}}\right)^2 + \left(\frac{1}{3 \times 10^{10}}\right)^2 + \left(\frac{10^{-3}}{1.119}\right)^2 + \left(\frac{10^{-1}}{50}\right)^2 + \left(\frac{10^7}{3 \times 10^9}\right)^2 + \left(\frac{2 \times 10^{-1}}{90}\right)^2\right]^{\frac{1}{2}}$$

$$= (10^{-4} + 10^{-21} + 8 \times 10^{-7} + 4 \times 10^{-6} + 10^{-5} + 5 \times 10^{-6})^{\frac{1}{2}}$$

$$= 1.1 \times 10^{-2} = 1.1 \text{ percent.}$$

Most of this error in the $\Delta\epsilon$ measurement results from uncertainty in the sweep period of the signal generator. Conversion from $\Delta\epsilon$ to $\Delta\rho$, i. e., from change in dielectric constant to change in density, is again by way of the Clausius-Mossotti function, as explained in section 4. 3. 2 and Appendix C.

4. 4. 2 Experimental Results

Figure 25 shows data obtained in the one-m^3 upgrader for various levels of settled slush. The microwave horn faces were 90 cm apart; the lower horn face was 20 cm above the dewar bottom. The settled slush depths shown in figure 25 refer to distances above the lower horn face. The balance of the sample column, reaching to the upper horn, is assumed to be triple-point liquid. The effective dielectric constant thus becomes a direct function of the settled slush level.

The system is normalized, i. e., Δf is set equal to zero, with triple-point liquid between the horns. When slush is introduced, a frequency shift proportional to the change in effective dielectric constant is observed, as shown in figure 25. The mean or effective density then derives from the Clausius-Mossotti function; the deviation from linearity of ϵ vs. ρ in the C-M function is about 0. 8 percent over the density range from triple point liquid to freshly settled slush.

An independent estimate of density can be made by assuming a density for settled slush based on previous experience. A reasonable estimate for fresh settled slush is 81. 1 kg/m^3, i. e., a solid mass fraction of 0. 45. The average density of the column then becomes the weighted averages of the triple point liquid and settled slush depths. A density scale based on this assumption is shown on the right side of figure 25. This is simply another way of expressing the settled slush depth, and the two vertical scales are proportional to one another. A test of the method

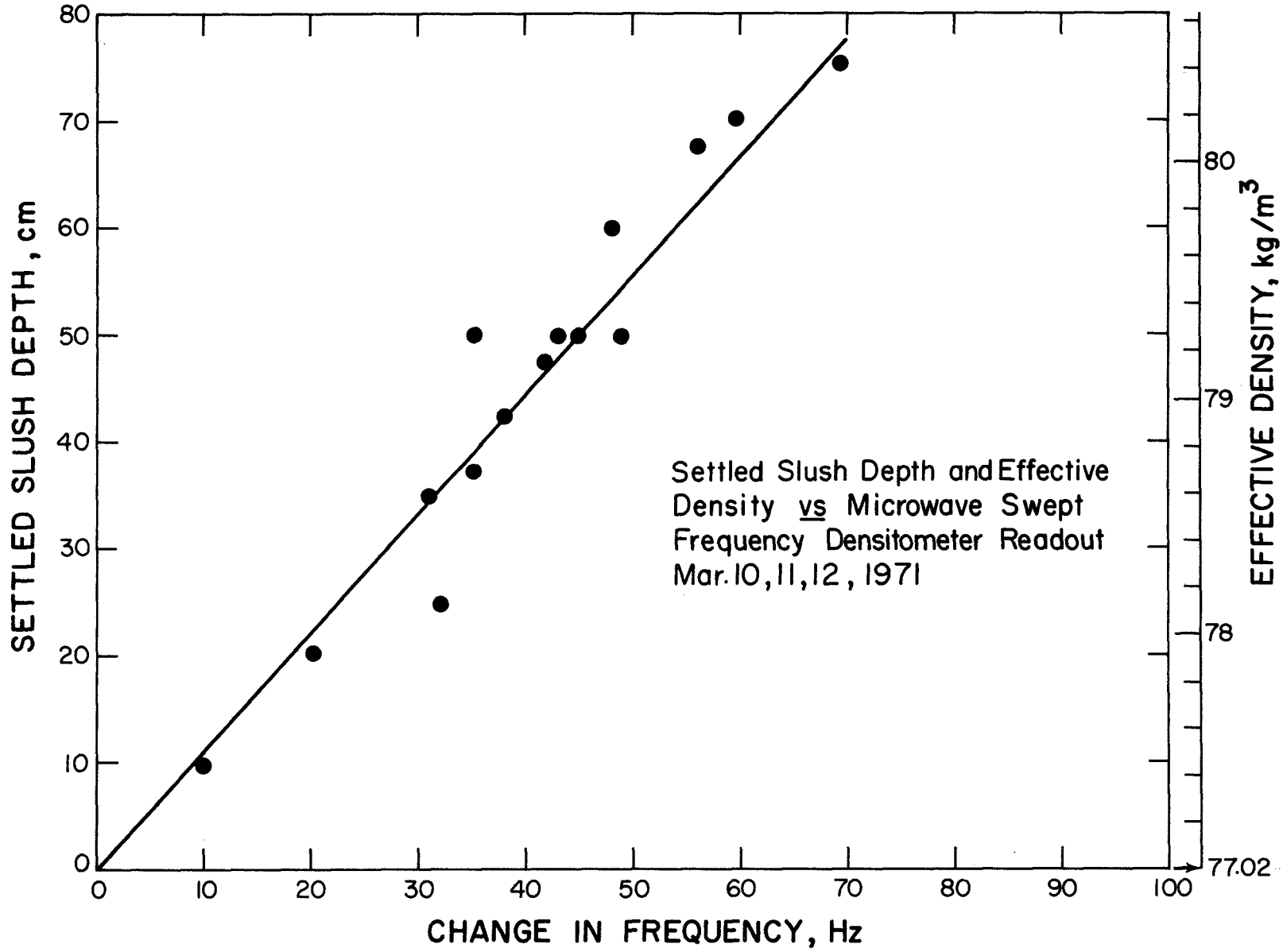

Figure 25. Settled Slush Density Data Obtained by Microwave Method.

is to plot the frequency shift against either vertical scale and observe the scatter of the data points and the deviation from linearity. The data indicate that the method can be used to locate a settled slush level to within about five centimeters if the above assumptions regarding liquid and settled slush densities are made. Conversely, if an unknown density distribution is assumed, the mean density can be determined with a sensitivity of a few tenths of a kg/m^3. It appears, at this point, that some refinement of readout instrumentation is all that would be required to make this method as simple and reliable as the more common capacitance measurement method.

5. Summary

The contract objectives were:

1) Explore methods for detection of settled hydrogen slush levels, and
2) Provide a method or methods for continuous inventory of hydrogen slush during storage.

Several approaches were examined for each objective, and it was experimentally verified that both objectives could be accomplished.

5.1 Settled Slush Level Detection

Carbon film sensors and a microwave method known as frequency domain reflectometry were both able to discriminate between triple-point liquid hydrogen and settled slush in a storage vessel. Accuracy of the interface location depends strongly on age and quiescence of the slush, i.e., on the sharpness of the density gradient. In well settled slush, carbon film sensors can locate the interface to ±0.5 cm or less.

We did not go beyond feasibility demonstration for the microwave FDR method. Oscilloscope patterns indicated a liquid-slush interface uncertainty of about ±5 cm.

The time domain reflectometry method was unsuccessful for slush level detection within the contract period. This method is being pursued, however, with lower thermal conductivity materials and a modified coaxial design. Indications are that a successful instrument of this kind will be developed.

5.2 Total Mass Gauging

The resonant cavity method of total mass sensing has many attractive features, particularly for containers with simple interior geometry. It was experimentally shown that the contents of a 48 cm diameter spherical vessel could be determined with an uncertainty of less than 0.5 percent of the full mass during several empty-to-full tests with liquid nitrogen. Encouraging results were also obtained in two cylindrical vessels, and extensive theoretical analyses were performed.

Experimental and theoretical studies of total mass gauging by capacitance methods show these to be the simplest and most accurate methods which are immediately available. Total mass of slush or liquid hydrogen between the capacitor electrodes can be determined with an uncertainty of about ±0.3 percent. Total mass in the storage tank then follows with similar accuracy if the sample between the electrodes is representative, and if the tank geometry is well defined. A capacitor which reaches from top to bottom of the tank is suggested, and an electrode configuration which allows free passage of the slush is essential. Such a capacitor was developed and is now in regular use at NBS.

5.3 Technology Transfer

A specific result of this contract work has been transfer of technology from NBS to a large hydrogen slush generation, storage, and flow facility which is under construction at the NASA-George C. Marshall Space Flight Center. This facility requires instrumentation for liquid

and slush density determination, liquid and settled slush levels, and temperature distribution profiles. These tank gauging systems will be installed in a 11.4 m^3 (3000 gallon) combination weigh tank and generator and in a 87 m^3 (23,000 gallon) combination slush storage and upgrading vessel.

The NBS Cryogenics Division will provide design drawings and consultation for installation of the rod-to-blade vertical capacitors in both vessels, carbon film ladders in both vessels, and a time domain reflectometry line in the 87 m^3 storage and upgrading vessel.

Appendix A.

Total Mass Gauging in a Spherical Resonant Cavity

Introduction

When a closed metal container is excited by an RF antenna probe inserted through a hole in the container, theoretically there are an infinite number of excitation frequencies for which the container is strongly coupled to the antenna; this means that energy can flow more freely between the antenna and the container at these resonant frequencies. The resonant frequencies correspond to standing wave patterns in the cavity which are called resonant modes. The wave pattern of the mode which occurs at the lowest possible resonant frequency is called the fundamental mode. This mode and the modes of the next few higher frequencies are called lower order modes.

When the cavity is uniformly filled with a fluid, the resonant frequency changes because the velocity of propagation of the resonant standing wave, $c = 1/\sqrt{\mu\epsilon}$, depends on the dielectric constant, ϵ, and the magnetic permeability, μ, of the fluid. For example, in a spherical resonant cavity uniformly filled, the resonant frequencies, f_{np}, are given by

$$f_{np} = \frac{u_{np}}{2\pi b\sqrt{\mu\epsilon}} \tag{A-1}$$

where b is the radius of the sphere, and n and p are subscripts which label the different modes (these will be explained in detail). The u_{np} are eigenvalues of the modes and are obtained in the process of finding solutions to Maxwells equations. The resonant frequencies can then be related to total mass by using the Clausius-Mossotti relation

$$P\rho = \frac{\epsilon - 1}{\epsilon + 2} \tag{A-2}$$

where P is the polarizability of the fluid which is a slowly varying function of the fluid density, ρ.

If the cavity is uniformly filled with a liquid, the eigenvalues, u_{np}, are just numbers independent of the fluid within the cavity and there is therefore a simple relationship between resonant frequency and total mass. However, if the container is only partially filled with liquid, the rest of the cavity being a vacuum or a gas, then the values of u_{np} will depend on μ and ϵ of the liquid, the μ_o and ϵ_o of the gas, and the geometry which the liquid takes within the cavity; the resonant frequency, then, is no longer an unambiguous function of mass but depends on the liquid geometry as well. This is because the standing wave patterns are distorted because of the boundary conditions at the liquid-gas interface. However, the resonant frequency of each partially filled mode does lie between the completely empty and completely full values

$$\frac{u_{np}}{2\pi b\sqrt{\mu\epsilon}} \leq f_{np} \leq \frac{u_{np}}{2\pi b\sqrt{\mu_o \epsilon_o}}, \qquad \text{(A-3)}$$

and varies continuously between these values as the cavity is filled. This suggests that the resonant frequency at least approximately indicates total mass independent of geometry.

The purpose of this note is to investigate the geometry effects for a spherical cavity with spherical symmetry of the liquid gas interface. This geometry is similar to a "zero-g" formation with the liquid clinging to the walls and a gas bubble in the middle of the cavity. The reason for choosing this geometry is that it is one of the few examples of a partially filled cavity for which the Maxwell Equations can be solved in closed form. Even though this gometry is particularly simple, it does give a reasonable

indication of the uncertainty which may be involved when the geometry is not known. Numerical examples are calculated for cases in which the liquid is hydrogen or nitrogen.

From a practical point of view, the spherical cavity is an ideal container geometry for this method of mass gauging. The reason for this is that the spherical symmetry of the cavity wall creates a degeneracy in the modes. That is, there are a number of standing wave patterns which have the same resonant frequency. This results in the fact that the distinct resonant frequencies of the lower order modes are widely separated and minimizes the effect of mode crossing in a partially filled cavity. Mode crossing occurs when, for a particular liquid geometry, the resonant frequency of a higher mode falls below that of a lower mode. For example, if the liquid is nitrogen, mode crossing between the first two modes is impossible and for the next few higher modes is quite unlikely; this is established from the table of eigenvalues, Table 1 on page 74, and the inequalities expressed in (A-3).

The relative independence of the lower order modes suggests that they can each be monitored independently. Since each mode has its own geometry in the standing wave pattern, it seems reasonable that the modes themselves may be used to at least partially determine the fluid geometry. (Mathematically the problem reduces to this: Given some of the eigenvalues of a boundary value problem, how closely can the eigenfunctions be approximated.) In fact, it will be shown that for the spherical symmetry considered in this analysis, that for a liquid of unknown density, both the location of the liquid-gas interface and the density (hence the total mass) can be determined uniquely if and only if five modes are monitored simultaneously. The reason for this is that each mode determines exactly one independent relation between the resonant frequency

of that mode and the five unknown parameters ϵ, μ, ϵ_o, μ_o, and a, where r = a is the liquid-gas interface. For most applications it is sufficient to assume that $\epsilon_o \approx \mu_o \approx \mu \approx 1$, leaving only two unknowns, namely ϵ and a. In this case, two modes will uniquely determine the total mass.

Solutions for Maxwells Equations in Spherical Coordinates

When the cavity is resonating at an angular frequency, ω, the time phase of the electromagnetic field is the same at all points within the cavity. Hence, for a loss free cavity the electric and magnetic fields can be written as the real parts of $Ee^{i\omega t}$ and $He^{i\omega t}$, respectively, where E and H are vectors which depend only on the spacial coordinates. The source free Maxwell Equations can then be written

$$\begin{aligned} \text{curl } E &= -i\omega\mu H \\ \text{curl } H &= i\omega\epsilon E \\ \text{div } \epsilon E &= 0 \\ \text{div } \mu H &= 0. \end{aligned} \tag{A-4}$$

It should be emphasized at this point that only two assumptions have been made, the cavity is loss free and it is source free; in practice these are usually very good assumptions for calculating resonant frequencies. A third assumption which we will now make, may have to be justified more carefully in any given situation: we assume that there are two regions within the cavity, each of which have uniform density. The technical advantage of this assumption is that derivatives of μ and ϵ are not involved; the equation (A-4) can be solved in each region where μ and ϵ are constant and the boundary conditions are then modified to include the liquid-gas interface. The boundary conditions can be written

$$\left\{\epsilon E\cdot n,\ \mu H\cdot n,\ \text{Exn and Hxn continuous at each boundary point}\right\} \tag{A-5}$$

where n is the unit normal vector to the surface at that point. Since

div E = 0 and div H = 0, both E and H can be expressed in terms of vector potentials G and F,

$$E = \text{curl } F$$
$$H = \text{curl } G \tag{A-6}$$

where the Maxwell Equations impose consistency conditions between G and F. Two independent solutions may be obtained by choosing a coordinate direction, say $\hat{r}$, the unit vector in the radial direction and finding fields which are perpendicular to $\hat{r}$. If E is perpendicular to $\hat{r}$ we say we have a TE (transverse electric) mode. This situation may be assured if F is chosen to be

$$F = f\hat{r} \tag{A-7}$$

where f is a scalar function of the spacial coordinates. In this case we have from (A-4) and (A-7)

$$E = \text{curl } f\hat{r}$$
$$H = -\frac{1}{i\omega\mu} \text{curl curl } f\hat{r}. \tag{A-8}$$

If H is perpendicular to r we say we have a TM (transverse magnetic) mode. This situation may be assured if G is chosen to be

$$G = g\hat{r} \tag{A-9}$$

where g is a scalar function of the spacial coordinates. In this case we have from (A-4) and (A-9)

$$E = \frac{1}{i\omega\epsilon} \text{curl curl } g\hat{r}$$
$$H = \text{curl } g\hat{r}. \tag{A-10}$$

The general solution for E and H may be obtained by a superposition of (A-8) and (A-10)

$$E = \text{curl } f\hat{r} + \frac{1}{i\omega\epsilon} \text{curl curl } g\hat{r}$$

$$H = \text{curl } g\hat{r} - \frac{1}{i\omega\mu} \text{curl curl } f\hat{r} . \tag{A-11}$$

To find equations which f and g satisfy, we consider the TE and TM modes separately. For the TM mode (A-10) and (A-4) imply that

$$\text{curl } E = - i\omega\mu \text{ curl } g\hat{r}$$

or

$$\text{curl } (E + i\omega\mu g\hat{r}) = 0 . \tag{A-12}$$

This last relation is satisfied only if

$$E + i\omega\mu g\hat{r} = \text{grad } \varphi \tag{A-13}$$

for some scalar function φ. Substituting (A-13) into the second of equation (A-4) we have

$$\text{curl curl } g\hat{r} = \omega^2\mu\epsilon\, g\hat{r} + i\omega\epsilon \text{ grad } \varphi. \tag{A-14}$$

Using the vector equation

$$\text{curl curl } g\hat{r} = \nabla^2 g\hat{r} - \text{grad } (\nabla\cdot g\hat{r}) \tag{A-15}$$

and

$$\omega^2\mu\epsilon = k^2$$

we find that g satisfies the following equations

$$(\nabla^2 + k^2)\, g\hat{r} = 0$$

$$\nabla\cdot g\hat{r} = - i\omega\,\epsilon\varphi . \tag{A-16}$$

A similar argument for the TE mode shows that f satisfies the following equation

$$(\nabla^2 + k^2)\, f\hat{r} = 0$$

$$\nabla\cdot f\hat{r} = i\omega\,\mu\nabla\psi. \tag{A-17}$$

Equations (A-16) and (A-17) are the scalar Helmholtz equations for g and f with standard solutions given by*

$$B_n(kr)\, L_n^m(\theta, \varphi)\ , \tag{A-18}$$

where the $L_n^m(\theta, \varphi)$ are spherical harmonics and the $B_n(kr)$ satisfy the differential equation

$$\left[\frac{d^2}{dr^2} + k^2 - \frac{n(n+1)}{r^2}\right] B_n(kr) = 0\ . \tag{A-19}$$

The general solution of equation (A-19) can be given as a linear combination of $j_n(kr)$ and $y_n(kr)$ which are the Spherical Bessel Functions of order n of the first and second kind respectively.**

$$B_n(kr) = C_n kr j_n(kr) + D_n kr y_n(kr) \tag{A-20}$$

where C_n and D_n are constants. The general solutions for f and g may be written as an infinite series

$$f = \sum_{n,m}^{\infty} \left(C'_{nm} kr j_n(kr) + D'_{nm} kr y_n(kr)\right) L_n^m(\theta, \varphi)$$

$$g = \sum_{n,m}^{\infty} \left(C_{nm} kr j_n(kr) + D_{nm} kr y_n(kr)\right) L_n^m(\theta, \varphi)\ . \tag{A-21}$$

The constants C_{nm}, D_{nm}, C'_{nm}, and D'_{nm} may be evaluated by substituting (A-21) into (A-11) and applying the boundary conditions (A-5). Equation (A-21) can be viewed as an infinite superposition of modes.

---

*See R. F. Harrington, Time Harmonic Electromagnetic Fields, McGraw Hill (1961).

**See M. Abrahamowitz and I. A. Stegun, NBS Handbook of Mathematical Functions, p. 437.

TM Modes Under Spherical Symmetry

The TM modes are obtained by setting $f = 0$. If the liquid has spherical symmetry the boundary conditions may be satisfied by using only one value each for n and m in equation (A-21) and thus the series for g contains at most two non-vanishing terms:

$$g = \left(C_{nm} kr j_n(kr) + D_{nm} kr y_n(kr)\right) L_n^m(\theta, \varphi). \tag{A-22}$$

Using equations (A-11) and (A-16) along with (A-22), the components of the electric and magnetic fields may be written as follows:

$$E_r = \frac{-1}{i\omega\epsilon}\left(\frac{\partial^2}{\partial r^2} + k^2\right) g = -\frac{n(n+1)}{i\omega\epsilon r^2} g$$

$$E_\theta = \frac{-1}{i\omega\epsilon r} \frac{\partial^2}{\partial r \partial\theta} g$$

$$E_\varphi = \frac{-1}{i\omega\epsilon r \sin\theta} \frac{\partial^2}{\partial r \partial\varphi} g$$

$$H_r = 0$$

$$H_\theta = -\frac{1}{r\sin\theta} \frac{\partial g}{\partial\varphi}$$

$$H_\varphi = \frac{1}{r} \frac{\partial g}{\partial\theta}. \tag{A-25}$$

The boundary conditions are applied by letting the container walls exist at $r = b$ and the liquid-gas interface at $r = a \leq b$ (if $a = 0$ the container is full and if $a = b$ the container is empty.). The conditions $\mu H \cdot n$ and $H \times n$ continuous at $r = a$ and $r = b$ imply continuity of H_θ and H_φ and hence that g is continuous at $r = a$ and $r = b$. This is compatible with the continuity of $\epsilon E \cdot n$. The condition $E \times n$ continuous implies that E_θ and E_φ is continuous and hence that $\frac{1}{\epsilon} \frac{\partial}{\partial r} g$ is continuous at $r = a$ and $r = b$. In summary the boundary conditions are completely specified by

$$g \text{ continuous at } r = a \text{ and } r = b \tag{A-26}$$

$$\frac{1}{\epsilon}\frac{\partial}{\partial r} g \text{ continuous at } r = a \text{ and } r = b. \tag{A-27}$$

Since the $L_n^m(\theta, \varphi)$ are independent both of radial position and fluid properties, the condition (A-26) is equivalent to

$$k_o a j_n(k_o a) = C_{nm} k a j_n(ka) + D_{nm} k a y_n(ka) \tag{A-28}$$

and

$$g(b) = C_{nm} k b j_n(kb) + D_{nm} k b y_n(kb) \tag{A-29}$$

where the coefficient of $y_n(k_o a)$ in equation (A-22) is zero because g must be finite at $r = 0$. (Here, $k_o = \omega\sqrt{\epsilon_o \mu_o}$ applies to the region in the gas and $k = \omega\sqrt{\epsilon\mu}$ applies to the region in the liquid.) Likewise condition (A-27) is equivalent to

$$\frac{1}{\epsilon_o}\frac{\partial}{\partial a}\left[k_o a j_n(k_o a)\right] = \frac{1}{\epsilon}\frac{\partial}{\partial a}\left[D_{nm} k a j_n(ka) + D_{nm} k a y_n(ka)\right] \tag{A-30}$$

and

$$0 = \frac{1}{\epsilon}\frac{\partial}{\partial b}\left[C_{nm} k b j_n(kb) + D_{nm} k b y_n(kb)\right]. \tag{A-31}$$

Equations (A-28), (A-30), and (A-31) are three independent relations in the eight variables, C_{nm}, D_{nm}, a, ω, ϵ, μ, ϵ_o, and μ_o. The inhomogeneous equations (A-28) and (A-30) can be solved uniquely for C_{nm} and D_{nm} and these values are substituted in equation (A-31) which then becomes a homogeneous relation in six variables a, ω, ϵ, μ, ϵ_o, and μ_o. We will denote this relation by

$$F_n(\omega, a, \epsilon, \mu, \epsilon_o, \mu_o) = 0 \tag{A-32}$$

or sometimes more simply by $F_n(\omega, \text{etc.}) = 0$. For a given set of values for a, ϵ, μ, ϵ_o, and μ_o (which is determined by conditions in the container), it can be shown that F_n plotted as a function of ω is oscillatory

and hence there are an infinite number of solutions to equation (A-32). The solution for the pth zero of equation (A-32) is called ω_{np} and the field pattern obtained by substituting ω_{np} and the values for C_{nm} and D_{nm} into equations (A-22) and (A-25) is called the TM_{mnp} mode where

$$n = 1, 2, 3, \ldots\ldots$$
$$p = 1, 2, 3, \ldots\ldots$$
$$m = 0, \pm 1, \pm 2, \ldots\ldots \pm n.$$

(The range on m comes from the properties of the spherical harmonics.) Since ω_{np} is independent of m, we see that there are a number of modes corresponding to the same ω_{np}. This number is called the degeneracy of ω_{np}. For example, the fundamental frequency ω_{11} corresponds to three modes, TM_{011}, TM_{-111}, and TM_{111} and hence has degeneracy 3. Sometimes the first subscript is dropped and the three modes are collectively referred to as the TM_{11} mode (which is an abuse of the term "mode").

We now discuss the conditions under which the resonant frequencies ω_{np} can determine the total mass. The total mass M is a function of three of the above variables, a, ϵ_o, and ϵ. If the resonant frequencies, ω_{np}, of the modes are known, then we have the following relations in the five variables a, ϵ_o, μ_o, ϵ, and μ

$$\begin{aligned} 0 &= F_1(\omega_{11}, \text{etc.}) = F_1(\omega_{12}, \text{etc.}) = \ldots\ldots \\ &= F_2(\omega_{12}, \text{etc.}) = F_2(\omega_{22}, \text{etc.}) = \ldots\ldots \\ &\quad\vdots \qquad\qquad\qquad \vdots \qquad\qquad\qquad \vdots \\ &= F_n(\omega_{np}, \text{etc.}) \end{aligned} \qquad \text{(A-33)}$$

where each of the $F_n(\omega_{np}, \text{etc.})$ is a relation determined by measuring the resonant frequency of a TM_{mnp} mode. Since there are five variables,

it is clear that at least five different modes are necessary to completely determine the total mass. From the properties of the Spherical Bessel Functions it can be shown that each of the above relations is also independent; therefore, five modes are also sufficient to determine the total mass. If further assumptions are made, fewer modes may be sufficient. For example, for most liquids $\mu \approx \mu_o \approx 1$ reduces the number of necessary modes to 3; if it is further assumed that $\epsilon_o \approx 1$, then the number of necessary modes is two; finally if in addition ϵ is known, then only one resonant frequency is necessary to determine the total mass.

Alternately, it may be that the interface, $r = a$, is known and ϵ (hence the density) is unknown; if $\epsilon_o \approx \mu_o \approx \mu \approx 1$, then the density and hence the total mass may be determined by a single resonant frequency. As a limiting case of this situation, the case $a = 0$ indicates a completely full cavity and the resonant frequencies are given by

$$\omega_{np} = \frac{u_{np}}{b\sqrt{\epsilon\mu}} \tag{A-34}$$

where u_{np} is the pth zero of equation (A-32) considered as a function of the quantity kb. (The quantities u_{np} are also known as eigenvalues of the TM_{np} "mode".) The measured frequency f_{np} is given by $f_{np} = \frac{\omega_{np}}{2\pi}$. The calculated values for u_{np} in the case $a = 0$ are listed in Table 1 in increasing order for the lowest ten modes. (Table 1 also includes results of a similar analysis for the TE modes.) The resonant frequencies f_{np} also plotted in Table 1 are for the specific case of a 48-cm diameter empty container.

We see from Table 1 that the resonant frequencies of the lower order modes are widely spaced. This is primarily due to the degeneracy and makes it feasible to simultaneously monitor several of the lower order modes.

Table 1.

Modes	Eigenvalues	Degeneracy	Frequency (48 cm dia. Sphere)
TM_{11}	$u_{11} = 2.744$	3	$f_{11} = 0.543$ GHz
TM_{21}	$u_{21} = 3.870$	5	$f_{21} = 0.766$
TE_{11}	$u'_{11} = 4.493$	3	$f'_{11} = 0.889$
TM_{31}	$u_{31} = 4.973$	7	$f_{31} = 0.984$
TE_{21}	$u'_{21} = 5.763$	5	$f'_{21} = 1.140$
TM_{41}	$u_{41} = 6.062$	9	$f_{41} = 1.200$
TM_{12}	$u_{12} = 6.117$	3	$f_{12} = 1.210$
TE_{31}	$u'_{31} = 6.998$	7	$f'_{31} = 1.384$
TM_{51}	$u_{51} = 7.140$	11	$f_{51} = 1.413$
TM_{22}	$u_{22} = 7.443$	5	$f_{22} = 1.472$

Examples Using Hydrogen and Nitrogen

Equation (A-32) was solved for the four lowest order modes using the FORTRAN program listed in Table 2.* For given values of a, ϵ, μ, ϵ_o, and μ_o, the program finds the zeros of $F_n(\omega$, etc.) plotted as a function of kb where

$$kb = \omega\sqrt{\mu\epsilon}\, b.$$

The pth zero is

$$u_{np} = \omega_{np}\sqrt{\mu\epsilon}\, b.$$

The computer plots the quantity αu_{np} vs. $\bar{\rho}$ which is essentially resonant frequency, f_{np}, vs. total mass M. Here,

$$\alpha = \sqrt{\frac{\epsilon_o \mu_o}{\epsilon\mu}},$$

*Written by A. E. Hiester.

Table 2.

```
      PROGRAM PLOT3
      DIMENSION IFILM(13),ITITLE(13),X(100),Y(100),AL(3),RHO(3)
      DATA (IFILM=24HART HIESTER, X3474                                )
      A(N,U,F,AL)=(1./AL*PJ(N,AL*F*U)*YPP(N,F*U)-AL**2*PPJ(N,AL*F*U)*YP(
     1N,F*U))/(PJ(N,F*U)*YPP(N,F*U)-PPJ(N,F*U)*YP(N,F*U))
      B(N,U,F,AL)=(AL**2*PJ(N,F*U)*PPJ(N,AL*F*U)-1./AL*PPJ(N,F*U)*PJ(N,A
     1L*F*U))/(PJ(N,F*U)*YPP(N,F*U)-PPJ(N,F*U)*YP(N,F*U))
      FUN(N,U,F,AL)=A(N,U,F,AL)*PJ(N,U)+B(N,U,F,AL)*YP(N,U)
    1 FORMAT(3F10.0)
    2 FORMAT(*U*,I2,5H      )
    3 FORMAT(1H1,10X,2A8//9X,11HALPHA * UNP,10X,*RHOBAR*//)
    4 FORMAT(9X,F9.5,10X,F10.7)
    5 FORMAT(*0U NOT FOUND IN 100 ITERATIONS*//1X,6E22.8)
    6 FORMAT(5H$1* U,I2,1H )
      P=1.
      ITITLE(1)=8H RESONAN
      ITITLE(2)=8HT FREQUE
      ITITLE(3)=8HNCY VS M
      ITITLE(4)=8HASS - H2
      ITITLE(7)=8HR$9HOBAR
      ITITLE(10)=8H      $1
      ITITLE(11)=8HA$9LPHA
      ITITLE(5)=ITITLE(6)=ITITLE(8)=ITITLE(9)=ITITLE(13)=8H
      READ 1,(AL(I),I=1,3)
      READ 1,(RHO(I),I=1,3)
      CALL GRAPH(1,1,3,IFILM,0,6)
      DO 60 N=1,4
      ID=P
      ID=ID+10*N
      ENCODE(8,2,IFILM)ID
      ENCODE(8,6,ITITLE(12))ID
      DO 55 I=1,3
      GO TO (7,8,9),I
    7 LTYP=8HTP SOLID
      GO TO 95
    8 LTYP=8HTP LIQ
      GO TO 95
    9 LTYP=8HNBP LIQ
   95 PRINT 3,IFILM(1),LTYP
      LINE=0
      DO 50 J=1,99
      RHOBAR=J
      RHOBAR=RHOBAR/100.*RHO(I)
      F=(1.-RHOBAR/RHO(I))**(1./3.)
      UB=7.5
      US=2.5
      FUS=FUN(N,US,F,AL(I))
      FUB=FUN(N,UB,F,AL(I))
      IT=0
   10 UM=(UB-US)/2.+US
      IT=IT+1
      IF(IT.LE.100)GO TO 15
      PRINT 5,US,FUS,UM,FUM,UB,FUB
      STOP
```

Table 2. (Continued)

```
 15 FUM=FUN(N,UM,F,AL(I))
    IF(ABS(FUM).LT..00001)GO TO 45
    IF(FUM.GT.0..AND.FUS.GT.0..OR.FUM.LT.0..AND.FUS.LT.0.)GO TO 20
    UB=UM
    FUB=FUM
    GO TO 10
 20 US=UM
    FUS=FUM
    GO TO 10
 45 X(J)=RHOBAR
    Y(J)=AL(I)*UM
    LINE=LINE+1
    IF(LINE.NE.51)GO TO 50
    LINE=0
    PRINT 3,IFILM(1),LTYP
 50 PRINT 4,Y(J),X(J)
    IF(I.NE.1)GO TO 53
    CALL LGRAPH(X,Y,99,ITITLE,IFILM)
    CALL CPGRAPH(X(99),Y(99),1,,,I+4)
    GO TO 55
 53 CALL CLGRAPH(X,Y,99)
    CALL CPGRAPH(X(99),Y(99),1,,,I+4)
 55 CONTINUE
    IFILM(1)=8H$9, $1TP
    IFILM(2)=8H SOLID'/
    IFILM(3)=8H$1+ TP L
    IFILM(4)=8HIQUID'/$
    IFILM(5)=8H1* NBP L
    IFILM(6)=8HIQUID
    CALL COMGRAPH(.75,.75,6,IFILM)
    CALL SKIPFRM
 60 CONTINUE
    STOP
    END

    FUNCTION SY(N,Z)
    Y1(Z)=-COS(Z)/Z
    Y2(Z)=-COS(Z)/Z**2-SIN(Z)/Z
    Y3(Z)=(-3./Z**3+1./Z)*COS(Z)-3./Z**2*SIN(Z)
    GO TO (10,20,30,40,50)N+1
 10 SY=Y1(Z)
    RETURN
 20 SY=Y2(Z)
    RETURN
 30 SY=Y3(Z)
    RETURN
 40 SY=5./Z*Y3(Z)-Y2(Z)
    RETURN
 50 SY=7./Z*(5./Z*Y3(Z)-Y2(Z))-Y3(Z)
    RETURN
    END

    FUNCTION SJ(N,Z)
    J1(Z)=SIN(Z)/Z
```

Table 2. (Continued)

```
      J2(Z)=SIN(Z)/Z**2-COS(Z)/Z
      J3(Z)=(3./Z**3-1./Z)*SIN(Z)-3./Z**2*COS(Z)
      GO TO (10,20,30,40,50)N+1
   10 SJ=J1(Z)
      RETURN
   20 SJ=J2(Z)
      RETURN
   30 SJ=J3(Z)
      RETURN
   40 SJ=5./Z*J3(Z)-J2(Z)
      RETURN
   50 SJ=7./Z*(5./Z*J3(Z)-J2(Z))-J3(Z)
      RETURN
      END

      FUNCTION PJ(N,Z)
      FN=N
      PJ=Z*SJ(N-1,Z)-FN*SJ(N,Z)
      RETURN
      END

      FUNCTION YP(N,Z)
      FN=N
      YP=Z*SY(N-1,Z)-FN*SY(N,Z)
      RETURN
      END

      FUNCTION PPJ(N,Z)
      FN=N
      PPJ=(FN*(FN+1.))/Z*SJ(N,Z)
      RETURN
      END

      FUNCTION YPP(N,Z)
      FN=N
      YPP=(FN*(FN+1.))/Z*SY(N,Z)
      RETURN
      END
```

$$f_{np} = \frac{\alpha u_{np}}{2\pi b\sqrt{\epsilon_o \mu_o}} ,$$

and

$$M = \bar{\rho} V$$

where V is the volume of the tank in cm^3. The results may then be applied to spheres of any size and to any dielectric fluid.

We have assumed that $\mu = \mu_o = \epsilon_o = 1$ and plotted the results for three different densities corresponding to solid hydrogen, triple point liquid, and normal boiling point liquid; this corresponds to about 22 percent range in density. The results for the first four modes are shown in figures A1, A2, A3, and A4. It is seen that the uncertainty in total mass is smaller for higher modes. Qualitatively this is because the field patterns are spread more uniformly throughout the cavity for the higher modes. For example, the uncertainty in mass vs. αu_{41} (or f_{41}) is less than 5 percent over most of the range. This is to be compared with a density change of 22 percent indicating that the resonant mode has a tendency to integrate over the mass of the liquid rather than the volume.

In order to obtain an estimate of the effects of liquid geometry, the volume fill curve is plotted in figure A5 for normal boiling point nitrogen in "zero gravity" (spherical symmetry). This is compared with data points taken from an experiment* filling a 48 cm diameter copper sphere in "normal gravity". This shows how much the changes in fluid geometry affect the resonant frequency of a single mode and makes it clear that if the geometry is completely unknown it may be necessary to use more than one mode in order to obtain the desired accuracy.

---

*See section 4. 1 of this report.

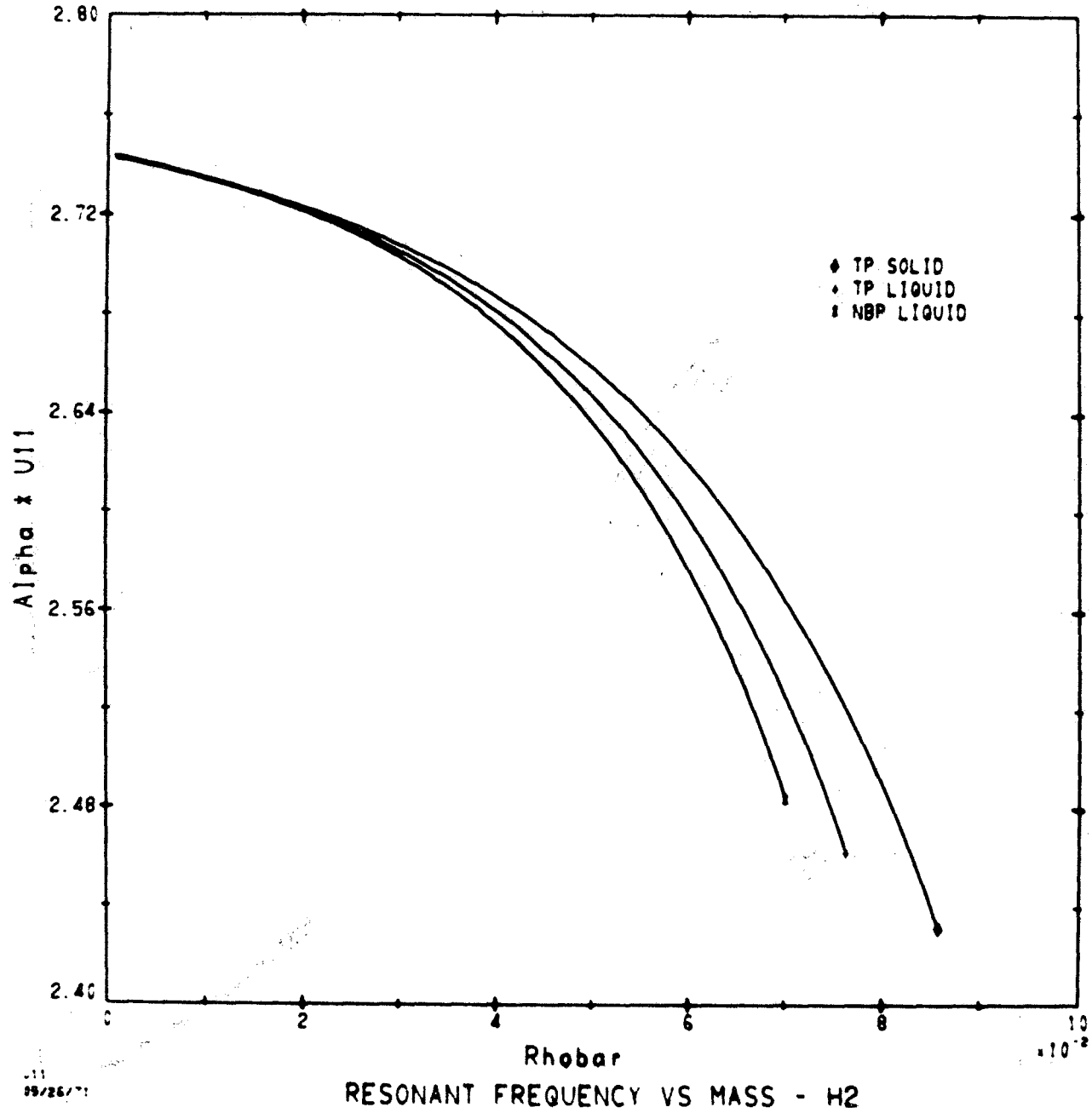

Figure A1. Resonant Frequency vs. Mass, TM_{m11} Mode.

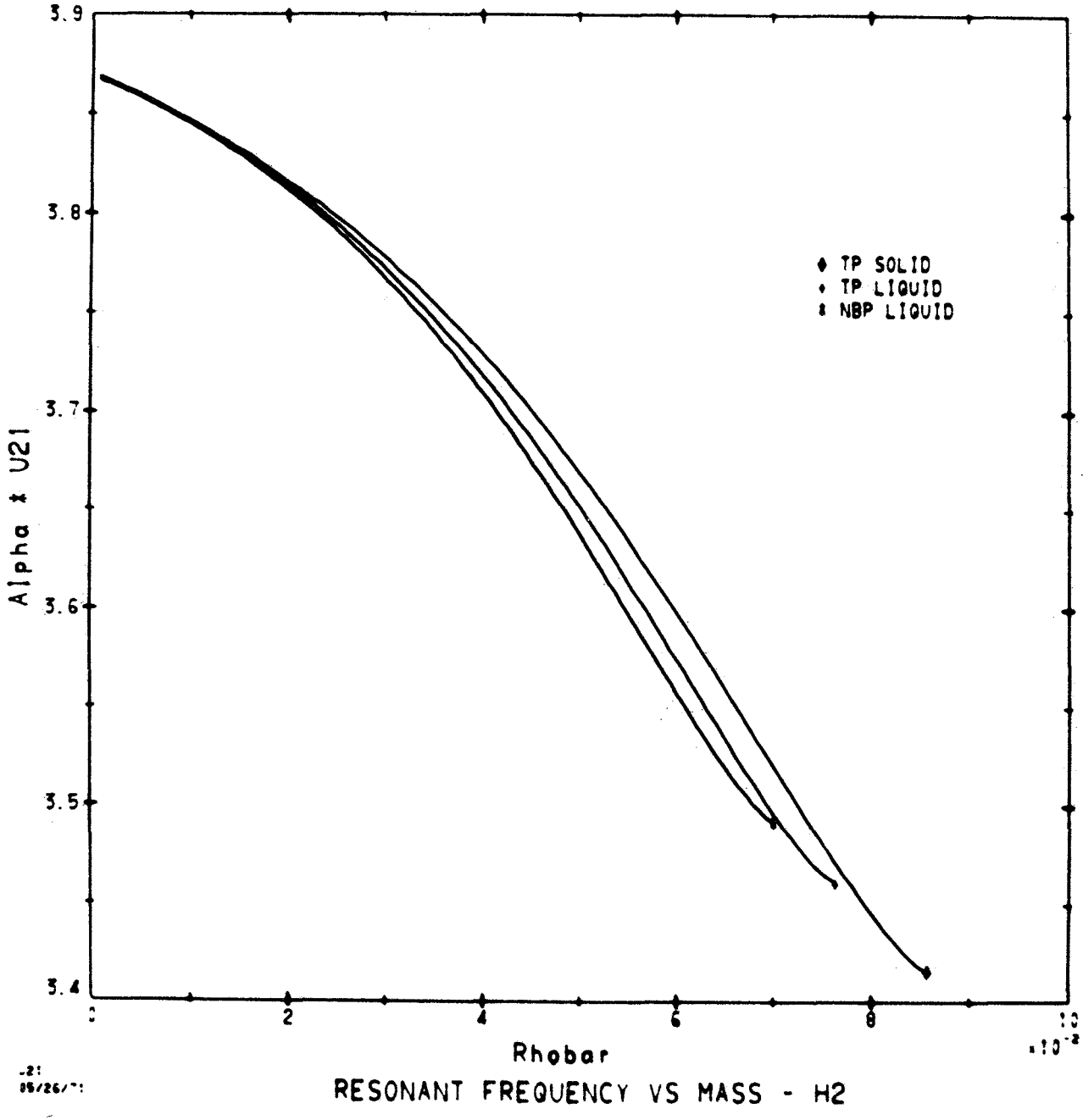

Figure A2. Resonant Frequency vs. Mass, TM_{m21} Mode.

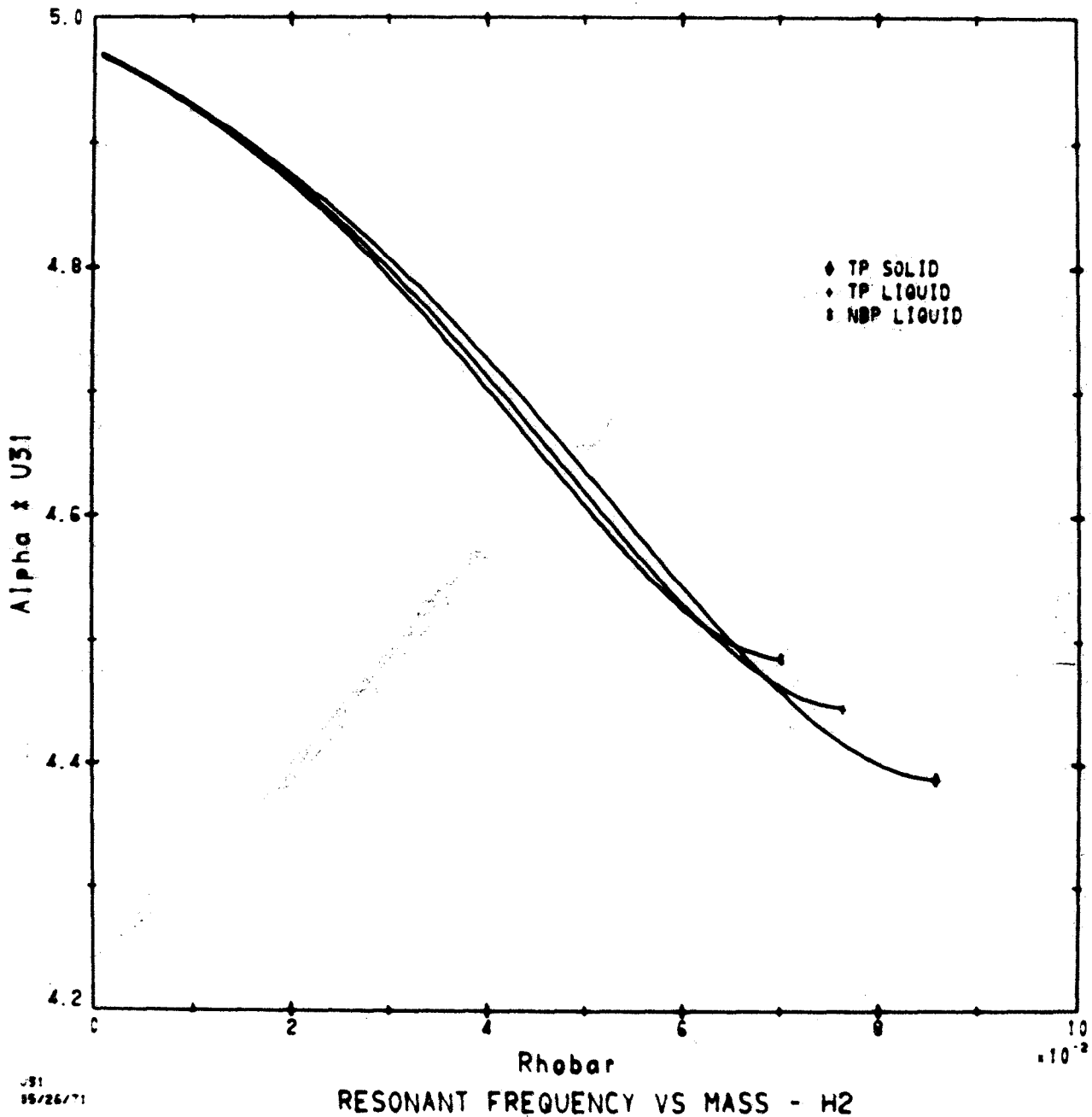

Figure A3. Resonant Frequency vs. Mass, TM_{31} Mode.

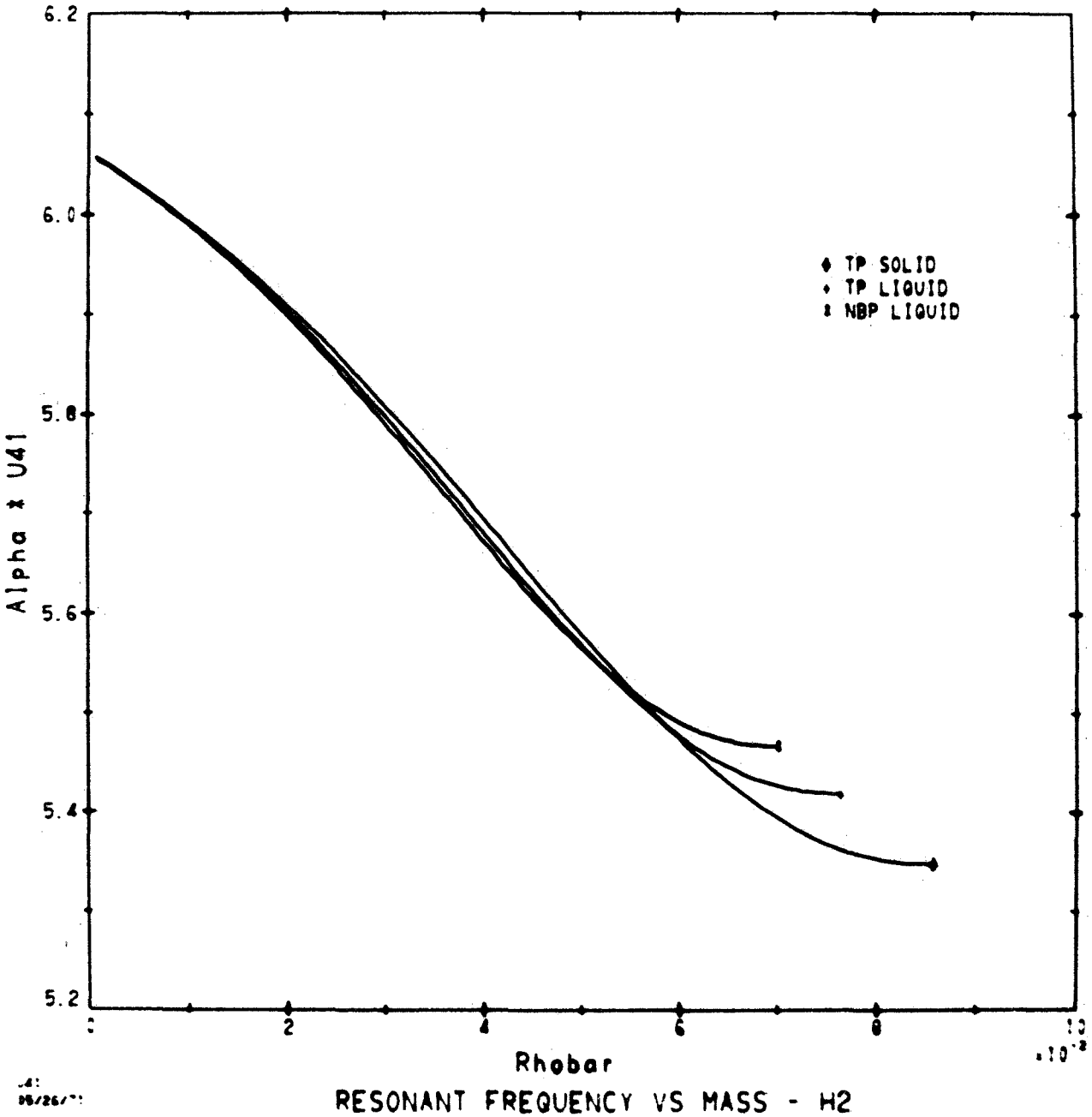

Figure A4. Resonant Frequency vs. Mass, TM_{m41} Mode.

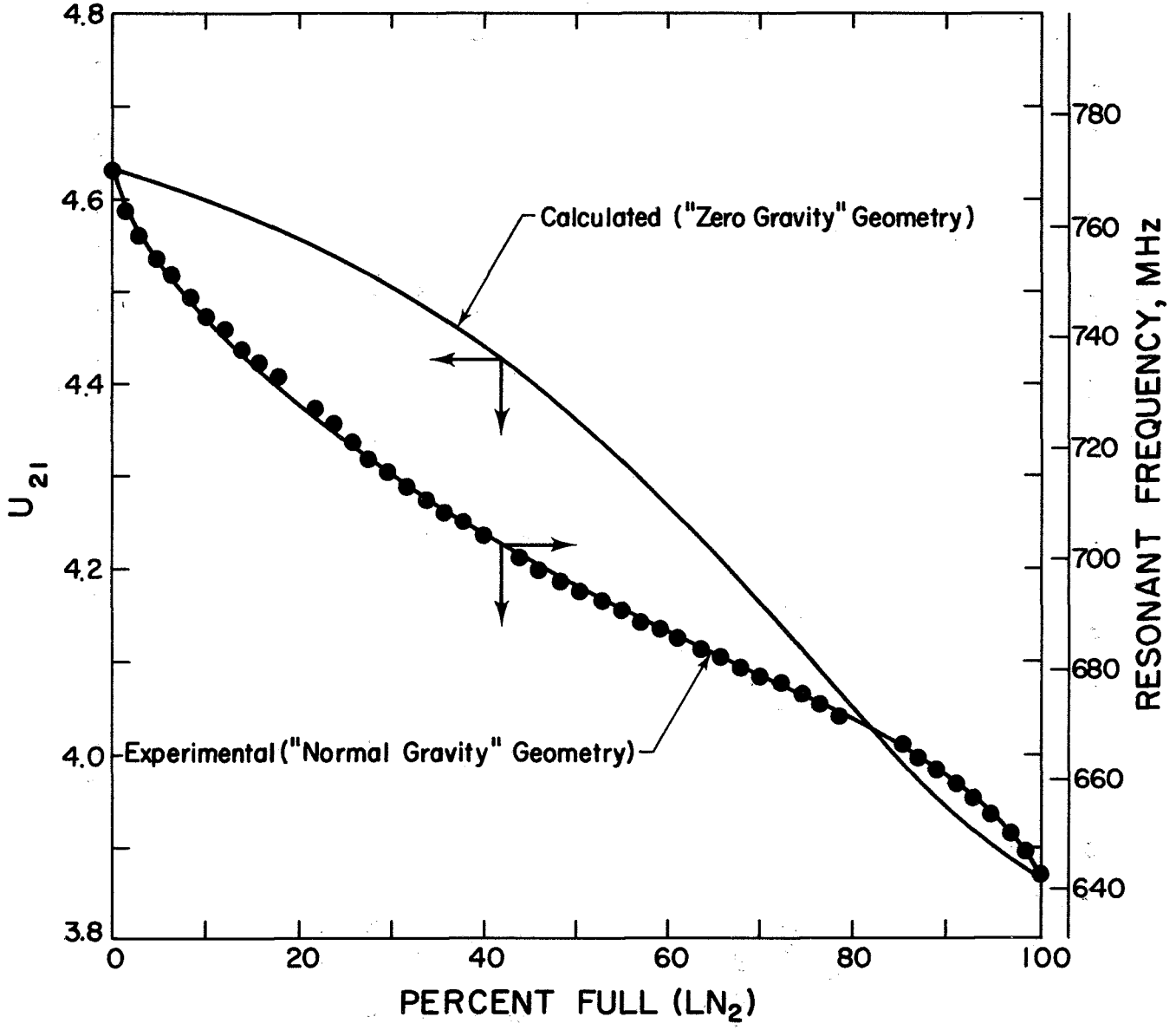

Figure A5. Mass Gauging in Spherical Vessel (TM_{021} Mode, Liquid Nitrogen).

Appendix B.

Upper and Lower Bounds for Capacitance in Terms of the Free Space Field

It is well known that for a two-electrode system the capacitance is given by

$$C = \frac{\epsilon_o}{(\varphi_1 - \varphi_2)^2} \int_V K|\nabla\varphi|^2 dV \tag{B-1}$$

where V is the open space not occupied by the electrodes, ϵ_o is the permittivity of empty space, K is the dielectric constant which may vary throughout V, and φ is the electrostatic potential satisfying the equations

$$\nabla\cdot(K\nabla\varphi) = 0 \text{ in } V$$

$$\varphi = \begin{cases} \varphi_1 \text{ on } S_1 \\ \varphi_2 \text{ on } S_2 \end{cases} \tag{B-2}$$

where S_1 is the boundary of V at the first electrode and S_2 is the boundary of V at the other electrode; $\nabla\varphi$ is the electric field. The integral in (B-1) is a minimum with repsect to certain variations in φ. These variational principles will be obtained directly in terms of the free space potential, φ_o, satisfying

$$\nabla\cdot\nabla\varphi_o = 0 \text{ in } V$$

$$\varphi_o = \begin{cases} \varphi_1 \text{ on } S_1 \\ \varphi_2 \text{ on } S_2 . \end{cases} \tag{B-3}$$

φ_o depends only on the electrode geometry and not on the geometry of the dielectric. The free space capacitance, K = 1, becomes

$$C_o = \frac{\epsilon_o}{(\varphi_1 - \varphi_2)^2} \int_V |\nabla\varphi_o|^2 dV. \tag{B-4}$$

Using the identity $\nabla\varphi_o = \nabla\varphi + (\nabla\varphi_o - \nabla\varphi)$, the following identity is useful:

$$\int_V K|\nabla\varphi_o|^2 dV = \int_V K|\nabla\varphi|^2 dV + 2\int_V K\nabla\varphi\cdot\nabla\left(\varphi_o - \varphi\right) dV$$

$$+ \int_V K|\nabla\left(\varphi_o - \varphi\right)|^2 dV. \qquad \text{(B-5)}$$

In the vector identity

$$\nabla\cdot\left(K\left(\varphi_o - \varphi\right)\nabla\varphi\right) = K\nabla\varphi\cdot\nabla\left(\varphi_o - \varphi\right) + \left(\varphi_o - \varphi\right)\nabla\cdot K\nabla\varphi \qquad \text{(B-6)}$$

the second term on the right vanishes because of equation (B-2). Therefore, using the divergence theorem (assuming sufficiently regular surfaces)

$$\int_V K\nabla\varphi\cdot\nabla\left(\varphi_o - \varphi\right) dV = \lim_{R\to\infty}\sum_i\int_{S_i}\left(\varphi_o - \varphi\right)K\nabla\varphi\cdot dS_i \qquad \text{(B-7)}$$

where S_o is a large spherical surface of radius R surrounding the electrodes and dielectric materials, S_1 and S_2 are the electrode surfaces and S_i, $i > 2$, are the surfaces which contain the interface regions between two different dielectric materials. The sum in (B-7) vanishes because: 1) on S_o the integral goes as $\frac{1}{R^3}$, 2) $\varphi_o = \varphi$ on S_1 and S_2, and 3) $(\varphi_o - \varphi)$ $K\nabla\varphi.dS_i$ is continuous for $i > 2$ and cancels $(\varphi_o - \varphi)K\nabla\varphi\cdot dS_j$ for some $j > 2$ where S_j coincides with S_i (dS_i and dS_j are oppositely directed outward normal vectors). With the vanishing of (B-7), equation (B-5) becomes

$$\int_V K|\nabla\varphi_o|^2 dV = \int_V K|\nabla\varphi|^2 dV + \int_V K|\nabla\left(\varphi_o - \varphi\right)|^2 dV. \qquad \text{(B-8)}$$

Since each term in (B-8) is non-negative it follows that

$$\int_V K|\nabla\varphi|^2 dV \le \int_V K|\nabla\varphi_o|^2 dV \qquad \text{(B-9)}$$

and the capacitance is maximized combining equations (B-1) and (B-9).

To minimize the capacitance in terms of K and φ_o, the Swartz inequality is applied twice in succession:

$$\int_V \nabla\varphi\cdot\nabla\varphi_o dV \le \int_V |\nabla\varphi|\,|\nabla\varphi_o| dV \le \left[\int_V K|\nabla\varphi|^2 dV \int_V \frac{|\nabla\varphi_o|^2 dV}{K}\right]^{\frac{1}{2}}. \quad \text{(B-10)}$$

The first integral in (B-10) can be simplified using the divergence theorem and the identity

$$\nabla\cdot(\varphi\nabla\varphi_o) = \nabla\varphi\cdot\nabla\varphi_o + \varphi\nabla\cdot\nabla\varphi_o, \quad \text{(B-11)}$$

where the last term in (B-11) vanishes in V because of equation (B-5),

$$\int_V \nabla\varphi\cdot\nabla\varphi_o dV = \lim_{R\to\infty}\sum_i \int_{S_i} \varphi\nabla\varphi_o\cdot dS_i \quad \text{(B-12)}$$

where S_i are defined as before. When the limit is taken in (B-12), the only remaining surface integrals are those bounded by the electrodes. Letting S denote the surface bounded by the electrodes and noting that $\varphi = \varphi_o$ on S equation (A-12) becomes

$$\int_V \nabla\varphi\cdot\nabla\varphi_o dV = \int_S \varphi_o\nabla\varphi_o\cdot dS. \quad \text{(B-13)}$$

Combining (B-13) and B-10) it follows that

$$\frac{\left[\int_S \varphi_o\nabla\varphi_o\cdot dS\right]^2}{\int_V \frac{|\nabla\varphi_o|^2}{K} dV} \le \int_V K|\nabla\varphi|^2 dV \quad \text{(B-14)}$$

and the capacitance is minimized by combining (B-1) and (B-14). In terms of the empty space capacitance, C_o, the upper and lower bounds can be expressed as

$$\frac{\left[\int_S \varphi_o \nabla \varphi_o \cdot dS\right]^2}{\int_V \frac{|\nabla \varphi_o|^2}{K} dV \int_V |\nabla \varphi_o|^2 dV} \leq \frac{C}{C_o} \leq \frac{\int_V K|\nabla \varphi_o|^2 dV}{\int_V |\nabla \varphi_o|^2 dV} . \tag{B-15}$$

Again using the divergence theorem it follows that

$$\int_V |\nabla \varphi_o|^2 dV = \int_S \varphi_o \nabla \varphi_o \cdot dS \tag{B-16}$$

and

$$\frac{\int_S \varphi_o \nabla \varphi_o \cdot dS}{\int_V \frac{1}{K} |\nabla \varphi_o|^2 dV} \leq \frac{C}{C_o} \leq \frac{\int_V K|\nabla \varphi_o|^2 dV}{\int_S \varphi_o \nabla \varphi_o \cdot dS} . \tag{B-17}$$

Appendix C.

Total Mass Gauging in a Cylindrical Tank by Capacitance Methods

If the density distribution of a fluid in a storage tank is unknown, there is an inherent uncertainty in the capacitance vs. total mass relation which is due to both geometric effects and the nonlinearity of the Clausius-Mossotti relation. It is then possible only to calculate upper and lower bounds for capacitance vs. total mass. However, it will be shown that for certain geometries and with knowledge on the limits of the fluid density, the difference between the upper and lower bounds can be small.

It will be assumed that gravity is along the axis of the cylinder and that if any density stratification takes place it will be normal to the cylinder axis. In this case the total mass, M, is given by

$$M = A\int_0^L \rho(\ell)\, d\ell \qquad \text{(C-1)}$$

where $\rho(\ell)$ is the density as a function of distance along the axis, A is the cylinder cross section and L is the length of the cylinder. Assume also that the capacitor is composed of two electrodes with surfaces that are parallel with the cylinder axis, i. e., any line parallel to the cylinder axis will not intersect the electrode surface at any angle other than zero. Because of the assumption on density stratification it follows that the capacitance, C, is given by

$$C = \frac{C_o}{L}\int_0^L \epsilon(\ell)\, d\ell\,, \qquad \text{(C-2)}$$

where $\epsilon(\ell)$ is the dielectric constant of the fluid as a function of distance

along the axis, C_o is the empty space capacitance and, for the moment, end effects are neglected so the capacitor length L is assumed to be equal to the cylinder length.

The Clausius-Mossotti relation is given by

$$P\rho = \frac{\epsilon - 1}{\epsilon + 2} \tag{C-3}$$

where P is the polarizability which is a slowly varying function of the density, ρ. Solving for ϵ gives

$$\epsilon = \frac{1 + 2P\rho}{1 - P\rho} \tag{C-4}$$

and dividing through the first term it follows that

$$\epsilon = 1 + \frac{3P\rho}{1 - P\rho}. \tag{C-5}$$

Substituting (C-5) into (C-2) it follows that

$$C = C_o + \frac{3C_o}{L}\int_o^L \frac{P\rho}{1 - P\rho}. \tag{C-6}$$

There remains only to find upper and lower bounds to this integral in terms of the relation (C-1). It is assumed that the limits of density and polarizability are known, i. e., that

$$\underline{P} \le P \le \bar{P} \quad \text{and}$$

$$\underline{\rho} \le \rho \le \bar{\rho}, \tag{C-7}$$

where the upper and lower bars refer to the upper and lower limits of the quantities. If $P\rho < 1$ then the quantity $\frac{1}{1 - P\rho}$ is an increasing function of $P\rho$ and it follows that

$$\frac{1}{1 - \underline{P}\underline{\rho}} \le \frac{1}{1 - P\rho} \le \frac{1}{1 - \bar{P}\bar{\rho}}. \tag{C-8}$$

It follows, using (C-8) and (C-1), that

$$\frac{\underline{P}}{1 - \underline{P}\underline{\rho}} \frac{M}{A} = \frac{\underline{P}}{1 - \underline{P}\underline{\rho}} \int_o^L \rho d\ell \le \int_o^L \frac{P\rho d\ell}{1 - P\rho} \le \frac{\bar{P}}{1 - \bar{P}\bar{\rho}} \int_o^L \rho d\ell = \frac{\bar{P}}{1 - \bar{P}\bar{\rho}} \frac{M}{A} \quad \text{(C-9)}$$

and, substituting (C-9) into (C-6),

$$C - C_o \le \frac{3C_o \bar{P}}{(1 - \bar{P}\bar{\rho})} \frac{M}{AL} \quad \text{and}$$

$$C - C_o \le \frac{3C_o \underline{P}}{(1 - \underline{P}\underline{\rho})} \frac{M}{AL} . \quad \text{(C-10)}$$

After combining the relations in (C-10), it follows that

$$\frac{(C - C_o)(1 - \bar{P}\bar{\rho})}{3C_o \bar{P}} \le \frac{M}{AL} \le \frac{(C - C_o)(1 - \underline{P}\underline{\rho})}{3C_o \underline{P}} . \quad \text{(C-11)}$$

If the difference between the upper and lower bounds is small, then the total mass is approximately proportional to $C - C_o$. The expression for this difference, Δ, is

$$\Delta = \frac{C - C_o}{3C_o}\left(\frac{1}{\underline{P}} - \underline{\rho} - \frac{1}{\bar{P}} + \bar{\rho}\right), \text{ or}$$

$$\Delta = \frac{C - C_o}{3C_o}\left(\frac{\bar{P} - \underline{P}}{\bar{P}\,\underline{P}} + (\bar{\rho} - \underline{\rho}\right) . \quad \text{(C-12)}$$

Another way of writing (C-11) is

$$\frac{2M}{AL} = \frac{\left(C - C_o\right)\left(1 - \bar{P}\bar{\rho}\right)}{3C_o \bar{P}} \begin{matrix} +\Delta \\ -0 \end{matrix} + \frac{\left(C - C_o\right)\left(1 - \underline{P}\underline{\rho}\right)}{3C_o \underline{P}} \begin{matrix} +0 \\ -\Delta \end{matrix}$$

or

$$\frac{M}{AL} = \frac{C - C_o}{3C_o}\left[\frac{1}{\bar{P}} + \frac{1}{2\underline{P}} - \frac{1}{2}(\bar{\rho} + \underline{\rho})\right] \pm \frac{\Delta}{2} . \quad \text{(C-13)}$$

Example -- A Liquid Hydrogen Tank with Solid Particles, i. e., Hydrogen Slush:

If gas and liquid are present, the density in the gas phase is negligible so that the integrand in (C-6) is essentially zero over the gas range. The upper and lower bounds for P and ρ can then be restricted to the liquid and solid phases. If it is known that the liquid is at triple point temperature and that the concentration of solid particles is less than 50 percent then, $\bar{P}$ and $\bar{\rho}$ are the corresponding values for 50 percent solid fraction and $\underline{P}$ and $\underline{\rho}$ are the values for triple point hydrogen. Substituting these values gives

$$\bar{\rho} = 0.081526 \text{ gm/cm}^3$$
$$\underline{\rho} = 0.077017 \text{ gm/cm}^3$$
$$\bar{P} = 1.0056 \text{ cm}^3/\text{gm}$$
$$\underline{P} = 1.0046 \text{ cm}^3/\text{gm}$$

$$\frac{1}{2}\left(\frac{\bar{P} - P}{P\,\underline{P}} + (\bar{\rho} - \rho)\right) = \frac{1}{2}(0.00099 + 0.0045) \text{ gm/cm}^3$$
$$= 0.0027 \text{ gm/cm}^3.$$

The total mass M is then obtained from equation (C-13)

$$\frac{M}{AL} = \frac{C - C_o}{3C_o}(0.9156 \pm 0.0027) \text{ gm/cm}^3.$$

It is seen that although the uncertainty in density is almost 5 percent, the uncertainty in total mass is about 0.3 percent, showing that the capacitor tends to integrate over mass rather than volume.

References

1. C. F. Sindt, Cryogenics, 10, 5 (1970).

2. R. Carlson, S. Krakaver, R. Monnier, V. Van Duzer, and R. Woodbury, "Sampling Oscillography," Hewlett Packard Applications Note 52 (Nov. 1959).

3. "Transmission Line Testing Using the Sampling Oscilloscope," Hewlett Packard Applications Note 53 (1959).

4. "Time Domain Reflectometry," Hewlett Packard Applications Note 62 (1964).

5. "Pulse Reflection Measurement of Transmission Line Impedance and Discontinuities," in-house publication, Tektronix (1962).

6. W. L. Willis and J. F. Taylor, "Time Domain Reflectometry for Liquid Hydrogen Level Detection," Los Alamos Report LA-3474-MS, University of California Report Library (1966).

7. W. L. Willis, "Disturbance of Capacitance Liquid Level Gauges by Nuclear Radiation," Advances in Cryogenic Engineering, Vol. 12, Plenum Press, N. Y. (1967).

8. R. H. T. Bates, "The Charcteristic Impedance of the Shielded Slab Line" PG MIT Transactions (Jan. 1956).

9. Lockheed Missiles and Space Co., "RF Liquid Level Sensing Technigues," LMSC-A785006, Contract NAS8-11476 (1966).

10. R. E. Post and R. G. Brown, "Method and Apparatus for Measuring Liquid Volume in a Tank," U. S. Patent 3,540,275 assigned to the Bendix Corp. (1970).

USCOMM - ERL